UC Berkeley
UC Berkeley Electronic Theses and Dissertations

Title
Rogue waves in unidirectional seas: statistics and prediction

Permalink
https://escholarship.org/uc/item/06x6s634

Author
Guo, Qiuchen

Publication Date
2018

Peer reviewed|Thesis/dissertation

Rogue waves in unidirectional seas: statistics and prediction

by

Qiuchen Guo

A dissertation submitted in partial satisfaction of the

requirements for the degree of

Doctor of Philosophy

in

Engineering – Mechanical Engineering

in the

Graduate Division

of the

University of California, Berkeley

Committee in charge:

Associate Professor Mohammed-Reza Alam, Chair
Professor Ömer Savaş
Professor Ming Gu

Fall 2018

Rogue waves in unidirectional seas: statistics and prediction

Abstract

Rogue waves in unidirectional seas: statistics and prediction

by

Qiuchen Guo

Doctor of Philosophy in Engineering – Mechanical Engineering

University of California, Berkeley

Associate Professor Mohammed-Reza Alam, Chair

The ability of accurately predicting the occurrence of rogue waves(i.e. time, location and maximum height) in the open ocean is limited by sparsity of field measurements and accuracy in numerical models. The difficulties with the latter arise primarily from the ability of taking into higher order nonlinearity, as well as allowing various mechanisms in rogue wave formations. In this dissertation, several steps on quantitative analysis toward understanding the statistical properties of rogue waves are presented, followed by a pioneer study on rogue wave prediction in two dimensional framework.

First, an approach to get averaged rogue wave profile was proposed to keep asymmetric trough shape respect to the main crest. The averaged profile using this new approach(i.e. approach II) and the blind averaging approach(i.e. approach I) were obtained in both space and time. By comparing the averaged shape using both approaches, we concluded that rogue wave is indeed asymmetric(i.e. the deeper trough can be as high as more than two times the shallower trough on two sides of the main crest). The widely used approach I omits this asymmetric feature in the averaged profile, thus rogue wave height can be strongly underestimated using approach I. This is especially important in estimating rogue wave height in space because we observed that rogue wave is generally more asymmetric in space compared with that in time. For example, rogue wave height in space is underestimated by 10% using approach I in sea state 5(i.e. H_s=3.25m, T_p=9.7s). Moreover, effect of nonlinearity was also addressed by quantitatively comparing the averaged shape of rogue waves with different order of nonlinearity in numerical simulations. Rogue wave formation is dominated by second-order nonlinear interaction, and further enhanced by higher-order nonlinearities.

The effect of stratification on the formation of rogue waves was evaluated by studying rogue waves in both homogeneous fluid and stratified fluid(i.e. two-layer stratified fluid). Through resonant interactions, energy can be exchanged from surface modes on the free surface and interfacial modes on the interface. This effect was quantitatively analyzed by comparing the rogue wave height in both models with identical initial conditions. In relatively short term(i.e. 100T_p), we found that regular oceanic stratification(i.e. density variation is

1% in upper and lower layer) does not play a crucial role in rogue wave formation. However, in strongly stratified ocean($\sim$5% density difference in upper and lower layer), rogue wave height can be strongly underestimated in relatively long term($500T_p$).

Finally, we quantitatively predicted rogue wave formation in the homogeneous fluid model for a short term(i.e. up to $100T_p$) by tracking energy concentration in space. This is motivated by the observation that energy concentrates in space several periods before rogue wave occurrence. We evaluated this energy concentration by calculating the energy flux, which is defined as energy across a vertical plane from seabed to free surface. The height of normalized net energy flux was found to be a good precursor in predicting rogue wave occurrence. A relatively low false positive rate(i.e. $\sim$20%) was achieved with most of the rogue waves being successfully predicted(i.e. more than 80% rogue waves are successfully predicted in the numerical database).

To my parents

Contents

List of Figures

List of Tables

Acknowledgments

My first thanks goes to my research advisor, Professor Mohammad-Reza Alam, who has provided me both guidance and freedom on research in the past six years. I still remember how he introduced me to this fascinating research area of rogue waves by showing me the picture of rogue waves on his desktop and explaining the mysterious aspects behind this phenomenon. He has been supporting me with thoughtful discussions and feedback. I will not reach this far without his continuous support. Although doing research with Reza can be tough sometimes, all these efforts has shaped me to a much better researcher compared with before. Reza is also the top instructor I have ever met so far. He is enthusiastic about his research can deliver his thoughts and passion to the audience. Even if that I only learned a small portion of his presenting skills, this can already be a life long treasure for my future career.

I would also thank other members of my committee for their contributions. Professor Ömer Savaş and Professor Ming Gu gave many valuable and inspiring comments to my dissertation. Professor Ömer Savaş was so encouraging and shared his opinions on ocean waves, which has helped me think of the problem in different perspectives. Professor Ming Gu is so kind and I have learned a lot numerical methods from his classes. These techniques turned out to be my close friends on research. I sincerely thank all the professors who served on my qualification exam, M.Reza Alam, Philip S. Marcus, Ömer Savaş and Ming Gu.

Special thanks goes to the collaborator Dr. Louis-Alexandre Couston, who co-authored two papers with me that will be published soon. He has always helped push the research forward by providing a lot of valuable discussions and comments. His passion on research in fluid dynamics also affects me a lot. I am grateful to have the chance to work with him on several papers together. I also want to thank all the current and previous members in Theoretical and Applied Fluids LAB(TAFLAB), Ahmad Zareei, Yong Liang, Farid Karimpour, etc. Our weekly meeting has always been mind blowing and a lot of great ideas to attempt come out from that.

The past five years would not be this great without my friends at Berkeley. I want to thank them for standing with me in good and bad times. The friendship will be one of the best things to remember at Berkeley. Qian Zhong has been my closest friend at Berkeley. I would sincerely thank her accompany. I also spent a lot of time with fluid and ocean folks, Abdulrahman Jbaily, Rachael Hager, David Fernández-Gutiérrez, Spencer Frank, Dongchi Yu, Lu Wang. All the fun time spent with these guys is the best memory of friendship.

Most importantly, I sincerely thank my parents, Junfeng Guo and Xuyun Zhang. They always believe in me and empower me especially when I doubt myself. Even though they may have different opinions with mine, they always support whatever decision I make. My deepest thanks go to my significant other, Haoyuan, for his constant love and support. He is encouraging at the same time pushing me to do my best. He traveled from China twice a year to spend time with me. He spent all his holidays and vacations to visit me for the past five years and I greatly appreciate that.

Chapter 1

Introduction and overview

For a long time in the past, it is hard to describe a rogue wave until you actually see one. Rogue wave is that kind of phenomenon that "exists" in the seafarers' stories. These waves were described as one or more "walls of water" or "holes in the seas" that come from nowhere. It was not until year 1995 that the first scientific measurement of rogue wave was gauged by lasers mounted on the Draupner platform standing in the North Sea[3]. This quantitative measurement is of significance to the scientific community proving that rogue wave does exist and can indeed reach terrifying height. Followed by the availability and improvements in accuracy of in-situ instrumentation(i.e. wave buoy, radar, laser, subsurface instruments such as pressure gauges, etc.), active research arose on rogue waves. During the past two decades, various mathematical models were proposed and many experimental works were conducted on studying rogue waves. However, many mysterious aspects remain. For example, the exact mechanism behind rogue wave occurrence is not clear yet, which also attributes to the difficulty in predicting rogue wave quantitatively. This chapter presented the motivation for this work on rogue wave statistics and prediction, followed by an overview of this research.

1.1   Motivation and background

Rogue waves, also called freak waves, extreme waves or monster waves, are large amplitude waves surprisingly appearing on the free sea surface. They are usually identified by a steep crest either followed or preceded by a deep trough. Extreme wave in the open ocean results in loss of vehicles and offshore structures every year. Recent accidents to the cruise ship *Norwegian Dawn*[4] and *Louis Majesty*[5] were caused by a sequence of large waves of more than 20 meters height striking the hull in Georgia's coast and Mediterranean sea respectively. In early 2016, a huge wave as high as 30 meters hitting offshore drilling rig *COSL Innovator* leaded to death of one crew member, several injuries and extensive damage of properties[6]. Not only causing tremendous losses on a global scale, rogue waves can also be threatening to individual people.

The highest wave measured on record reached more than 30 meters in height, while

most of the ships are designed for waves 10-15 meters high[7]. Moreover, rogue wave is an unexpected event, thus precaution can hardly be taken to avoid or reduce potential damage. Through statistical study of this phenomenon, rogue waves were found occurring much more frequency than indicated by the linear theory[8]. Offshore structures are especially vulnerable to rogue waves since the only thing they can do is to stand there withstanding the large wave. The current design of ships and offshore structures starts to take into account withstanding these extreme waves. For example, new offshore structures are designed with an larger air gap to minimize on-deck wave loads. However, it is still questionable to define accurately how strong we should build a structure or how large an air gap should be to withstand rogue wave considering both safety and cost. We can not achieve this without the inherent understanding of physical and statistical properties of rogue wave(i.e. cause of their occurrence, probability of occurrence, maximum crest height and maximum height they can reach, etc.).

1.1.1 Experimental observations

In the past decades, a database of field measurements, mainly time series, are accumulated with the employment of offshore instrumental devices. An examination of rogue waves in the database can provide intuitive recognition on what kind of environmental conditions rogue wave usually occur and the possible key parameters influencing rogue wave formation. It was found that rogue waves can occur in any sea conditions(i.e. wind generated sea, swell, current or a combination of them)[9], and in both linear and nonlinear circumferences[10]. By analyzing rogue waves in a large amount of wave data measured mainly in North Sea, it is found there exists a high correlation between large kurtosis and normalized rogue wave height in a sea state[11]. In addition, nonlinearity beyond second order is found important in the formation of some rogue waves in the open open. By studying the Andrea wave measured in a storm crossing the North Sea, Magnusson and Donelan[12] found the likelihood of very high crests is considerably greater than that expected from second order wave theory(i.e. Forristall distribution from second order Stokes wave) or linear wave theory(i.e. Rayleigh distribution).

Most of the rogue waves in open ocean were measured by wave buoy, hence numerous temporal series were accumulated but not the spatial ones. Spaceborne synthetic aperture(SAR) is the only instrument that has the capacity of observing large spatial wave fields with single wave resolution[13]. However, the SAR-based wave-height estimate is still far from being validated. The current data analysis of field measurement database can detect existence and some implications on rogue wave dynamics, but not able to provide a solid conclusion in various sea conditions.

Laboratory experiments in wave tank provide a wider variety in viewing rogue waves as a complement to field measurements. The laboratory experiment performed by Wu and Yao[14] and Toffoli et al.[15] showed that dispersive focusing and wave-current interaction(i.e. strong opposing current) may enhance rogue wave formation. Energy transfers to high frequency region when a rogue wave occurs. This was demonstrated by Fourier transform and wavelet transform analysis on laboratorial rogue wave time series[16]. An amplification of

high frequency amplitudes was observed as the nonlinearity increases. In shallow and intermediate water depth, experiments conducted by Baldock and Swan[17], Trulsen et al.[18], Viotti and Dias[19] showed that nonlinear wave-wave and wave-bottom bathymetry interaction increases the intensity of extreme-wave activity. Local high kurtosis can be used to quantify such high intensity. Moreover, wind effect can be taken into account directly in laboratory experiments. For example, Touboul et al.[20] correlated the weak increase of the rogue wave height and an asymmetry in the rogue wave height in space with the presence of wind blowing on mechanically generated wave group. Toffoli et al.[21] also designed an laboratory experiment in annular wave flume, where waves were forced naturally by wind. They observed strong deviation from Gaussian statistics in this wind forced wave field.

1.1.2 Mathematical modeling on rogue waves

From observations in open field and laboratory experiments, several theoretical models were developed in linear to weakly nonlinear framework. Rogue waves can be captured in linear model as a result of spatial wave focusing and dispersion enhancement, however, the frequency of occurrence is strongly underestimated. Weakly nonlinear mathematical models(i.e. nonlinear Schrödinger type equations) introduced new mechanism in forming rogue waves, such as modulational instability(i.e. Benjamin-Feir instability). Theoretical solutions have been derived in nonlinear Schrödinger(NLS) equation under certain limits[22, 23, 24, 25]. NLS is modified and deduced to Davey-Stewartson equation[26, 27] in deep water. In shallow water region, (modified) Korteweg-de Varies(KdV) equation is used to describe long wave dynamics[28, 29]. Kadometsev-Petviashvili(KP) equation is an extension from KdV equation in the case of propagation in three dimensional framework. Soliton like solutions are derived for KP solution[30, 25]. Explicit rogue wave solutions can help reveal conditions behind rogue wave formation and facilitate their observations. All the theoretical models discussed above are formulated in weakly nonlinear framework, which may be inadequate in describing rogue wave dynamics because rogue wave is a large amplitude and highly nonlinear phenomenon. Accordingly, higher order nonlinear and dispersive model(i.e. Zakharov equations) and even fully nonlinear wave equations(i.e. wave breaking effect) are required.

The fully linear dispersive and weakly nonlinear framework(i.e. Zakharov's equation [31]) describe the nonlinear random wave field focusing event, which is close to in situ sea states. Moreover, Zakharov equation accounts for the formation of rogue waves beyond modulational instabilities. NLS, extended Dysthe and Zakharov equations have good agreement in short term(i.e. $t < \mathcal{O}(T/\epsilon^2)$) but not in long term[10]. This implies full nonlinearity plays a crucial role in long-term wave evolution. Unlike some theoretical solutions to weakly nonlinear models, solutions to these highly/fully nonlinear models can only be solved numerically. Depending on the mathematical modeling, various numerical schemes are applied in different scenarios, including boundary integral method[32, 33], pseudo-spectral method[34, 35], volume of fluid method[36], etc.

1.1.3   Research objectives

This dissertation mainly dealt with several unsolved problems, including statistics of rogue wave and their prediction in 2-dimensional framework. Up to date, it is still under debate whether second-order nonlinearity is sufficient to describe rogue wave dynamics in open ocean. Good match had been obtained between second order theory(i.e. Tayfun distribution) and some field measurements[37]. At the mean time, many other filed measurements can not be described by such distribution. Hence higher order nonlinearities may still play an important, if not dominant, role in the formation of rogue waves. In this dissertation, higher order nonlinear effects were looked at in detail with the focus on morphology of averaged rogue wave profiles.

In the past mathematical models, oceanic stratification has not been taken into account in studying rogue wave formations. However, the ocean is known stratified, mainly due to temperature and salinity difference across the water depth. In stratified ocean, surface wave dynamics can change due to resonant interactions with internal waves[38, 39, 40]. For example, the triad resonance between surface mode and internal modes causes energy transfer between surface waves and internal waves[41]. Thus, rogue waves occurring on the free surface hence can be potentially altered if stratification is taken into account.

In addition, most of the research work on predicting rogue waves used weakly-nonlinear equations[42] or gave qualitative rather than quantitative results [43, 44]. Predicting rogue wave occurrence in highly-nonlinear framework is needed with the mechanism not limited to modulational instability. Within 2D framework, rogue waves were predicted quantitatively by directly tracking energy concentration in space.

1.2   Overview

Careful statistical analysis on a numerical rogue wave database was conducted to further understand the physical mechanism of rogue wave formation. These can potentially provide design guidance of offshore structures and ships, which need to withstand extreme environmental loads(i.e. on-deck wave load). The goal of this dissertation is to understand rogue wave dynamics and predict them quantitatively in two dimension framework, considering the effect of nonlinearity, ocean stratification, stratification, bathymetry and etc.

In chapter 2, we generalized the understanding of rogue wave dynamics and formulated the problem in two dimensional framework in Zakharov equation form. The problem setup considers both wave-wave interaction and wave-bottom interaction. Nonlinearity up to arbitrary order can be taken in to account. The problem is formulated so that it can be solved by high-order-spectral(HOS) method, where nonlinear wave evolution equations are solved in space and time efficiently(i.e. in terms of running time) and accurately(i.e. ability of considering high nonlinearity). Wave spectrum(i.e. JONSWAP and Pierson-Moskowitz spectrum) is used to describe the wind-generated wave field. Then the initial wave elevations and velocity potentials were calculated, which serve as the initial conditions of wave evolution

equations. With the increasing power of high performance computing resources, large wave field datasets are simulated numerically, with numerous rogue wave database accumulated based on definitions defined in chapter 2.

Chapter 3 described the statistical properties of rogue wave profile in both space and time. Using wave data from highly-nonlinear numerical simulations, two approaches were presented in analyzing rogue wave profile, one using blind averaging and the other one using flip to preserve the asymmetry. In agreement with the averaged profile of field measurements attained by Christou and Evans[9], it was shown that rogue waves are well captured in the numerical data set. Moreover, rogue wave crest height, wave height and asymmetry between troughs were discussed in different scenarios(i.e. severity of sea roughness, crossing sea states, etc.). In addition, the effect of nonlinearity on rogue wave profile was quantified on rogue wave morphology. Guidelines on describing rogue wave profile quantitatively were then provided based on these statistical analysis.

Chapter 4 presented effect of oceanic stratification on predicting rogue wave height using direct numerical simulations. Ocean is usually stably stratified due to temperature and salinity variations. A two layer model has been proposed by [45] as a simple model to represent this stratification in the ocean, with a lighter fluid on top and denser fluid on bottom. Following the two layer set up by Alam[40, 38], the effects of stratification intensity(i.e. density ratio varying from 0.9 to 0.99), water depth for upper and lower layer, existence of internal modes were presented in detail. This serves as the first work considering effect of stratification in the study of oceanic rogue waves to the authors knowledge.

In Chapter 5, we addressed the challenging problem of predicting rogue wave occurrence quantitatively. Predicting rogue waves is one of the most important problem to solve in this research field. Ideas of identifying triangular characteristics in spectrum[44] and wave group detection[42] had been proposed in weakly nonlinear framework. Here, we looked at this problem in highly-nonlinear scenario and tackled the prediction problem by tracking energy concentration in space. It was found that energy concentrates periods of time ahead the actual rogue wave occurrence, which can potentially trigger rogue wave event. Thus, energy flux in space was used to predict rogue waves in time and relatively high prediction accuracy had been achieved. In this chapter, we also pointed out the possibility of using wavelet transform to improve prediction accuracy, because wavelet analysis provides energy concentration not only in space, but also length scale.

Chapter 6 summarized the contributions of this work and provided recommendations on future directions for studying rogue wave dynamics in the ocean. The appendices included some detailed derivations as a supplement to the main chapters. Appropriate references to sections in the appendices are given throughout.

1.3   Summary of contributions

In summary, the main contributions of this research are:

1. A numerical database of rogue waves were accumulated and validated against field measurements in open ocean.

2. Improved current understanding on rogue wave profile, especially the strong asymmetry in space compared with that in time.

3. Effect of nonlinearity was quantitatively presented on rogue wave formation.

4. Evaluated the effect of oceanic stratification on rogue wave formation, which turned out to have a small effect on quantifying rogue wave height.

5. Predicted rogue wave occurrence for a relatively mild sea state in the numerical database and relatively high accuracy in prediction has been achieved.

Chapter 2

Problem formulation and methodology

This chapter aims at providing the problem formulation which rogue wave dynamics is based on. We began with a simplified model of 2-dimensional non-breaking waves over rippled bottom. The initial sea surface is characterized with a broadband wave field. The detailed description and formulation of this model are discussed in this chapter. We also discussed the High-Order-Spectral(HOS) method used to solve the highly nonlinear wave evolution equations. Since significant efforts were made to accumulate a numerical database of rogue waves, we covered various aspects on obtaining this numerical database.

2.1 Wave governing equations

Rogue wave is subjected to basic nonlinear wave dynamics, where surface waves are propagating over possibly non-uniform bottom topography. Of basic interests here are the conditions involving the incident wave and bottom topography wavenumbers. For water waves, we assume the fluid is inviscid, irrotational, incompressible and homogeneous. With surface tension neglected, the wave dynamics can be described by the potential flow theory. The general setup of the problem in shown in figure 2.1. A Cartesian coordinate system is defined with x-axis as the horizontal axis on the mean surface and z-axis positive upward. The free surface elevation is denoted as η, measured from mean free surface. h denotes the mean water depth. The rippled bottom can be expressed as $z = -h + \eta_b$, where η_b is the elevation of the bottom undulation measured from mean water depth. The flow in the fluid domain can be described by a velocity potential, $\phi(x, z, t)$. And the field velocity $\mathbf{u}(x, z, t)$ is expressed in terms of the velocity potential $\phi(x, z, t)$ with the relation $\nabla\phi = \mathbf{u}$. The nonlinear equations governing the potential flow in this model are:

$$\nabla^2\phi = 0 \qquad\qquad \text{at } -h + \eta_b < z < \eta(x, t) \qquad (2.1\text{a})$$

$$\eta_t + \eta_x\phi_x - \phi_z = 0 \qquad\qquad \text{at } z = \eta(x, t) \qquad\qquad (2.1\text{b})$$
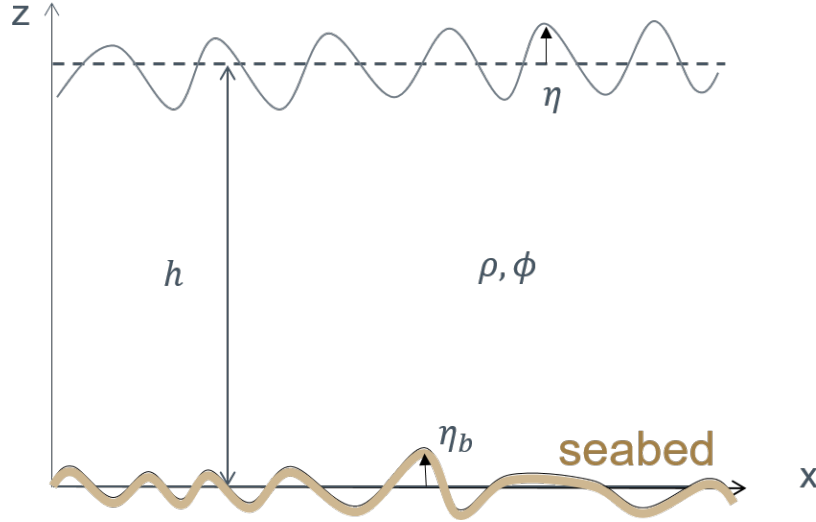
Figure 2.1: Definition sketch of waves over a rippled bottom in homogeneous fluid.

$$\phi_t + \frac{1}{2}(\phi_x^2 + \phi_z^2) + g\eta = 0 \qquad\qquad \text{at } z = \eta(x,t) \qquad\qquad (2.1\text{c})$$

$$\eta_{b,x}\phi_x - \phi_z = 0 \qquad\qquad \text{at } z = -h + \eta_b(x,t) \qquad\qquad (2.1\text{d})$$

Equation (2.1a) is derived from mass conservation, which is valid in the whole fluid domain. On the free surface, the kinetic surface boundary condition (2.1b) holds because we assume that fluid particles on the free surface have to stay on the surface. As a result of continuity of pressure and vertical velocity over this air-water interface, equation (2.1c) is valid on the free surface. Due to no penetration boundary condition at solid boundary(i.e. fluid particle can not go into the solid boundary), equation (2.1d) holds at the seabed.

We further define a velocity potential at the free surface $\phi^s(x,t) = \phi(x, z = \eta, t)$, and then rewrite the surface boundary conditions in the Zakharov form[31] (see equation (2.3)). This can be derived from equation (2.1) using chain rule, as in (2.2).

$$\frac{\partial \phi_S}{\partial t} = \frac{\partial \phi}{\partial t} + \frac{\partial \eta}{\partial t}\frac{\partial \phi}{\partial z}\bigg|_{z=\eta} \qquad\qquad (2.2\text{a})$$

$$\frac{\partial \phi_S}{\partial x} = \frac{\partial \phi}{\partial x} + \frac{\partial \eta}{\partial x}\frac{\partial \phi}{\partial z}\bigg|_{z=\eta} \qquad\qquad (2.2\text{b})$$

$$\eta_t = \phi_z^S(1 + \eta_x^2) - \phi_x^S \eta_x \qquad\qquad \text{at } z = \eta(x,t) \qquad (2.3\text{a})$$

$$\phi_t^S = -g\eta - 1/2(\phi_x^S)^2 - 1/2\phi_z^2(1 + \eta_x^2) \qquad\qquad \text{at } z = \eta(x,t) \qquad (2.3\text{b})$$

This Zakharov's equation can describe the evolution of a broadband surface waves on the free surface. The essential benefit of this form is the ease of expanding the velocity potential

into velocity potential in different orders and hence using HOS method to solve it efficiently. For given initial condition $\eta(x,0)$ and $\phi^S(x,0)$, this boundary-value problem can be solved by integrating the right-hand-side of equation (2.3) given $\phi_z(x,\eta,t)$ can be obtained at each time step. We assume that both $\phi(x,t)$ and $\eta(x,t)$ are $\mathcal{O}(\epsilon)$, where ϵ is a small parameter, in our case, is the wave steepness. We expand velocity potential ϕ and surface elevation η up to an arbitrary order M in ϵ. The expansions are as

$$\phi = \epsilon\phi^{(1)} + \epsilon^2\phi^{(2)} + \mathcal{O}(\epsilon^3) \tag{2.4a}$$

$$\eta = \epsilon\eta^{(1)} + \epsilon^2\eta^{(2)} + \mathcal{O}(\epsilon^3) \tag{2.4b}$$

where $\phi^{(m)}$ is the perturbation potential of order m. We expand $\phi(x,\eta,t)$ in Taylor series with respect to the mean free surface $z = 0$ evaluated on $z = \eta$, so that $\phi^{(s)}$ reads

$$\phi^{(S)}(x,t) = \phi(x,\eta,t) = \sum_{m=1}^{M}\sum_{k=0}^{M-m}\frac{\eta^k}{k!}\frac{\partial^k}{\partial z^k}\phi^{(m)}(x,0,t) \tag{2.5}$$

Then we collect $\phi(x,0,t)$ at different order $m = 1,2,\ldots,M$ and obtain the Dirichlet boundary condition on $z = 0$, as:

$$\phi^{(1)}(x,0,t) = \phi^S \tag{2.6a}$$

$$\phi^{(m)}(x,0,t) = -\sum_{\ell=1}^{m-1}\frac{\eta^\ell}{\ell!}\frac{\partial^\ell}{\partial z^\ell}\phi^{(m-\ell)}\bigg|_{z=0} \quad m = 2,3,\ldots,M; \tag{2.6b}$$

Similarly, substituting equation (2.4) into (2.1d), expanding the quantities on free surface and bottom in Taylor series with respect to the mean water depth h. We then collect the terms at each order $m = 1,2,\ldots,M$ and obtain equations for z derivative of ϕ:

$$\phi_z^{(1)}(x,-h,t) = 0 \tag{2.7a}$$

$$\phi_z^{(m)}(x,-h,t) = \sum_{\ell=1}^{m-1}\frac{\partial}{\partial x}\bigg(\frac{\eta_b^\ell}{\ell!}\frac{\partial^{(\ell-1)}}{\partial z^{(\ell-1)}}\bigg)\bigg|_{z=-h} \quad m = 2,3,\ldots,M; \tag{2.7b}$$

In addition, the perturbation velocity potential should also satisfy Laplace equation in the mean fluid domain and $-h < z < 0$, as:

$$\nabla^2\phi^{(m)} = 0 \tag{2.8}$$

In summary, the velocity potential at each order $\phi^{(m)}$ needs to satisfy mass conservation equation (2.8), Dirichlet boundary condition (2.6) and Neumann boundary condition (2.7).

2.1.1   Linear solution

Keeping only leading terms in the wave evolution equations(i.e. $m = 1$), the linear wave solution can be written as

$$\eta = a \cos(kx - \omega t) \tag{2.9a}$$

$$\phi = A \frac{\cosh(k(z + h))}{\cosh kh} \sin(kx - \omega t) \tag{2.9b}$$

where a is the wave amplitude for wave mode with frequency ω. A and a needs to satisfy the relation:

$$A = \frac{ga}{\omega} \tag{2.10}$$

where ω is wave frequency and k is wavenumber. They need to satisfy the dispersion relation in equation (2.11).

$$\omega^2 = gk \tanh(kh) \tag{2.11}$$

2.1.2   Nonlinear solution: High-order-spectral(HOS) method

Given the initial condition $\eta(x, 0), \phi^S(x, 0)$, the nonlinear governing equations 2.3 are solved in space and marching by integration in time. The spatial derivatives are solved by high-order-spectral method(HOS) method, which is originally developed by Dommermuth and Yue[46, 47] for wave-wave and wave-bottom interactions. This method generally takes into account of up to an arbitrary high order nonlinearity M in steepness as well as a large number of wave modes N $\mathcal{O}(1000)$. The accuracy of this method has been validated extensively through comparison with fully nonlinear simulation results[14] as well as the field measurements[35].

In a spectral approach, we represent $\phi^{(m)}$ as a summation of α^m and β^m. These basis functions satisfy the Laplacian equations in the mean fluid domain $-h < z < 0$ as well as the surface/bottom boundary conditions. $\alpha^{(m)}$ and $\beta^{(m)}$ can be written as

$$\alpha^{(m)} = \sum_{n=-N/2}^{N/2} \alpha_n^{(m)} \frac{\cosh[k_n(z + h)]}{\cosh(|k_n|h)} \exp^{ik_n \cdot x} \tag{2.12a}$$

$$\beta^{(m)} = \beta_0^{(m)} z + \sum_{n=-N/2}^{N/2} \frac{\sinh(k_n z)}{|k_n| \cosh(k_n z)} \exp^{ik_n \cdot x} \tag{2.12b}$$

Then we substitute (2.12) into boundary conditions (2.6) and (2.7), and obtain the following relations:

$$
\begin{aligned}
\alpha^{(1)} &= \phi^S, &&\text{at } z = 0 \\
\beta_z^{(1)} &= \frac{\partial \eta_b}{\partial t}, &&\text{at } z = -h \\
\alpha^{(2)} &= -\eta(\alpha^{(1)} + \beta^{(1)})_z, &&\text{at } z = 0 \\
\beta_z^{(2)} &= -\eta_b(\alpha^{(1)} + \beta^{(1)})_{zz} + \eta_{b,x}(\alpha^{(1)} + \beta^{(1)})_x, &&\text{at } z = -h
\end{aligned}
\tag{2.13}
$$
$$\cdots$$

Given any initial condition $\phi^S(x,0)$ and $\eta(x,0)$, $\alpha^{(m)}$ and $\beta^{(m)}$ can be solved from lower order relations. Thus $\phi^{(m)} = \alpha^{(m)} + \beta^{(m)}$ is easy to calculate. Since we assumed that ϕ can be expressed in perturbation series as $\phi = \sum_{m=1}^{M} \phi^{(m)}$ with $\phi^{(m)} \sim \mathcal{O}(\epsilon^m)$, such that, regrouping terms of same order results in a system of M forced linear partial differential equations. The equations are then solved sequentially efficiently using a spectral decomposition of ϕ_S and η in N Fourier modes. The results converge exponentially fast with N and M up to wave steepness $\epsilon \approx 0.35$ [46], allowing to capture high-order nonlinearties, which are essential to the rogue wave dynamics, at a relatively low computational cost (we typically use $N \sim \mathcal{O}(1000)$, $M \sim \mathcal{O}(10)$).

In order to use HOS method, the computational domain is assumed periodic in space. In practice, the non-dimensional computational domain is chosen from $[0, 2\pi)$ with space step $\delta x = 2\pi/\text{NDX}$, and NDX$= 2^q$. q is chosen to be 12 otherwise specified. Time step δt is chosen as $T/128$, where T is the characteristic wave period. In most of the cases, T_p is adopted here.

2.2   Characteristics of oceanic spectrum

The characteristic wave field can be represented only if the initial wave field are described properly. Usually, the spectral form is recommended to describe the wind-generated surface waves in the open ocean. Depending on significant wave height H_s and wave period T(i.e. peak period, zero-up-crossing period, etc.), spectra show sea surface variance, proportional to wave energy, as a function of wave frequency. The typical oceanic wave spectra include the Pierson-Moskowitz Spectrum[48] for fully developed seas(i.e. a sea surface produced by winds blowing steadily for long enough time over long distance) and JONSWAP(Joint North Sea Wave Project) spectrum[49] for developing seas(i.e. the waves may continue to develop due to non-linear wave-wave interactions), etc. These two spectra are single peaked, which are in agreement with most of the spectra measured in the open wave field. The parameters P-M and JONSWAP spectra depend on are defined in Table 2.1. H_s is calculated as 4 times standard deviation of surface elevation in this dissertation, unless otherwise specified.

The JONSWAP spectrum was determined from observations in the North Sea of fetch-limited waves. It is given by:

$$
S_J(\omega) = \frac{\alpha H_s^2 \omega_p^4}{\omega^5} \exp(\beta) \gamma^\delta
\tag{2.14}
$$

Table 2.1: Definitions of physical parameters used in P-M/JONSWAP spectra.

Parameters	Definition	Formula
H_s	significant wave height (m)	$4std(\eta)$
T_p	peak period (s)	$1/f_p$
f_p	frequency of the spectral peak (H_z)	$1/T_p$
ω_p	peak angular frequency(rad)	$2\pi f_p$

Table 2.2: Values of significant wave height H_s and peak period T_p in sea state 4, 5 and 6. The wave amplitude becomes higher and the peak period becomes longer from sea state 4 to 6.

Sea State	$H_s(m)$	$T_p(s)$
4	1.875	8.8
5	3.25	9.7
6	5.0	12.4

The JONSWAP spectrum has constant $\alpha = \frac{1}{16I_0(\gamma)}$, where $I_n(r)$ is the n-th order moment of the spectrum. The peak enhancement factor γ varies from 1 to 9. Nonlinearity becomes more important and the probability of the formation of freak waves increases as α and γ increase. γ usually has value in the range of 1-6. The typical value γ is 3.3 and we have $I_0(3.3) = 0.3$. The variables $\beta = -1.25\frac{\omega_p}{\omega^4}$ and $\delta = \exp(-\frac{(\omega - \omega_p)^2}{2\omega_p^2\sigma^2})$, where σ equals 0.07 and 0.09 for $\omega \leq \omega_p$ and $\omega > \omega_p$, respectively.

Pierson-Moskowitz spectrum was developed using Shipborne Wave Recorder traces obtained at the North East Atlantic Ocean Weather Stations. P-M spectrum accounts for fully developed seas generated by local winds. P-M spectrum can be expressed in the form of JONSWAP spectrum with the peak enhancement factor $\gamma = 1$ which writes

$$S_{P-M}(\omega) = \frac{\alpha H_s^2 \omega_p^4}{\omega^5} \exp(\beta) \qquad (2.15)$$

Within the scope of this dissertation, the developing sea is of the most interest, where the frequency of rogue wave occurrence is much higher compared with in developed seas. JONSWAP spectrum is also more commonly used in other similar research work. In figure.2.2, we show the JONSWAP spectrum with $\gamma = 3.3$ as well as the P-M spectrum for same H_s and T_p. In this dissertation, JONSWAP is generally used to account for developing sea states. But P-M spectrum is also used in chapter 3 to look into rogue wave statistics in fully developed seas.

Here, we compared the JONSWAP spectrum for three different sea state conditions, namely sea state 4, 5 and 6. The physical values of H_s and T_p are given in Table 2.2. The corresponding JONSWAP spectra for these three sea states are plotted in figure 2.3. Detailed study on rogue waves in different sea states is covered in chapter 3.
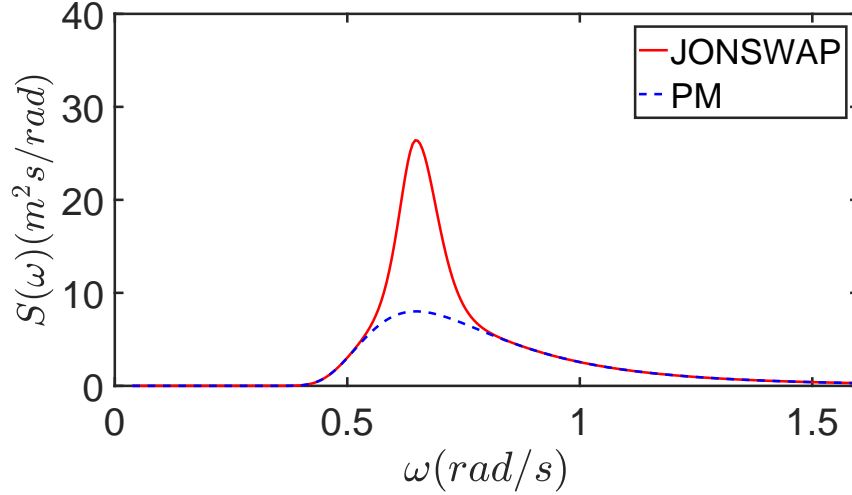
Figure 2.2: Comparison of JONSWAP spectrum and P-M spectrum given same physical parameters, $H_s = 3.75m$ and $T_p = 9.7s$. JONSWAP spectrum is similar to the P-M spectrum except that waves continue to grow with time(or distance) due to wave continuing blowing. Thus the JONSWAP spectrum has a more pronounced peak, as specified by the peak enhancement factor γ.

With a characteristic wave spectrum, the initial wave surface could be represented by a summation of a large number of sin waves. The idea behind wave spectrum is that almost any wave elevation $\eta(t)$ can be well approximated by a summation of an infinite number of sine and cosine functions with harmonic wave frequency. Their wave frequency and amplitude(i.e. from spectral density) are defined by proper wave spectrum function. In order to perform a large number of numerical simulations, we chose to initialize the wave field using wave modes defined by JONSWAP spectrum with random phases. Unidirectional wave is considered where the wave amplitude A can be expressed as an integral of spectrum and wave length:

$$A^2 = \int S(\omega)d\omega = \int S(k)dk \tag{2.16}$$

$S(k)$ is the spectrum density in wavenumber domain. $S(k)$ and $S(\omega)$ has the relation:

$$S(k) = S(\omega)C_g \tag{2.17}$$

where C_g is the group velocity of surface waves, $C_g = \frac{d\omega}{dk}$.

We expressed the wave amplitude in terms of the integral over wave number in stead of wave frequency ω to achieve higher numerical integral accuracy. This is based on the fact that we always have integer number of waves for any wave frequency in the computational domain per request of applying FFT algorithm in HOS. Thus dk is a constant but not $d\omega$.
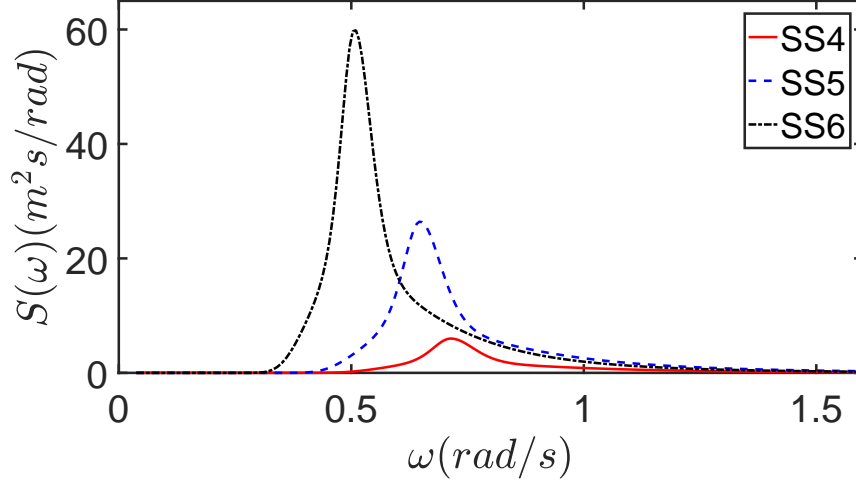
Figure 2.3: JONSWAP spectra in sea state 4(red solid line), 5(blue dash line) and 6(black dot-dash line). The same $\gamma = 3.3$ is used for all three sea states. Clearly, the peak of the spectrum shifts to the left as the peak period becomes longer. As the significant wave height increases, the spectrum also has a larger density.

The integration over constant step variable can be well calculated with higher accuracy. The discrete version of equation (2.17) is:

$$A_n = \sqrt{S(k_n)\delta k} \tag{2.18}$$

where A_n is the wave amplitude of wave with wavenumber k_n. Thus the initial wave field $(\eta(x,0), \phi^S(x,0))$ is characterized by a linear summation of waves with wavenumber k_n and random phases θ_n, given as:

$$\eta(x,0) = \sum_n A_n \cos(k_n x + \theta_n) \tag{2.19a}$$

$$\phi^S(x,0) = \sum_n g A_n \sin(k_n x + \theta_n) \tag{2.19b}$$

In practice, k_n could vary from 1 to the cut-off wavenumber k_c.

2.3 Definition of a rogue wave

Rogue waves are described as short-lived large amplitude waves in the ocean. But the definition on how large a wave should be to be called a rogue wave is still of dispute. Two types of rogue wave definition are commonly used in the past literature, one based on crest

height and the other based on wave height. Definitions of crest height η_c and rogue wave height H_r of rogue waves are illustrated in figure 2.4. The first one is stating that wave that is 2~3 times larger than the significant wave height is classified as rogue wave. Following the convention, 2 is used and the definition writes:

$$H_r >= 2H_s \tag{2.20}$$

The other one states that rogue wave should have maximum crest height η_c at least 1.2 1.3 times the significant wave height. The numerical database of rogue waves is mostly based on definition in equation (2.20). The definition (2.21) is used in chapter 3 for validation purpose.

$$\eta_c >= 1.25H_s \tag{2.21}$$

There are other claims that more parameters other than η_c and H_r should be included in order to well define a rogue wave. Ruban[50] proposed a definition including the parameter ,typical wavelength λ, where a wave with maximum wave height $h_{max} \geq\sim 0.10\lambda$ among surrounding waves having peak to trough amplitude about $h_0 \leq\sim 0.05\lambda$ and small steepness. In addition, there are other researchers arguing that dynamic content need to be included for a better definition. With more input on this topic, the definition may converge or we may need to adopt different definitions for rogue waves in various scenarios(i.e. shallow water rogue wave, current induced rogue wave etc.). Since we are mainly dealing with rogue waves caused by nonlinear interactions, we stick with the two conventional definitions in operation throughout the dissertation.

2.4 Notes on accumulation of rogue wave database

A computational domain of the 9×10^3 meter is considered. Waves propagating to positive x axis direction unless specified. With a given initial condition, we run the simulation for long enough time so that higher order nonlinear effects come into place. Then for a certain time window, we search for rogue waves throughout the spatial domain. If a rogue wave occurs, we record the initial condition and entire time/space series. Otherwise, we use another random seed to initialize the free surface repeat the entire process until we accumulate enough rogue waves. A sample wave field in space and time is shown in figure 2.5. We basically have many such wave fields in our database, within which one or more rogue wave events are detected after long time evolution. The high performance computational resources provided by National Energy Research Scientific Computing Center(NERSC) and Research IT (RIT) make it possible to accumulate a large number of rogue wave efficiently. The simulations are parallelized in terms of different random phases as well as sea states.
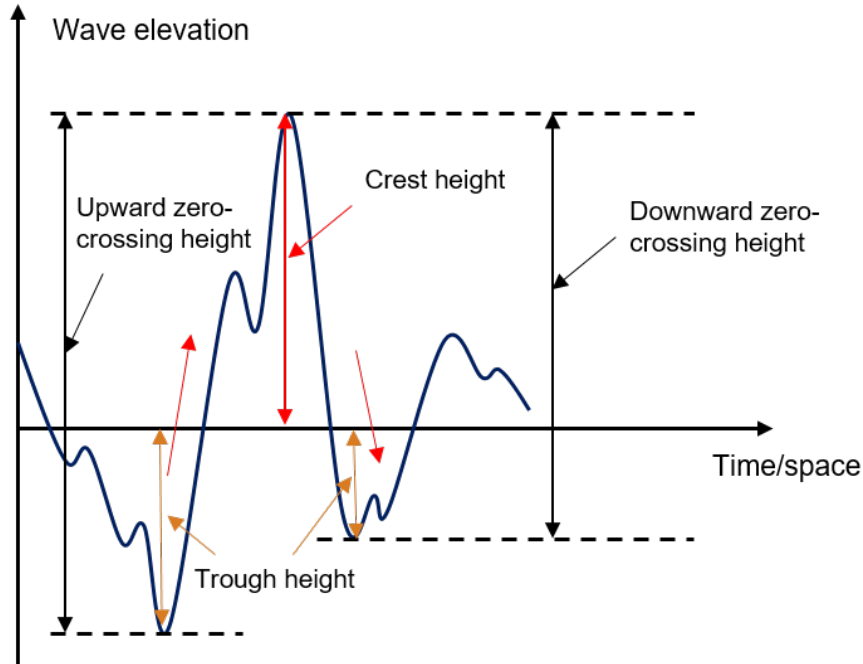
Figure 2.4: Diagram showing the definition of wave crest height, trough height and wave height. Crest height η_c is defined as the height from the positive zero-crossing peak to the mean free surface(see the height pointed by red arrow). Similarly, trough height is defined as the height from negative zero-crossing peak to the mean free surface(see the height pointed by yellow arrow). For each crest, there are two troughs either preceding or succeeding it. The shallower trough has trough height $\eta_t s$ and the deeper trough has trough height $\eta_t h$. Rogue wave height account both the upward and downward zero-crossing height(see the height pointed by black arrows), as $H_r = max(H_{up}, H_{down})$. If the maximum wave height H_r satisfies the definition in (2.20), a rogue wave is detected and H_r becomes rogue wave height.
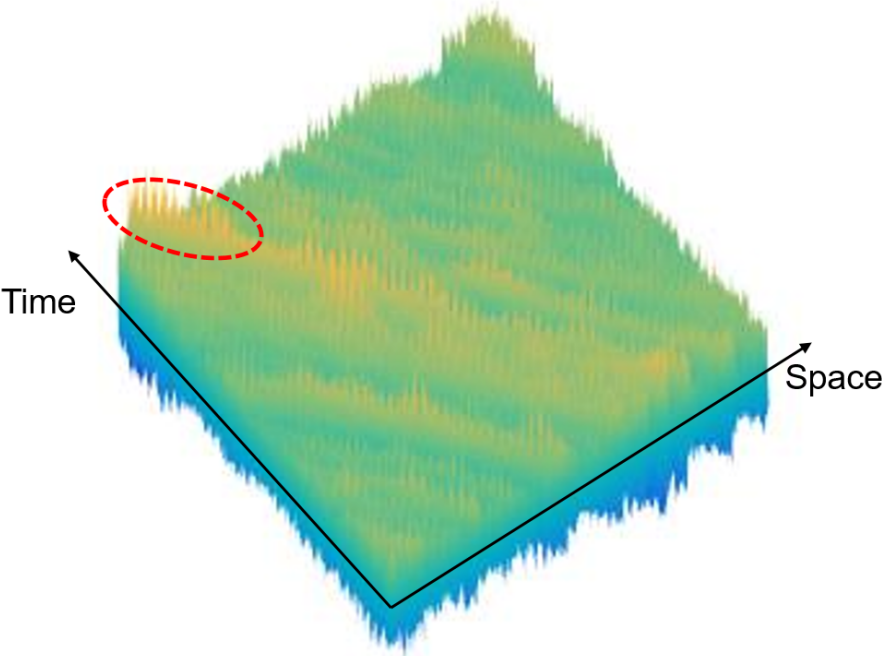
Figure 2.5: A wave field in space evolving in time. In this wave field, yellow means positive wave elevation and blue mean negative wave elevation. In the region marked by red dash line, we observed a rogue wave event, where the maximum wave height satisfies equation (2.20).

Chapter 3

Morphology of rogue waves

Here, we show through a statistical analysis that rogue waves in broadband non-breaking seas are spatially asymmetric for most realistic oceanic conditions. In addition to the top-down asymmetry due to nonlinear effects, we show that the two troughs adjacent to the rogue wave crest are generally of different depths, which is unlike the conventional picture of rogue waves with symmetric fore and aft troughs often obtained from model equations. The rogue-wave trough asymmetry is demonstrated for sea states 4 to 6 on Douglas Sea Scale. Considering the deepest trough leads to approximately 10% increase in the calculation of the mean rogue-wave height compared to previous results for rogue waves reported with symmetric troughs. This implies that estimates of rogue-wave trough-crest amplitudes based on model equations should be re-assessed upward for most realistic oceanic conditions.

3.1   Background

As discussed in chapter 1, rogue waves are usually defined as waves with peak to trough height larger than two times the significant wave height, which, in relatively common rough sea state 6 on Douglas Sea Scale, correspond to 25m or larger waves. Observations of extreme waves by the oil and shipping industry across the world's oceans [9] have revealed the unexpectedness of rogue waves: rogue waves have a much higher rate of occurrence than predicted by classical sea state spectra without the information of phases [51], and thus defy Gaussian statistics. Our understanding of the unexpected nature of rogue waves has yet significantly improved over the past few decades, and the high occurrence rate can now be explained in part by nonlinear mechanisms, such as the Benjamin-Feir instability [see e.g. 13].

In addition to the occurrence rate of rogue waves and to the predictability horizon [52], which provides information on how much in advance and how accurately we can predict the formation of rogue waves for a given sea state, the morphology of rogue waves is of fundamental importance and of growing interest in maritime design [53, 54]. A popular theoretical model for rogue wave dynamics is the nonlinear Schrödinger equation (NLS), for

which analytical solution exist. Self-focusing solutions of NLS that can potentially represent rogue waves include the first-order Peregrine Breathers [55], and the higher-order rogue wave triplets [56], triangular and polygon wave patterns [57], and circular rogue wave clusters [58]. The averaged rogue wave profile in the framework of higher-order NLS-type equations gives similar symmetric shape[8]. First-order and higher-order NLS solutions always exhibit a high level of symmetry in the horizontal-temporal (x, t) plane with respect to the main crest, hence suggesting that rogue waves have symmetric fore and aft troughs, a characteristic shared by averaged rogue wave profiles from higher-order NLS-type equations [8]. NLS-type equations are, however, limited to narrow-banded wave spectra. Therefore, a natural and important question can be formulated: should we expect rogue waves predicted by general wave models, i.e. valid for broadband spectra, to have symmetric troughs?

For a broadband wave spectrum, existing results on the morphology of rogue waves [e.g. 1] have suggested that the troughs next to the main crest have similar shape and depths. The auto-correlation function of sea surface in Gaussian sea states is also shown to exhibit symmetric averaged profile of rogue waves[59]. However, observations of rogue waves in the oceans show a different picture. For instance, while the *New Year Wave* measured near the Draupner platform [60] has preceding and succeeding troughs of almost the same depth, the Andrea wave measured in a storm crossing the North Sea [12] has troughs of substantially different depths. Furthermore, the rogue wave measured in the North Cormorant field [53] shows a much deeper trough prior to the main crest compared to the one trailing behind [see also 61, 62, 63, 64, for other observations of rogue waves]. Differences in trough depths have also been reported for the case of broadband long-crested seas (i.e. amenable to two-dimensional studies), as shown by wave basin experiments [65], few numerical simulations [20], and field measurements [66].

Here we demonstrate that rogue waves are asymmetric with respect to the main crest for broadband nonbreaking seas, which can lead to underestimation of rogue wave trough-to-crest height. This strong asymmetry (referred to as trough asymmetry) of rogue waves emerging from broadband sea states has not been obtained by previous averaging methods based on proper orthogonal diagonization (POD) [1] and auto-correlation function [59]. We will demonstrate that the trough asymmetry is more pronounced in space domain than in time domain, hence is difficult to capture with fixed buoy measurements. This may explain why the trough asymmetry has not yet been reported as a recurring feature of rogue waves in the field, since field observations are more often based on time series of wave elevation at fixed locations with buoys than on spatial profiles based on e.g. Synthetic Aperture Radar (SAR) images. Nevertheless, the reproduction of the New Year Wave in a wavetank that did yield a rogue wave with strong trough asymmetry [cf. second rogue-wave occurrence in figure 3 of 67] and a SAR image-based reconstruction of a rogue-wave spatial profile with the right trough more than three times deeper than the left trough [cf. figure 6 in 68] are evidence supporting the existence of trough asymmetry for rogue waves in the oceans.

3.2 Numerical simulations of nonlinear rogue wave profile

3.2.1 Problem formulation

Recall the Zakharov's equation from chapter 1, as

$$\eta_t = \phi_z^S(1 + \eta_x^2) - \phi_x^S \eta_x, \qquad\qquad \text{at } z = \eta(x,t), \qquad (3.1a)$$
$$\phi_t^S = -g\eta - 1/2(\phi_x^S)^2 - 1/2\phi_z^2(1 + \eta_x^2), \qquad \text{at } z = \eta(x,t), \qquad (3.1b)$$

We solve equations (3.1) with a phase resolved high-order spectral method (HOS), as discussed in chapter 2.

The initial free-surface at $t = 0$ is given by

$$\eta = \eta^{(1)} = \sum_{n=1}^{N} \sqrt{2S_{dis}(k_n)\delta k_n} \exp^{i(k_n x + \theta_n)}, \qquad (3.2)$$

where $S_{dis}(k)$ is a discretized version of the JONSWAP spectral density respect to wave number(see JONSWAP spectrum in chapter 2 for additional details). Note that both T_p and H_s change with the sea state. The initial phase distribution $\theta_n \in (0, 2\pi)$ in (3.2) is random with uniform distribution, allowing for different initial conditions for each sea state considered. Note that in order to avoid spurious modes known to contaminate numerical solutions [14], we introduce nonlinear effects gradually, i.e. we multiply nonlinear terms by $\hat{W}$ where $\hat{W}$ increases from 0 to 1 in $5T_p$.

For each sea state, we run $\mathcal{O}(1000)$ simulations so that $\mathcal{O}(100)$ rogue waves are obtained under the criterion $H_r(t) > 2H_s(t)$, where $H_r(t)$ is the maximum peak to adjacent trough height and $H_s(t) = 4\sigma_\eta(t)$ is the significant wave height. With $\mathcal{O}(100)$ rogue waves, the standard error of the mean rogue-wave profile is maximum (2%) at the peak, hence the averaged profile is statistically converged. In the simulations, we search for rogue waves in the time window $100T_p < t < 130T_p$ in order to allow high-order nonlinearities to develop (nonlinear effects beyond second-order develop in $t \sim \mathcal{O}(1/\epsilon^2) \approx 45$ for $\epsilon \leq 0.15$).

3.2.2 Validation against measurements

Comparing the time-average profile of rogue waves from our simulations in sea state 5 with the time-average profile of more than three thousand rogue waves observed in multiple locations worldwide, we find that the averaged and normalized rogue wave profile from our numerical simulations match well with the one from field measured rogue waves in multiple locations(i.e. North Sea, Gulf of Mexico, the South China Sea and the North West shelf of Australia)[9], see Fig.3.1. The definition of rogue waves used in the field[9] is $\eta_c/H_s \geq 1.25$, where η_c is the rogue wave crest. Either the crest or wave height criteria by themselves are sufficient for the definition of a rogue wave[69]. To compare with this field measured rogue

Table 3.1: Sea states considered here with relevant physical and simulation parameters, along with key results regarding rogue wave asymmetry. The peak wavenumber k_p is obtained from T_p using the linear dispersion relation for surface waves in deep water. RWs is the number of rogues waves obtained from $\mathcal{O}(1000)$ simulations and Succ gives the number of times the deepest trough succeeds the rogue wave crest such that the profile is flipped when averaging according to equation (3.4). $\bar{\eta}_D/\bar{\eta}_S$ is the mean ratio of the deepest to shallowest trough, and $\bar{H}_r = \bar{\eta}_C + \bar{\eta}_D$ is the deepest trough to crest height of averaged rogue wave profile.

Sea State	H_s (m)	T_p (s)	ϵ_p	h (m)	$k_p h$	M	$\frac{\delta x}{\lambda_p}$	$\frac{\delta t}{T_p}$	RWs	Succ	$\frac{\bar{\eta}_D}{\bar{\eta}_S}$	$\bar{H}_r$
4	1.875	8.8	$\frac{5}{10^2}$	300	15.6	4	$\frac{18}{10^3}$	$\frac{1}{128}$	48	26	2.04	2.09
5	3.25	9.7	$\frac{7.8}{10^2}$	300	12.8	1-5	$\frac{15}{10^3}$	$\frac{1}{128}$	72	39	1.95	2.28
6	5	12.4	$\frac{6.5}{10^2}$	300	7.9	4	$\frac{9}{10^3}$	$\frac{1}{128}$	57	30	2.02	2.14

wave profile, same definition is used in our numerical simulations to get the database of rogue waves. The agreement between these two indicates that rogue waves in our database from numerical simulations are likely to represent the rogue wave profile in the field in multiple locations. Moreover, the field measured averaged rogue wave profile does have a slightly shallower trough and a smaller peak, but still falls into the region bounded by the averaged profile plus/minus the standard deviation(i.e. blue dash line in Fig. 3.1). These differences can be explained by three reasons. Firstly, the averaged rogue wave profile is calculated based on field measured rogue waves collected in different regions, and hence with different H_s(i.e. from 0.12-15.4m), T_p(i.e. from 1-24.7s), and water depth(i.e. from 7.7-1311m). However, the numerical simulations focuses on one specific sea state(i.e. sea state 5 with $H_s = 3.25m$, $T_p = 9.7s$) and same water depth(i.e. 300m). These three sea states considered have relatively narrow range of significant wave height and peak period. Also, to limit the number of parameters considered, we only considered deep water case with flat seabed. Secondly, all the field measurements are associated with instrument error, which will increase dramatically when the wave is large. Thirdly, the real sea state is never perfectly unidirectional as considered in the numerical simulations. Directional spreading could potentially change the statistical properties of rogue wave profile.

3.3   Results of rogue wave profiles

3.3.1   Spatial profile

Table 3.1 summarizes the three different sea states (4, 5, 6 on Douglas scale) considered as well as key physical and numerical parameters. $\epsilon_p = k_p H_s/2$ is peak wave steepness, which is less than 0.35, the upper bound of HOS method.

The main result of the paper is the average rogue wave profile $\bar{\eta}$ obtained from two different methods and shown in figures 3.2a-b for sea state 5. The first method (method
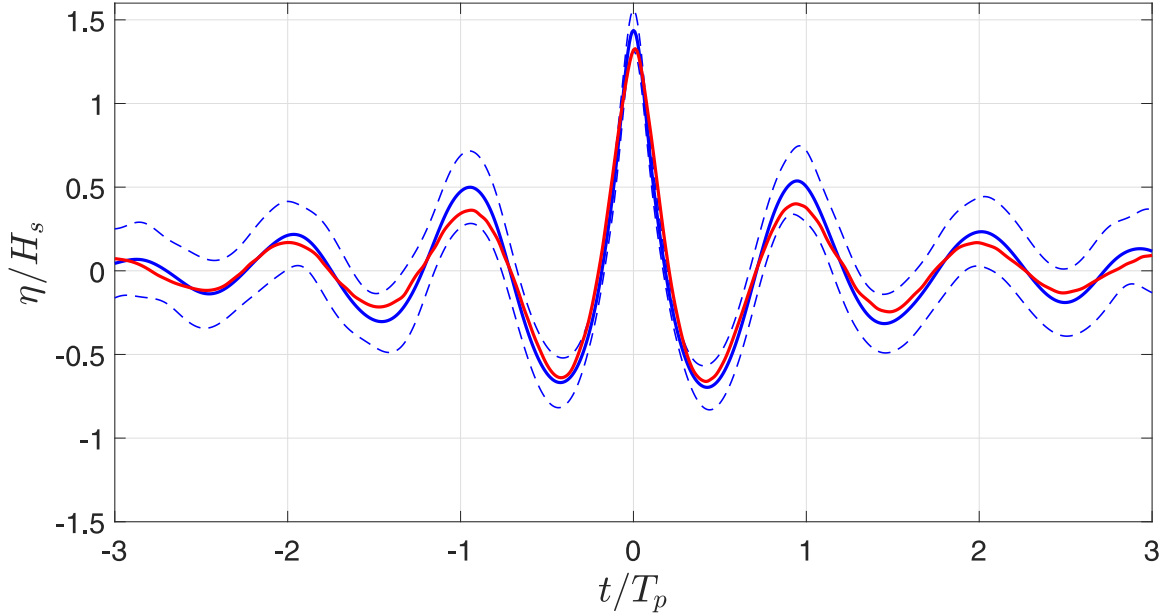
Figure 3.1: Averaged temporal rogue wave profile from field measurements(red line) v.s. our numerical simulations(blue solid line). We also plot the standard deviation plus/minus the averaged value of the numerical simulations(blue dash line). The averaged profile is calculated using approach definied in Equation (3.3) and definition of rogue waves as $\eta_c/H_s \geq 1.25$. The time of the occurrence of troughs and crests match very well bewteen the numerical simulations and the field measurements, where the maximum discrepancy is less than 6% and occurs close to the rogue wave crest. This agreement emonstrates that the rogue waves database generated numerically constitutes an appropriate representation of rogue-wave profiles in real seas. The averaged rogue wave profile from field measurements does have a slightly smaller crest height. The possible causes of the discrepency are detailed discuessed in the main text.

i-) is based on direct averaging of the crest-centered rogue wave profiles normalized by the instantaneous significant wave height $H_s(t)$, i.e.

$$\bar{\eta} = \frac{1}{\mathcal{R}} \sum_r \frac{\eta_r\left(\frac{x-x_r}{\lambda_p}\right)}{H_s(t)} \tag{3.3}$$

at the time of rogue wave occurrence ($\mathcal{R}$ the total number of rogue waves in database, x_r the location of rogue wave crest, $\lambda_p(t)$ the instantaneous peak wavelength), and results in the mean rogue wave profile shown in figure 3.2a. The second method (method ii-) consists in averaging the rogue wave profiles with flipping, i.e. calculating

$$\bar{\eta} = \frac{1}{\mathcal{R}} \sum_r \frac{\eta_r\left(p_r\frac{x-x_r}{\lambda_p}\right)}{H_s(t)} \tag{3.4}$$
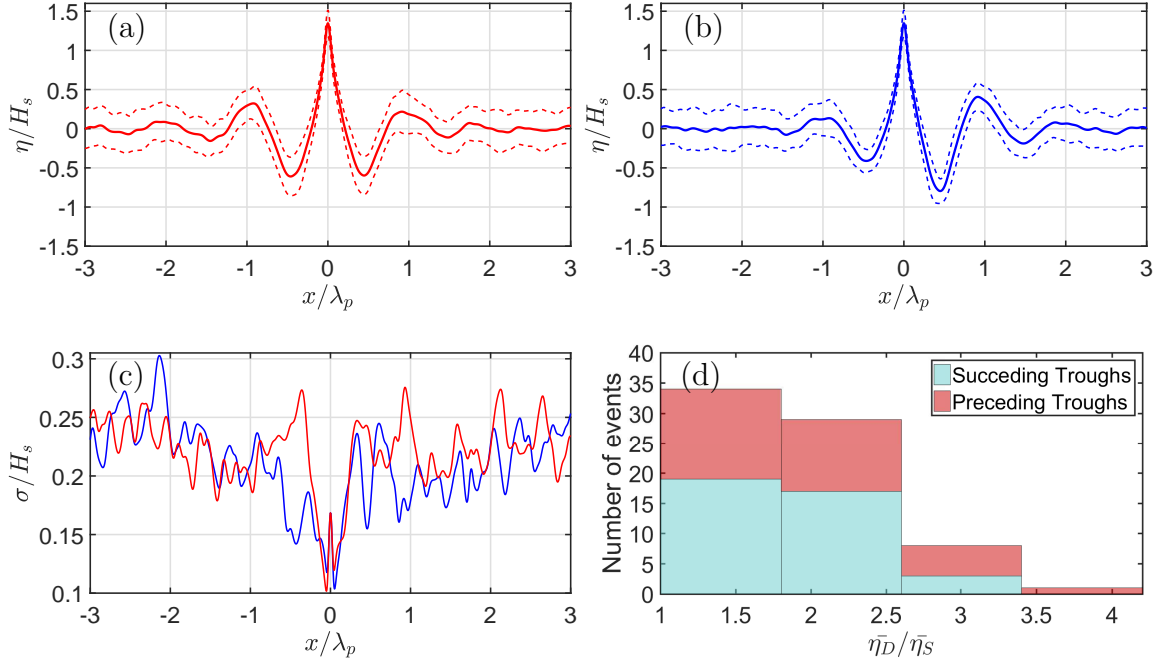
Figure 3.2: Are rogue waves spatially symmetric? From the 72 rogues waves obtained for sea state 5 and for $M = 4$ (see table 3.1), we compute the mean rogue wave profile $\bar{\eta}$ based on (a) equation (3.3) (method i-), and (b) equation (3.4) (method ii-). Method i- is commonly used in rogue wave research [1] and results in fore and aft troughs that are symmetric of each other with respect to the rogue wave crest. Method ii-, which involves flipping the troughs so as to keep the shallow troughs on the left hand-side of the crest, however, reveals the trough asymmetry of rogue waves. The standard deviation for each case is shown in figures (a)-(b) on top of the mean rogue wave profile (dashed lines) and in (c). The distribution of deep trough depth to shallow trough depth $\bar{\eta}_D/\bar{\eta}_S$ is shown in the form of two superposed histograms in (d). The bars with blue or red color are the histograms of rogue waves with trough preceding or succeeding the main crest.

where $p_r = 1$ (resp. -1) when the deepest trough precedes (resp. succeeds) the highest crest, and results in the mean rogue wave profile shown in figure 3.2b. The key point is that method -ii preserves the asymmetry of the trough depths surrounding the main crest, as can be seen from figure 3.2b, whereas method -i, which is often used in rogue wave research [e.g. 1], loses this information (see figure 3.2a). The standard deviation of the rogue wave profiles is plotted in figure 3.2c for each approach. The standard deviation is high close to both trough locations when using method i-, suggesting that the trough depths distribution is widespread on both sides of the main crest. The standard deviation using method ii- is 20% and 50% less than that of method i- at succeeding and preceding trough, respectively. Figure 3.2d shows the distribution of the deep-to-shallow trough depth ratio in the form of two superposed histograms; the histogram filled with blue (resp. red) color highlights the number of times the deepest trough is succeeding (resp. preceding) the main crest. redBecause the histograms show about the same number of events(i.e. 54% of succeeding troughs and 46% of preceding troughs), the deepest trough occurs on average before the main crest as often as behind the main crest. This explains why method i- loses the information on the rogue wave asymmetry: the deeper trough can occur on either side of the rogue wave, such that direct averaging gives the same mean fore and aft trough depth. We find that more than half the rogue waves have a deep trough more than twice as deep as the shallow trough. On average, the deep-to-shallow trough depth ratio is $\bar{\eta}_D/\bar{\eta}_S = 1.95$, and the deepest trough-to-crest height $\bar{H}_r = \bar{\eta}_C + \bar{\eta}_D$ calculated from method ii- is 2.14, which, compared to 1.96 for method i-, is approximately 10% larger (see table 3.1). It is important to note that, although not shown, normalized spatial profiles calculated using method ii- look similar qualitatively and quantitatively for all sea states (i.e. 4, 5 and 6). In particular, the normalized crest-to-trough height in sea state 4 and 6 is only 2% and 0.16% less than that in sea state 5, and the deep-to-shallow trough depth ratio changes by less than 4% both in sea state 4 and 6.

Comparable numbers of rogue waves with deeper rear/front troughs are identified for all sea states 4, 5 and 6, where the portions of deep rear/front trough are 54%/46%, 54%/46% and 53%/47% respectively. This is consistent with the observations in [70] in a similar sea state as sea state 5(see Fig. 10(a) where H_s=3.5 m, T_p=10s). As the steepness of sea states increases, rogue waves with deep rear trough become more dominant due to enhanced nonlinear effect(see Fig. 10(b) in [70] and Fig. 24(a) in [1]).

3.3.2   Effect of nonlinearity

Nonlinear effects are of significant importance in rogue wave research, and as a result here we carefully look at the effect of changing the order of nonlinearity on the rogue wave asymmetry. The results are shown in figure 3.3 and can be summarized as follows: (1) the rogue wave trough asymmetry is captured for all orders of nonlinearity, with only +4% (+12%,+7% and +0.9%) discrepancy in $\bar{\eta}_D/\bar{\eta}_S$ for M=1 (M=2, 3 and 4) compared with M=5, (2) the linear model (M=1) strongly underestimate the mean rogue wave height and crest height (i.e. -8% and -19% compared to $M = 5$), (3) the averaged rogue wave profile is overestimated
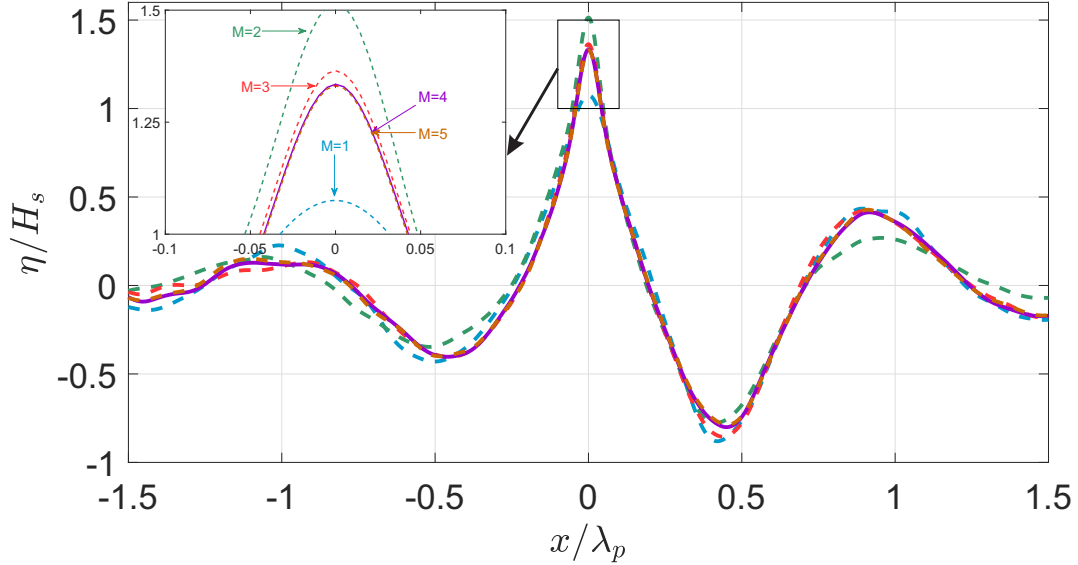
Figure 3.3: Effect of nonlinearity on the average rogue wave profile in sea state 5 for $M = 1 - 5$. The trough asymmetry is obtained for all M using method ii-, with $\bar{\eta}_D/\bar{\eta}_S$ (deepest to shallowest trough ratio) changing by less than 4% between $M = 1$ and $M = 5$. In agreement with previous works [2], the crest height is affected by higher nonlinearities $M = 3$, 4 and 5 (c.f. inset figure).

for $M = 2$ (+7% and +14%) and (4) the results for $M = 3$, 4 and 5 are in quantitative agreement (4.3% and ¡1% discrepancy in rogue wave heights for $M = 3$, 4 compared to 5). The convergence of the rogue wave profile with $M \geq 3$ confirms that cubic nonlinearity play a dominant role not only in the generation mechanism and occurrence rate of rogue waves [71, 72], but also in shaping the rogue wave crests and troughs. That the rogue wave trough asymmetry is qualitatively obtained for all M suggests that the primary mechanism responsible is the dispersive dynamics of ocean waves. This result is in agreement with the fact that the distribution of trough depths around the main crest is mostly random, and that the distribution will be wide spread in all realistic oceanic cases. We would like to note that the effect of the trough asymmetry can also be observed from the relatively small ratio of $\bar{\eta}_C/\bar{\eta}_D = 1.69$ ($M = 4$), which we obtain when considering the deep trough $\bar{\eta}_D$ using method ii-. This is much smaller compared with $\bar{\eta}_C/\bar{\eta}_D = 2.21$ if we use method -i (for which $\bar{\eta}_D \approx \bar{\eta}_S$), as well as the value obtained using the third order simulations of MNLS equations, which gives the ratio $\bar{\eta}_C/\bar{\eta}_D = 2.2$ [8].

Thus, the nonlinearity strongly influence the relative depth between crest and deep trough

$\frac{\bar{\eta}_C}{\bar{\eta}_D}$ but not the trough symmetry. Even though the profile symmetry respect to the main peak is not a nonlinear property, we still use $M = 4$ for all the result presented since we want to correctly predict the rogue wave height.

3.3.3 Temporal profile

In figure 3.4, we finally show the mean rogue wave profile averaged in time for sea state 5, following methods i- and ii– but with spatial variables in equations (3.3)-(3.4) replaced by temporal variables. The temporal wave signal used for averaging is obtained from the simulations using the recorded free-surface elevation at the midpoint between the highest peak and deepest trough of the rogue wave, which is the location that is most likely to capture the high crest and low trough in time. Compared to the mean rogue wave profile in space, the temporal average with flipping displays a relatively small asymmetry. The standard deviation using method ii- is yet still smaller than using method i- (see figure 3.4c), confirming that the rogue wave profile in figure 3.4b is in better agreement with individual rogue waves than in figure 3.4a. Similar to figure 3.2d, two superposed histograms of the deep-to-shallow trough depth ratio in time domain are shown in 3.4d. Again, deeper troughs can travel either preceding or succeeding the main crest. On average, the deep-to-shallow trough depth ratio $\bar{\eta}_D/\bar{\eta}_S$ is 1.33 for method ii-, and 1.00 for method i-. The largest trough-to-crest height $\bar{\eta}_C + \bar{\eta}_D$ calculated from method ii- is 2.28, which, compared to 2.18 for method ii-, is 4.9% larger.

3.3.4 Other effects on spatial profile

In this section, we further investigate other effects on spatial profile using approach in Equation (3.4), including sea roughness, water depth and the crossing sea state.

The previous results are obtained only in sea state 5. Now we evaluated how sea state roughness could potentially affect the rogue wave profile. Averaged wave elevation for sea state 4, 5 and 6 are plotted in Fig. 3.5. 48, 72 and 57 rogue waves are screened out respectively in sea state 4, 5 and 6. The normalized rogue wave η/H_s shows identical shape across the sea states considered. We carefully derived the similarity in the normalized linear wave profiles with given sea state parameters across these sea states, as in Appendix A. Note that the similarity exists not only in linear case, but also for the nonlinear case considered here(i.e. $\epsilon <\sim 0.1$.) This similarity could break if we consider wave field with high steepness.

The possible application of this observation could be in the design of ships and offshore structures. For example, in the scenario where extreme wave loads need to be taken into account, the identical rogue wave height H_r and characteristic wave length λ_r can be calculated based on the background sea state data and used in design criterion.

Rogue wave profiles in deep water has been analyzed carefully so far. Now we consider the scenario where water depth is intermediate(i.e. h = 50m). The parameters used in the simulation and the comparison of averaged rogue wave profile are presented in figure 3.6.
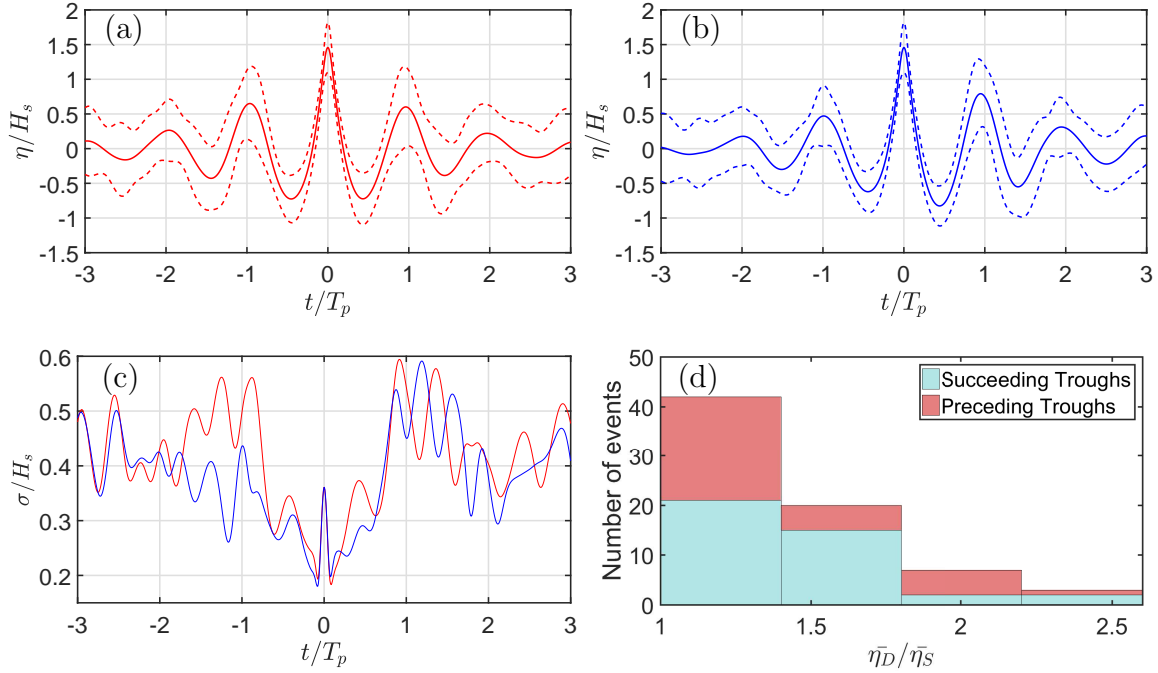
Figure 3.4: Mean temporal rogue wave profile based on (a) method i-, and (b) method ii- for averaging (corresponding to equation (3.3) and (3.4) with spatial variables substituted with time variables). The trough asymmetry in time is much less pronounced than in space (see figure 3.2). The standard deviation for each case is shown in figures (a)-(b) on top of the mean rogue wave profile (dashed lines) and in (c). $\bar{\eta}_D$ to $\bar{\eta}_S$ distribution is shown in the form of two superposed histograms. The bars with blue or red color are the histograms of rogue waves with trough preceding or succeeding the main crest.

Various sea conditions need to be considered to in order to further quantify the statistics of shallow water rogue waves.

It has been recognized that rogue waves occurs more frequently in crossing seas, which is two wave groups propagating in opposite direction in 2 dimensional framework. Here we consider waves, still represented by JONSWAP spectrum, can travel in either positive or negative x direction. The averaged profile is then compared with that in unidirectional seas, as in figure 3.7.

3.4   Summary

The trough asymmetry of rogue waves reported in this Letter is a new step toward careful characterization of the most extreme waves in the oceans, which deserve special attention owing to their destructive power. Indeed, the morphology of rogue waves is of significant
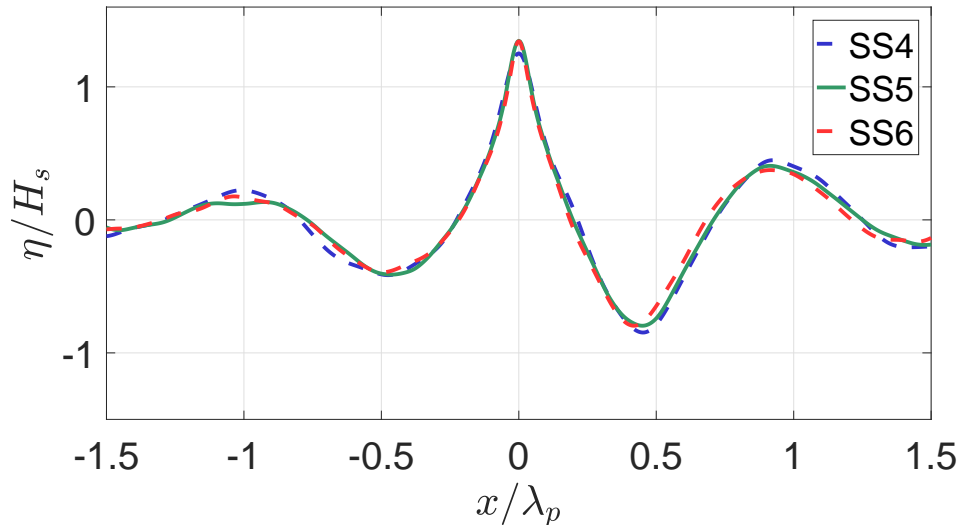
Figure 3.5: The average profile of normalized peak-centered rogue waves in sea state 4(blue dash line), 5(green solid line) and 6(orange dash line). It is important to note that, although not shown, spatial profiles calculated using method ii- are found almost identical for all sea states (i.e. 4, 5 and 6). The rogue wave crest is smaller in sea state 4 than that in sea state 5 and 6. This discrepancy is around 5%. In particular, the normalized crest-to-trough height in sea state 4 and 6 is only 2% and 0.16% less than that in sea state 5, and the deep-to-shallow trough depth ratio changes by less than 4% both in sea state 4 and 6.

importance for naval architects and man-made offshore structures, because rogue wave shapes directly influence structural loads, survivability and hence the safety of seamen. We find that the deepest trough extends on average twice as deep as the shallowest one for all sea states 4, 5, and 6 on Douglas scale, which implies an enhancement of the average trough-to-crest height from 1.96 to 2.14 times the significant wave height when considering the deepest trough instead of the trough depth average. The randomness of the trough depths distribution (including preceding/succeeding) is a result of the main mechanism for the asymmetry, which is the linear dispersion of waves. Averages of rogue wave profiles in space thus lose the information on the trough asymmetry when performing direct averaging techniques that remove the preceding/trailing trough depth difference [1].

The asymmetry of rogue waves in unidirectional seas has not been the focus of previous studies, to the best of our knowledge, potentially because rogue waves reported from the field are often based on buoys' motion in time, for which the signal is much less asymmetric than in space (compare figures 3.2 and 3.4). It may be also because most of our theoretical understanding has come from NLS models, for which solutions exhibit high levels of trough symmetry. NLS-type equations are limited to narrow-band seas, where the dispersion is weak because waves are assumed quasi-monochromatic. This may explain the higher symmetric
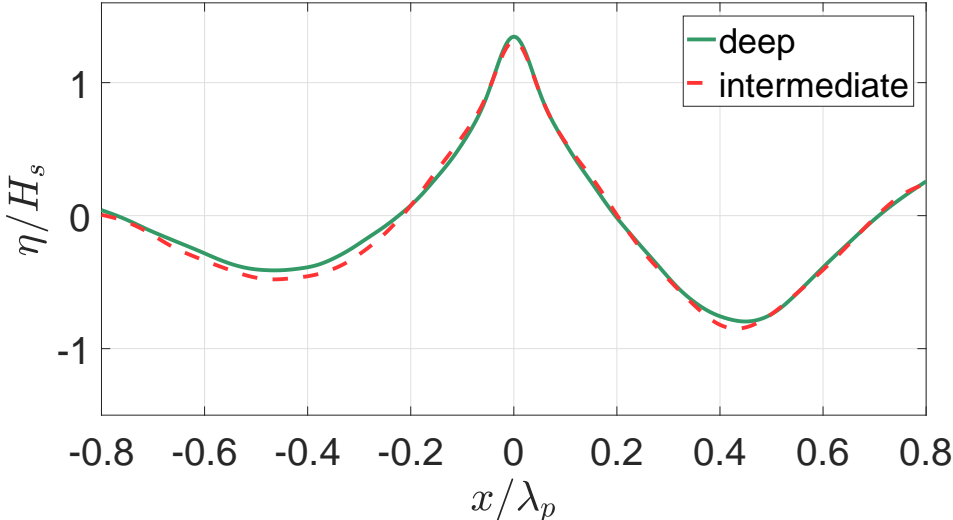
Figure 3.6: Averaged profile of rogue wave with water depth 300 meter and 50 meter, representing deep water and intermediate water depth case. Sea state 5 is considered for both cases. The corresponding $k_p h = 12.8$ and 2.2 respectively. The peak wave length is slighter longer in deep water than than in intermediate water depth. We observed that the averaged rogue wave has slightly deeper troughs and smaller crest in shallower water.
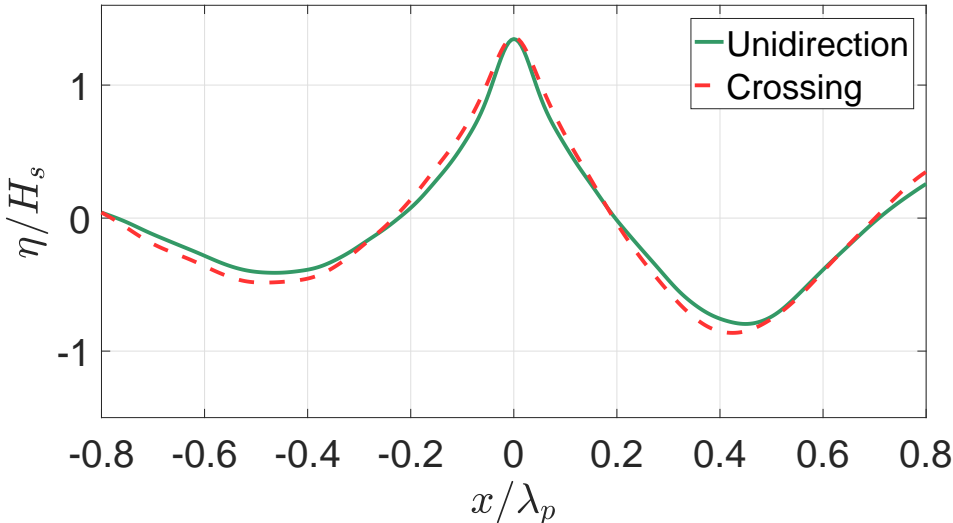
Figure 3.7: Comparison of statistically averaged rogue wave profiles using equation (3.4) (method ii-) in sea unidirectional(green solid line) and crossing seas(orange dash line). We observed that averaged rogue wave in unidirection seas have a slightly narrow crest.

rogue wave profile of solutions of NLS. It is thus not surprising that solutions to Zakharov equations can show high trough asymmetry.

We expect our results to be relevant to rogue waves in three dimensions, because the mechanism responsible for trough asymmetry is wave dispersion, which dominates wavefield rearrangement in most oceanic conditions. The trough asymmetry of rogue waves in three-dimensions is, however, expected to be more complicated as a result of directional spreading and three-dimensional hydrodynamic instability. For instance, it has long been known that rogue waves can exhibit a fore/aft asymmetry, with the trough following the rogue wave crest bigger than the one preceding (the so-called horseshoe shape), as a result of three-dimensional (class II) modulational instability [73]. Which one of dispersion or modulational instability is the primary responsible for the formation of rogue waves with asymmetric troughs in the real ocean emerges as a question that would be worth answering.

Chapter 4

Effect of oceanic stratification

4.1 Background

In spite of their inherent unpredictability, the prediction of rogue waves using direct simulation is becoming more promising ever since[43]. Hence, efforts have been intensified very recently to seek the possibility of predicting rogue waves. For example, using the Peregrine soliton as a prototype of rogue waves, Akhmediev[44] observed that solitons have a triangular spectrum during their evolution stage which may serve as an early warning of the formation of rogue waves. Latifah[74] explored the predictability of extreme waves by investigating the phase coherence using the power spectrum and the phase information, and found that the extreme waves can be predicted well by minimizing the variance of the total wave phase. Chalikov[75] investigates some properties of rogue waves by directly analysing O(1000) numerical results and calculates the probability of their occurrence. Xiao et al.[1] used direct simulation based on high-order spectral method, originally developed by Dommermuth[46] to study the occurrence and dynamics of rogue waves in 3-dimensional deep water. In addition, Alam[52] has implemented heavily computational experiments on the predictability horizon for rogue waves in the homogeneous fluid for various sea states using the high-order spectral method, where sea state is a general representation of the wave elevation statistics.

Most efforts for predicting waves in the ocean have focused on homogeneous flows [76, 77, 78]. On the other side, the real ocean is usually stably stratified due to the vertical variation of the salinity and/or temperature[79, 80]. The density stratification effect on small, linear oceanic surface waves is commonly very negligible. This is mainly attributed to the fact that the upper part of the ocean known as the mixed layer is homogenized due to the forcing and active turbulence from wind stress at the ocean free-surface. However, this is not the case for large amplitude highly nonlinear rogue waves whose substantial effects can be extended into the deep ocean and also be impacted by internal waves which are caused by buoyancy forces arising from the density stratification in the ocean. In this condition, energy is exchanged between the surface wave and internal wave which also alters the surface wave dynamics, i.e. in the form of triad resonance[45, 41] and the modulation and master mechanism[81].

Theoretical analysis of two dimensional Korteweg-de-Vries (KdV) equation has been used to represent abnormal wave surface with the stratification effect[39]. On the other hand, the effect of stratification on highly nonlinear waves (i.e. rogue waves) has not been investigated to date. Hence, it is crucial to explore this effect as using the homogeneous fluid model may lead to errors such as over- or underestimation of the rogue wave height. Underestimation in the wave height can be economically and humanly dangerous because the erroneous warning system fails to alert people to take proper actions in advance to reduce the disaster risk. Overestimation is conservative, however, can cause a waste of time and money. Hence, with the advancement of our knowledge on rogue waves and the increase in the computational power, it is critical to consider the density stratification effect in these scenarios for rogue waves predictability.

The stable stratification can be continuous where the density continuously increases in the fluid depth. Also, it can be composed of two homogeneous layers of water with distinct densities where the lighter fluid overlies a heavier fluid, separated by a surface known as the thermocline. The thermocline has a very sharp density gradient and is the location for the formation and propagation of internal waves. In the real ocean, density profile is continuous over the depth. However, field observations demonstrate that the stratified deep ocean can be estimated as a two-layer fluid system where the homogeneous mixed layer overlies the heavier fluid, which approximately has a constant density (e.g. Sigman, Jaccard, Haug 2004). The most important feature of the stratified ocean is retained in the two-layer fluid model where both barotropic and baroclinic modes are taken into account[82]. Also, in the two-layer fluid system, the interaction of surface waves and internal waves can be calculated significantly easier. Overall, the two-layer fluid model is more accurate and realistic than the homogeneous fluid model, and hence has been widely used for modeling ocean waves dynamics[83, 84, 85]. In this study, we employ the two-layer fluid model in order to investigate incorporation of density stratification and its efficacy for better and more realistic modeling of oceanic rogue waves. Also, the predictability error due to employing homogeneous fluid models for predicting ocean rogue waves in different sea states will be investigated.

In this chapter, rogue waves prediction is fulfilled by solving the wave evolution equation while the current sea state is obtained using the radar satellite data. The adoption of synthetic aperture radar (SAR) together with the advanced inversion technique give accurate information about the wave elevation over a large spatial domain. Radar scattering of surface ocean waves has been extensively studied and validated, thus many wave prediction models are based on the data from SAR images[86]. The SAR data can also be used for the prediction of rogue waves[13] which helps obtain the ocean stratification parameters including the upper layer depth and the density ratio[87][88] (i.e. the ratio of the upper layer density to the lower layer density) which are shown to be in good agreement with the cruise measurements[88][89]. However, given the fact that the computational cost of the two-layer fluid model is significantly higher than that of the homogeneous fluid model, it is imperative to investigate the efficacy of employing two-layer fluid model to predict rogue waves. This implies that stratification effects on the rogue wave prediction have to be accounted for by comparing the heights of predicted rogue waves in the homogeneous fluid model with the

actual rogue waves in the stratified fluid. To this end, we solve the fully nonlinear Euler equation to quantify the predictability of rogue waves in two-layer stratified ocean. The important statistical results are extracted through analysis of enormous results obtained from numerical simulations implemented for a large number of different initial conditions.

4.2   Problem formulation

In order to predict the wave field, Euler equations need to be solved numerically for the homogeneous and two-layer fluid where the initial conditions are similar for both models at the free-surface. Also, in order to only examine the stratification induced effect on the prediction of rogue waves and hence to avoid any other unwanted effects (i.e. interaction of surface waves and bottom undulations), the bottom is chosen uniform and without slope. Recall the problem formulation in chapter 2 where surface wave evolution is governed by the fully nonlinear Euler equations and a velocity potential ϕ can be to describe such wave dynamics. The two-dimensional governing equation together with the boundary conditions in the homogeneous fluid read:

$$\nabla^2 \phi = 0 \qquad\qquad -h < z < \eta \qquad (4.1a)$$
$$\phi_{tt} + g\phi_z + [\partial_t + 1/2(\nabla\phi \cdot \nabla)](\nabla\phi \cdot \nabla\phi) = 0 \qquad\qquad z = \eta \qquad (4.1b)$$
$$\phi_z = 0 \qquad\qquad z = -h \qquad (4.1c)$$

(4.1a) is the governing equation which is valid over the whole fluid domain. (4.1b) is the combined free surface boundary condition and (4.1c) is the no penetration bottom boundary condition. The wave elevation and velocity potential can be solved up to an arbitrary time T for a given initial condition.

In the two-layer fluid flow, we assume two homogeneous, inviscid, irrotational and incompressible fluids with different densities where each layer can be identified with the potential theory as shown in equations (4.2a) and (4.2b) in the following. In this case, in addition to separate governing equations for each layer, extra boundary conditions which describe the interface (i.e. same vertical position and vertical velocity for each layer at the interface) need to be taken into account. The two-dimensional governing equations together with the boundary conditions in the two-layer fluid model read:

$$\nabla^2 \phi_u = 0, \qquad\qquad -h_u + \eta_\ell < z < \eta_u \qquad (4.2a)$$
$$\nabla^2 \phi_\ell = 0, \qquad\qquad -h_u + h_\ell < z < -h_u + \eta_\ell \qquad (4.2b)$$
$$\phi_{u,tt} + g\phi_{u,z} + [\partial_t + 1/2(\nabla\phi_u \cdot \nabla)]$$
$$(\nabla\phi_u \cdot \nabla\phi_u) = 0, \qquad\qquad z = \eta_u \qquad (4.2c)$$
$$g\eta_u + \phi_{u,t} + 1/2(\nabla\phi_u \cdot \nabla\phi_u) = 0, \qquad\qquad z = \eta_u \qquad (4.2d)$$

$$\mathcal{R}\{\phi_{u,tt} + g\phi_{u,z} + 1/2(\nabla\phi_u \cdot \nabla\phi_u)_{,t}+$$
$$\eta_{\ell,t}[\phi_{u,t} + 1/2(\nabla\phi_u \cdot \nabla\phi_u)]_{,z}$$
$$- g\eta_{\ell,x}\phi_{u,x}\} - \{\phi_{l,tt} + g\phi_{\ell,z}$$
$$+ 1/2(\nabla\phi_\ell \cdot \nabla\phi_\ell)_{,t} + \eta_{\ell,t}[\phi_{\ell,t}$$
$$+ 1/2(\nabla\phi_\ell \cdot \nabla\phi_\ell)]_{,z} - g\eta_{\ell,x}\phi_{\ell,x}\} = 0, \qquad z = -h_u + \eta_\ell \qquad (4.2e)$$
$$\eta_{\ell,t} + \eta_{\ell,x}\phi_{u,x} - \phi_{u,z} = 0, \qquad z = -h_u + \eta_\ell \qquad (4.2f)$$
$$\eta_{\ell,t} + \eta_{\ell,x}\phi_{\ell,x} - \phi_{\ell,z} = 0, \qquad z = -h_u + \eta_\ell \qquad (4.2g)$$
$$\phi_{\ell,z} = 0, \qquad z = -h_u - h_\ell \qquad (4.2h)$$

(4.2c) is the combined free surface boundary condition and (4.2d) is the dynamic free surface boundary condition. (4.2e) is the combined interfacial boundary condition. (4.2f) and (4.2g) are the interfacial kinematic boundary conditions for the upper layer and the lower layer, respectively and (4.2h) is the bottom boundary condition. The subscripts u and l refer to the upper layer and the lower layer, respectively. The density ratio $\mathcal{R} = \rho_u/\rho_l$ is always less than 1 for the stably stratified ocean. Both (4.1) and (4.2) are solved numerically using the phase revolved high-order spectral (HOS) method.

In reality, the initial condition is based on the wave field reconstructed from SAR images or ship-born radars. However, to conduct numerous computational tests, the initial computational surface wave elevation is characterized by the JONSWAP spectrum. Indeed, many of the rogue wave predictive models also rely on waves initially defined by JONSWAP spectrum[90, 91, 75]. The intensity of the power spectral density is controlled by several parameters α_p, β and γ, as given in (4.3). The definition on these parameters are stated in chapter 2.

$$S(\omega) = \frac{\alpha_p g^2}{\omega^5} \exp(\beta)\gamma^\delta, \qquad (4.3)$$

For a given spectrum density function $S(\omega)$, the wave field data is initialized by the linear superposition of waves with amplitude defined as $a = \sqrt{2S(k)dk}$. In this equation the power spectrum is changed from a function of the frequency to that of the wavenumber using the relation $S(k) = S(\omega)C_g$, where $C_g = d\omega/dk$ is the group velocity. Each frequency component has a phase randomly generated from 0 to 2π. The initial wave elevation η_i and velocity potential ϕ_i are calculated using linear wave theory either in the homogeneous fluid or the two-layer fluid model. When the linear solutions are used as the initial conditions to solve the nonlinear wave evolution equations, i.e. (4.1) and (4.2), spurious wave modes develop. To avoid this issue, the nonlinear terms are introduced gradually from $t = 0$ to $t_{pre} = 5T_p$, where $T_p = 2\pi/\omega_p$ is the peak period. This is achieved by multiplying the nonlinear terms by a factor $\hat{W}$, which increases smoothly from 0 to 1 within time $[0, t_{pre}]$[14].

Since the directly measured wave field is barely linear, the nonlinear initial conditions need to be extracted from the linear initial conditions. One specific feature of the set of

equations introduced in (4.1) and (4.2), which helps resolve this challenge and reach appropriate nonlinear initial conditions, is their reversibility in time. This means that if (η_f, ϕ_f) is a solution for forward time (i.e. $t = +T$) with (η_i, ϕ_i) as the initial conditions, then (η_i, ϕ_i) is the solution of this set of equations when $t = -T$ with the initial conditions $(\eta_f, -\phi_f)$. To benefit from this feature, if for a given linear initial condition the rogue wave is detected at T_i, then the simulation will continue until $t_f = T_i + T_s$ and the elevation and velocity potential (η_f, ϕ_f) will be recorded at t_f. Due to reversibility, using the nonlinear initial conditions as $\eta_{ni} = \eta_f$ and $\phi_{ni} = -\phi_f$, should result in the same rogue wave at $t = T_s$.

In order to filter the linear initial conditions that result in a rogue wave at $t = T_i$, it is necessary to have an appropriate mathematical definition for rogue waves. There are several definitions for such abnormal waves. The most commonly used approach for defining rogue waves is the criterion of the wave height. In this approach if the maximum trough to peak height H_r is larger than twice of the significant wave height H_s (i.e. $H_r > 2H_s$), the wave is considered as a rogue wave. $H_s = 4\sigma$, where σ is the standard deviation of the wave elevation η. In this study, we employ this method for defining the rogue waves.

While the approach for detecting rogue waves might look simple and straightforward, it would never be possible without recourse to prohibitively expensive numerical simulations. The most challenging part in the computation process is filtering the desired initial conditions. Since the occurrence of the rogue waves is a rare event, enormous cases need to be simulated before we can reach a statistical converged result.

4.3 Results

4.3.1 Approach I

Firstly, the nonlinear initial conditions are obtained from the two-layer fluid model with different $\mathcal{R}$ and thermocline depth (i.e. different h_u). Then we use these selected initial conditions (i.e. the nonlinear surface wave initial conditions η_{si}, ϕ_{si}) in the homogeneous fluid model. This approach is illustrated in Figure 4.1. This is a realistic approach because the predicted rogue waves in the two-layer fluid are the actual rogue waves occurring in the stratified fluid. If the homogeneous fluid model is used for the prediction of rogue waves for stratified ocean, the error without taking into account the stratification can be quantified by comparing the predicted rogue wave in the homogeneous fluid model with the actual rogue wave height obtained from the two-layer fluid model with $\mathcal{R} < 1$.

To evaluate the suitability of using the homogeneous fluid model for the prediction of rogue waves in the stratified fluid, three parameters in the two-layer fluid can be altered and the sensitivity of the homogeneous model prediction accuracy to these parameters should be investigated. These influential parameters are: 1) Density ratio $\mathcal{R}$, 2) Prediction time T_p and 3) Thermocline to overall water depth ratio h_u/h. We will discuss these parameters briefly here. 1) The density ratio $\mathcal{R} = \rho_u/\rho_l$ is a measure of the strength of stratification in the ocean. $\mathcal{R}$ varies due to heating and salinity in different parts of the ocean. In this
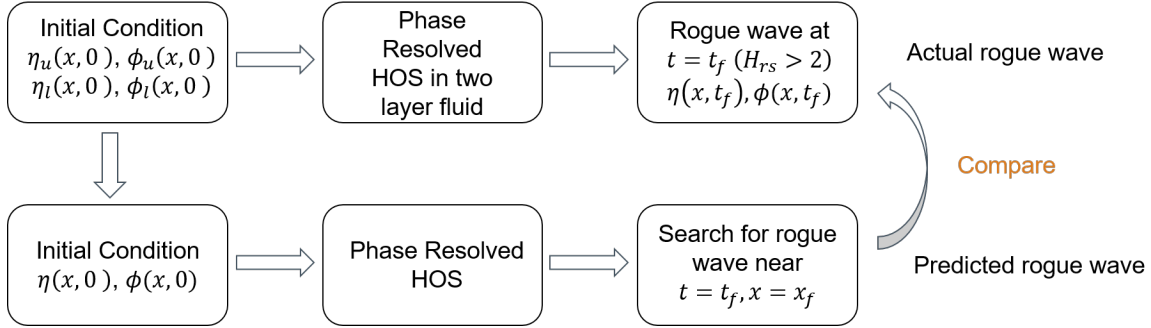
Figure 4.1: Diagram of the procedure in comparing rogue waves in two-layer stratified fluid and homogeneous fluid. Internal waves may be generated as a result of the interaction of surface waves, hence using model based on homogeneous fluid model may not be adequate in estimating rogue wave event in the stratified fluid. We quantify the feasibility of using homogeneous fluid model by comparing the predicted rogue wave height of using homogeneous fluid model with the actual height in 2-layer stratified fluid.

study, we use four different density ratios as $\mathcal{R} = 1, 0.99, 0.95, 0.9$. For $\mathcal{R} = 1$, as shown in Figure 4.2, we compare the predicted rogue wave in one specific initial condition with the actual rogue wave in the two-layer stratified fluid. The predicted wave is in great agreement with the actual wave with negligible difference. It is an expected result as $\mathcal{R} = 1$ means no density difference between two layers, which is similar to the homogeneous model.

However, these two are intrinsically different as in the two-layer model, unlike the vertical velocity, the horizontal velocity at the interface in each layer may be different. $\mathcal{R}=0.99$ represents the typical stratification in the ocean[79]. In some strongly stratified cases, $\mathcal{R}$ can reach as low as 0.95[92]. $\mathcal{R} = 0.9$ which is never possible in the ocean is considered in this dissertation to show the general effect of stratification. 2) Prediction time T_p is the time before the occurrence of the rogue wave for which we use the initial conditions in order to perform the prediction. The predictive error obviously depends on how advanced in time we need to predict. 3) Thermocline to overall water depth ratio h_u/h is another influential parameter since the baroclinic modes are developed through nonlinear interactions between the surface waves and internal waves. The depth ratio is altered to ensure kh_u varies from shallow water to deep water. Evaluating all these parameters causes the computational efforts are extremely heavy as numerous initial conditions need to be screened out if one parameter is changed.

In order to evaluate the efficacy of the introduced approach, we compare the predicted rogue waves with the actual rogue waves heights. To do so, we detect the maximum rogue waves with a trough to peak height H_r. The significant wave height at the time of rogue wave occurrence is H_s. Then the normalized rogue wave height can be defined as the height ratio $H_{rs} = H_r/H_s$ in the homogeneous fluid system. Similarly, $H_{rs}^{(2)} = H_r^{(2)}/H_s^{(2)}$ is defined as normalized height of the rogue wave in the two-layer fluid model. The rogue waves are
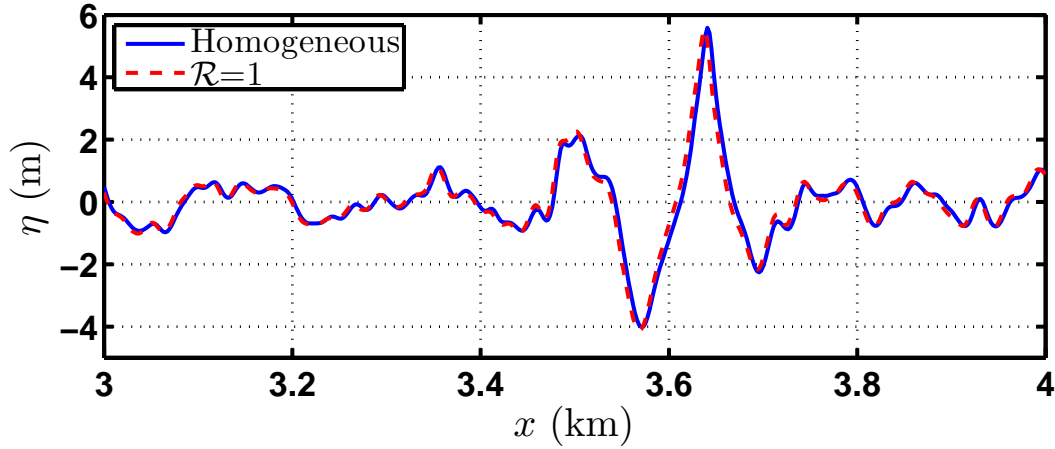
Figure 4.2: Comparison of the predicted rogue wave in homogeneous fluid and the actual rogue wave in the two-layer stratified fluid with $\mathcal{R}=1$ for a specific initial condition in sea state 5. The original rogue wave (i.e. red dash line) has height $H_r = 2.976H_s$, and the predicted rogue wave (i.e. blue solid line) height is $H_r = 2.954H_s$. The error in predicted wave height is less than 1%. This observation serves as the base of quantifying effect of stratification by comparing rogue waves in two-layer stratified fluid and homogeneous fluid.

detected in the two-layer fluid model with the height ratio $H_{rs}^{(2)}$. Then the predicted rogue waves in homogeneous fluid have the height ratio H_{rs}. Then the prediction accuracy is defined as in in (4.4).

In order to guarantee a well predictability, in addition to small difference in H_{rs}, the models need to show good agreement in the time and location that the rogue waves occur. So rogue waves are sought within the time window $T_s - 5T_p < t < T_s + 5T_p$ and space window $x_r - 5\lambda_p < x < x_r + 5\lambda_p$, where λ_p is the wave length of the wave with peak period and x_r is the peal location of the rogue waves.

$$A = \frac{H_{rs}}{H_{rs}^{(2)}} \times 100\% \tag{4.4}$$

We implement the simulations for a given sea state by using equation (4.3) for defining the initial amplitudes and frequencies. Although the computational effort required for approach 2 is considerably lower than that of approach 1, we mainly focus on the predictability of approach 1 due to its suitability and realistic nature. In approach 1, three sea states 4, 5 and 6 are considered, which represent the moderate, rough and very rough sea states, respectively. We only consider sea state 5 for approach 2. Sea states 4, 5 and 6 have H_s=1.875 m, 3.25 m and 5 m with T_p=8.8 s, 9.7 s and 12.4 s, respectively. Although most frequent sea states have characteristic H_s less than 0.5 m and $T_p \sim 4$ s[93], we use considerably higher sea states in our study as rogue waves with larger heights tend to develop in these sea states and hence their consequences are more perilous to properties and lives. For each of

the considered sea states with a given set of parameters (i.e. $\mathcal{R}$, T_p and h_u/h), order of 1000 random phases are altered through numerous numerical simulations and 48 qualified initial conditions are selected. For each of these initial conditions, a comparison is made between the predicted rogue waves and the original waves to assess the prediction efficiency. For both the homogeneous and two-layer fluid model, parameters used in numerical simulation are: spatial resolution $N = 2^{12}$, time step $dt = T_p/128$ and nonlinearity in wave steepness $M = 4$.

In the following we present the results using approach I. We quantify the predictability in each approach by plotting the prediction accuracy as shown in equations 4.4 versus H_{rs} in the two-layer fluid. Three criteria are used to assess the prediction accuracy. Firstly, if the predicted H_{rs} is within 10% change of the actual one, the prediction is defined accurate. Leonard & Williams [94] showed that 10% change in H_s results in waves with a longer/shorter return period (i.e. order of years). Secondly, although the predicted H_{rs} might be very different from the actual one, the predictions are acceptable if the occurrence of the rogue waves is successfully captured. Thirdly, the prediction of extreme waves with height larger than the design load of offshore structures is of our interest. As recommended by NORSOK[95], H_{10000}, which has an annual exceedance probability of 10^{-4}, is taken as $2.375H_s$ for the conservative design wave height. Thus, the prediction accuracy of rogue waves with $H_{rs} > 2.375$ will be inspected.

The predictability of rogue waves are discussed for different sea states (i.e. 4, 5 and 6), as shown in Figure 4.3 and 4.4. Each marker represents the accuracy of predicted rogue waves using the homogeneous fluid model. The linear interpolation is also calculated to show the statistical properties. It is natural that larger waves develop more easily in a rougher sea state while the largest H_{rs} in a specific sea state is bounded by a limit. This has been shown by Alam[52] in the homogeneous fluid. In the two layer fluid, the maximum H_{rs} ratio is 2.56 in sea state 4, 2.63 in sea state 5 and 2.7 in sea state 6 for the 48 cases analyzed.

First, we consider the effect of density ratio for $\mathcal{R}$=0.99, 0.95 and 0.9. The prediction accuracy decreases dramatically as $\mathcal{R}$ decreases (i.e. the linear interpolation of the accuracy drops as $\mathcal{R}$ decreases in Figure 4.3). For example, for predictions in short time (i.e. $100T_p$) in sea state 4, as shown in Figure 4.3a, the error for typically stratified ocean (i.e. $\mathcal{R}$=0.99) is extremely small (i.e. all the blue markers have error less than 5%). When density ratio decreases to 0.95, the prediction error increases slightly but still within 10%. The predictions becomes worse when the density drops to the unrealistic case (i.e. $\mathcal{R}$=0.9). Similar trend is also observed for sea states 5 and 6 shown in Figures 4.3c and 4.3e.

Now in order to assess the effect of prediction time on the prediction accuracy, we consider a case when the predictions are made for $500T_p$. For long time prediction (i.e. $500T_p$), the prediction accuracy significantly drops compared with short time ($100T_P$) predictions. For the same density ratio, the linear interpolation of the accuracy in $500T_p$ is significantly lower than that in $100T_p$. For example, in sea state 4 for strongly stratified ocean (i.e. $\mathcal{R} = 0.95$), the linear interpolation of prediction accuracy (i.e. red line) decreases notably as the prediction time increases from $100T_p$ to $500T_p$. It can be noticed that the data points are more scattered in Figure 4.3b compared with Figure 4.3a. In addition, the red line in Figure 4.3b has a steeper slope compared with $100T_p$ in Figure 4.3a, which indicates that not only

the prediction error is larger, but also the prediction error is increasing with a larger rate as H_{rs} increases for a longer prediction time. This is also the case for sea state 5 (Figures 4.3c and 4.3d) and sea state 6 (Figures 4.3e and 4.3f).

Then we extend our analysis on the prediction accuracy in various sea states. In sea state 4, the predictions can be made accurately up to $500T_p$ for $\mathcal{R}=0.99$ and 0.95 (i.e. all the blue markers are within 10% error in both Figures 4.3a and 4.3b, and all the red markers are within 10% error in Figure 4.3a and only 6 red markers are outside 10% but still within 20% error in Figure 4.3b). The predictions for $\mathcal{R}=0.9$ is not satisfactory for both $T_p=100$ and 500. In sea state 5, the predictions are accurate up to $500T_p$ for $\mathcal{R}=0.99$ but not 0.95. Only one red marker has error larger than 10% in Figure 4.3c but the red markers are scattered and many of them have error greater than 10% in Figure 4.3d. Similar patterns are observed in sea state 6 as in sea state 5. All the results above suggest the appropriateness of using the homogeneous fluid model to predict the rogue waves height for strongly stratified fluid (i.e. $\mathcal{R}$ as low as 0.95) up to $500T_p$ ahead in sea state 4, and up to $100T_p$ ahead in sea states 5 and 6.

Besides the rogue wave height, correct prediction of the time and space domain that waves occur is of importance. Markers in the gray regions in Figure 4.3 and 4.4 represent the dangerous cases that the predicted waves have $H_{rs} < 2$ (i.e. not predicted not rogue waves) while they are actual rogue waves (i.e. $H_{rs}^{(2)} > 2$). As shown in Figures 4.3a, 4.3c and 4.3e, all of the markers fall outside the gray region for typically stratified ocean (i.e. $\mathcal{R}=0.99$) in $100T_p$. While several markers fall into gray region in $500T_p$, shown in Figure 4.3b, 4.3d and 4.3f. But these markers are localized in the region with low H_{rs} ratio (i.e. $H_{rs} < 2.1$), and thus are less harmful. In the case of strongly stratified ocean (i.e. $\mathcal{R}=0.95$), only 4-5 localized markers (i.e. $H_{rs} < 2.1$) out of 48 initial conditions fall into the gray region for $\mathcal{R}=0.95$ in $100T_p$. However, if the prediction needs to be made in long time (i.e. $500T_p$), the prediction of rogue waves occurrence is not accurate (i.e. many of the red markers fall into the gray regions in Figure 4.3b, 4.3d and 4.3f). In addition, for the unrealistic stratified fluid (i.e. $\mathcal{R}=0.9$), the predictions are not acceptable even for $100T_p$ (i.e. many of the red circles fall into the gray regions in Figure 4.3a, 4.3c and 4.3e). Thus, generally, the homogeneous fluid model can be used in rogue waves prediction up to $100T_p$ ahead for typically and strongly stratified fluid (i.e. $\mathcal{R}$ as low as 0.95).

Besides the occurrence of rogue waves (i.e. $H_{rs} > 2$), it is of great interest to find the rogue waves which exceed the design load of offshore structures. Most of the offshore structures are designed based on design load of waves with 10000 years return period. Markers in the red region in Figures 4.3 and 4.4 represent the predicted waves with height less than $H_{10000} = 2.375H_s$ (i.e. predicted as safe waves for offshore structures) while the actual height of the rogue waves is greater than H_{10000} (i.e. dangerous waves). Thus necessary actions can not be taken to avoid or reduce the damages to offshore structures. The long time (i.e. $500T_p$) predictions are accurate for typically stratified ocean (i.e. $\mathcal{R}=0.99$) in all sea states as all the blue markers are outside the red region in Figure 4.3a-4.3f. For predictions in strongly stratified ocean (i.e. $\mathcal{R}=0.95$) in $100T_p$, only one case falls into the red region in sea

state 4, as shown in Figure 4.3a. While four and two cases fall into the red region in sea state 5 and 6, as shown in Figures 4.3c and 4.3e, respectively. For $\mathcal{R}$=0.95 and $T_s = 500T_p$, two cases fall into the red region in sea state 4 while most of the cases fall into the red region for $H_{rs} > H_{10000}$ in sea states 5 and 6. These results suggest that, with the purpose of predicting waves in oceans where offshore structures might be influenced, the homogeneous fluid model is suitable for rogue wave prediction in strongly stratified ocean ($\mathcal{R}$=0.95) in sea state 4 up to $500T_p$ ahead. However, if the prediction needs to be made in rougher sea states (i.e. 5 and 6), the prediction of rogue waves using the homogeneous fluid model is not satisfactorily accurate even for $100T_p$ ahead. When the fluid reach an unrealistic case (i.e. $\mathcal{R}$=0.9), the predictions are not acceptable even in short time (i.e. $100T_p$) for all the sea states as many of the green markers fall into the red region in Figure 4.3a-4.3f. Under-prediction of rogue waves is perilous as stated above, while over-prediction can also cause the waste of resources (i.e. investment of unnecessary time and money for protecting the offshore structures). On the contrary to the red region, markers in the yellow region represent predicted waves with $H_{rs} > 2.375$ (i.e. waves exceeding the design load) for safe waves with $H_{rs} < 2.375$. From Figure 4.3, only 1 to 2 cases fall into the yellow regions for all sea states and for both short and long time predictions. Thus over-prediction is not a major concern when using the homogeneous fluid model.

Now, we further investigate the model by considering the effect of the thermocline depth on the rogue waves prediction as shown in Figure 4.4. In this analysis, $\mathcal{R}$=0.95 is taken for strongly stratified ocean and the overall depth is fixed at 300 m. h_u is taken 15 m, 45 m and 100 m, which correspond to the non-dimensional parameter $k_p h_u$=0.7749, 2.32 and 5.17 for sea state 4, $k_p h_u$=0.64, 1.92 and 4.26 for sea state 5, $k_p h_u$=0.39, 1.16 and 2.58 for sea state 6. The upper layer depth effect can be concluded through comparing the prediction accuracy in Figure 4.4a-4.4e. For example, for $100T_p$ prediction time in sea sate 4, as in Figure 4.4a, the linear interpolation of the prediction error for h_u/h=0.05 has a larger slope than that for h_u/h=0.15 and 0.34 although all the errors are very small. However, for longer time predictions, the linear interpolation for h_u/h=0.34 has the largest error, as in Figure 4.4b. For $100T_p$ in sea state 5, as in 4.4c, the linear interpolation of the prediction accuracy for h_u/h=0.15 has the largest error. When the predictions are in $500T_p$, prediction accuracy for h_u/h=0.15 is still maximum, as in Figure 4.4d. Similarly, no clear dependence is observed on the thermocline depth in sea state 6, as in Figures 4.4e and 4.4f. Thus we find that the upper layer depth does not have an obvious effect on the prediction of the surface rogue waves for a fixed overall depth, which is likely a result of the assumption that interfacial modes are absent in the initial conditions.

4.3.1.1 Internal modes

The above result is based on the assumption that the initial free surface wave field only have contribution from surface modes. In reality, they may have contribution from surface modes, internal modes or usually both. Note that internal waves should have small wave amplitude on the free surface compared to that from the surface modes. So we randomly
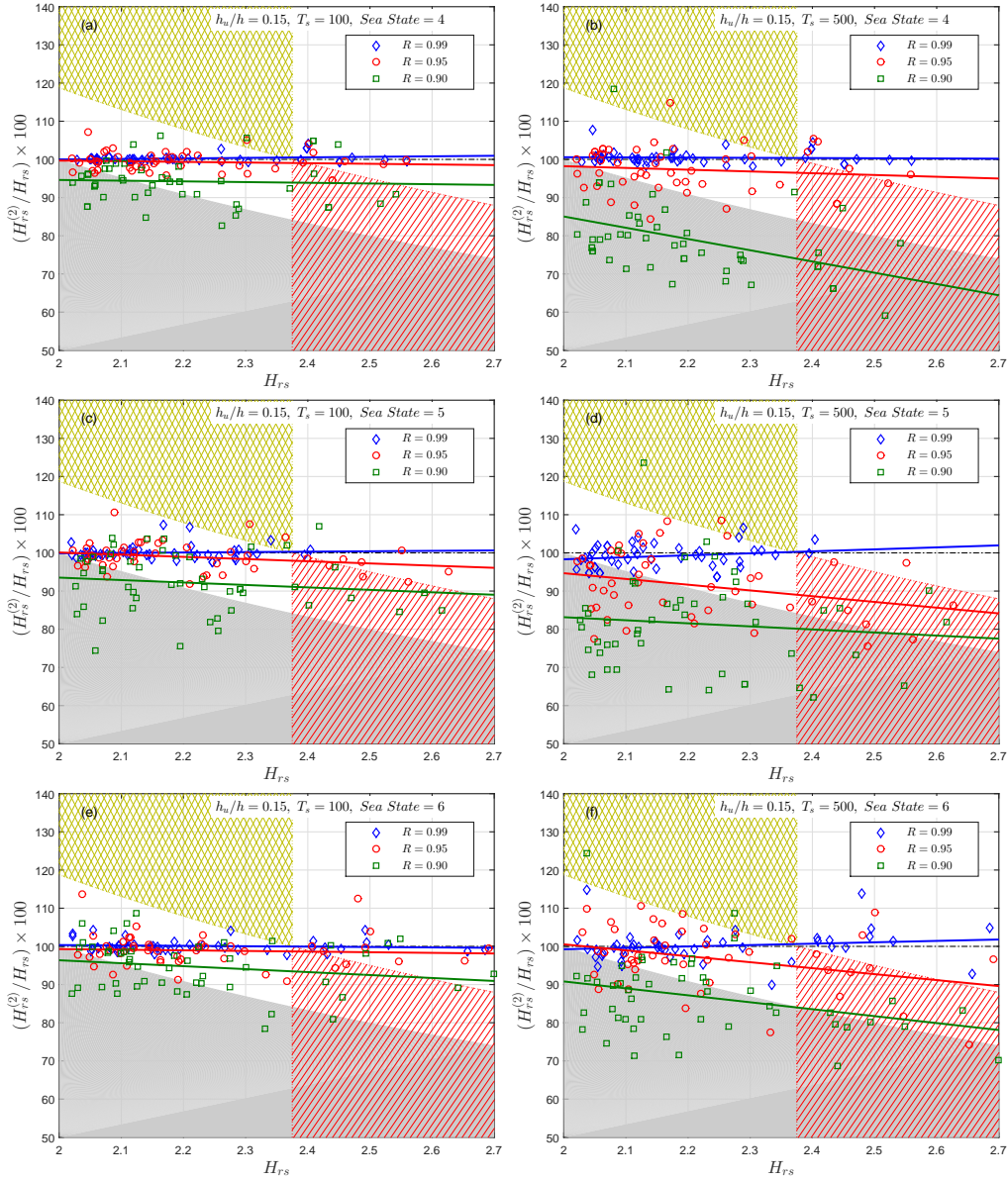
Figure 4.3: Prediction accuracy for density ratio $\mathcal{R}$=0.99, 0.95 and 0.9 using approach 1 in (a) sea state 4 for T_s=100T_p (b) sea state 4 for T_s=500T_p (c) sea state 5 for T_s=100T_p (d) sea state 5 for T_s=500T_p (e) sea state 6 for T_s=100T_p (f) sea state 6 for T_s=500T_p The horizontal axis is $H_{rs} = H_r/H_s$ in the two-layer fluid model. All the markers in the figure represent the result for one distinct initial condition. The blue (red, green) markers represent the prediction accuracy for $\mathcal{R}$=0.99 (0.95, 0.9) and the blue (red, green) solid line is the linear interpolation of the prediction accuracy for $\mathcal{R}$=0.99 (0.95, 0.9).
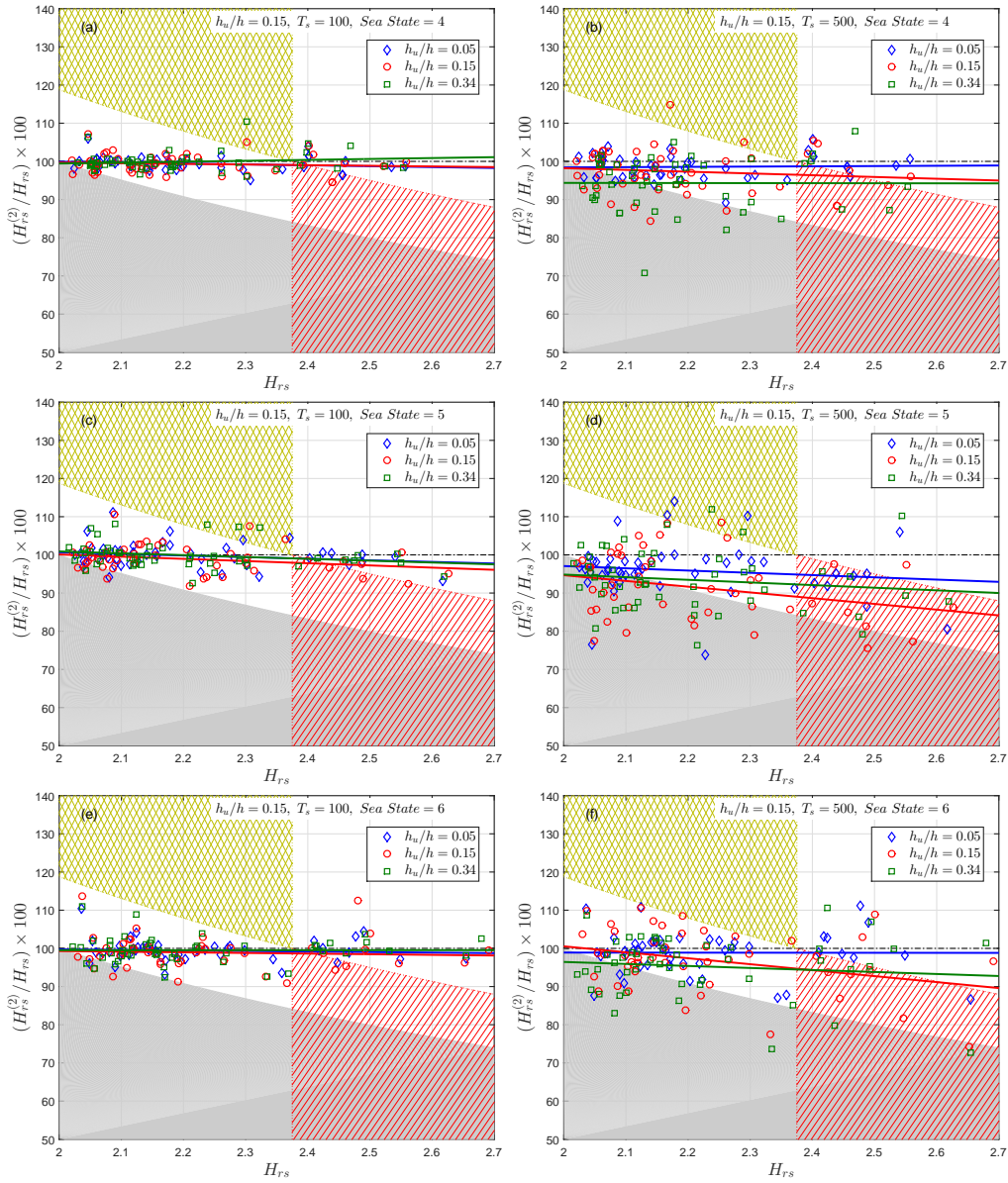
Figure 4.4: Prediction accuracy for h_u/h=0.05, 0.15 and 0.34 using approach 1 in (a) sea state 4 for T_s=100T_p (b) sea state 4 for T_s=500T_p (c) sea state 5 for T_s=100T_p (d) sea state 5 for T_s=500T_p (e) sea state 6 for T_s=100T_p (f) sea state 6 for T_s=500T_p. The horizontal axis is $H_{rs} = H_r/H_s$ in the two-layer fluid. All the markers in the figure represent the result for one distinct initial condition. The blue (red, green) markers represent the prediction accuracy for h_u/h=0.05 (0.15, 0.34). and the blue (red, green) solid line is the linear interpolation of the prediction accuracy for h_u/h=0.05 (0.15, 0.34).
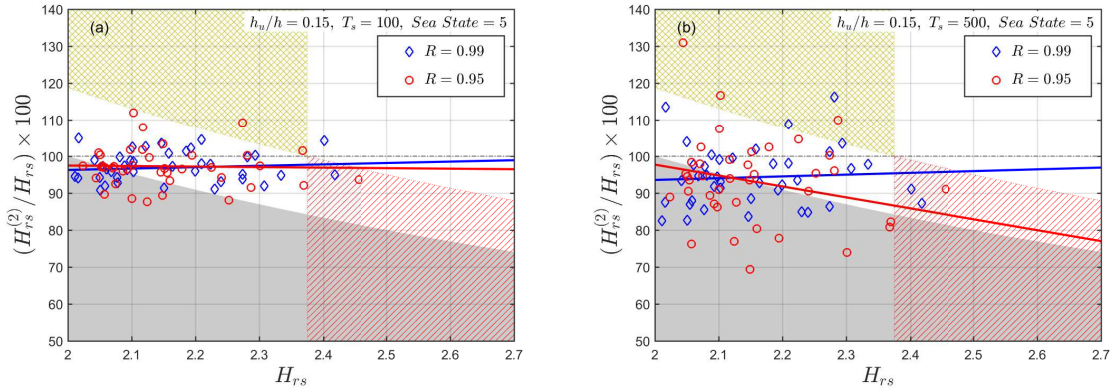
Figure 4.5: Prediction accuracy with internal modes in (a) 100Tp and (b) 500Tp. The cutoff frequency of surface wave is $< \omega_{cutoff} = 0.4025 rad/s$, and the corresponding interfacial wave frequency is 0.0253 and 0.0571 for $\mathcal{R}$ =0.99 and 0.95. With the presence of internal modes in initial conditions, the prediction accuracy significantly drops. Even in short term(i.e. $100T_P$), the error can be more than 10%. Longer term(i.e. $500T_p$) prediction becomes even worse with error more than 30%.

select a portion of some waves with low frequency(i.e. $< \omega_{cutoff}$) to come from internal modes. Assume the stratified ocean can be represented by the two-layer stratified fluid, we quantify the prediction accuracy of using homogeneous fluid model rather than stratified model, as in Figure 4.5. It can be concluded that with the presence of internal modes, rogue wave formation can be significantly affected. Hence we may strongly underestimate the rogue wave height if the homogeneous fluid assumption is made.

4.3.2   Approach II

The second approach is the complement of approach I. The nonlinear initial conditions which lead to rogue waves are obtained from the homogeneous fluid model and then they are employed as the initial conditions on the free surface for predicting rogue waves in the two-layer fluid model. Then the initial conditions on the interface η_{li} and ϕ_{li} are obtained using the linear wave theory if the necessary information on the interface is missing. We assume that initially there is no baroclinic mode in the two-layer fluid model, but baroclinic modes will later develop through nonlinear interactions.

We only use sea state 5 to analyze the prediction accuracy using approach II. First we focus on the effect of the density ratio on the rogue wave prediction, as shown in Figure 4.6, where the h_u/h ratio is 0.15 and h=300 m. Then we analyze the effect of thermocline depth, as shown in Figure 4.7, where $\mathcal{R} = 0.95$. To this end, we use three density ratios $\mathcal{R}$=0.99, 0.95 and 0.9 and two prediction times T_s=$100T_p$ and $500T_p$. As it is shown in Figure 4.6a, the error for $100T_p$ $\mathcal{R}$=0.99 is small ($< 10\%$) for most of the initial conditions, while only for two cases the error is slightly greater than 10%. This is a very interesting and promising result

when we notice that the density stratification in the real ocean is $\mathcal{R} \approx 0.99$, which implies the suitability of this homogeneous fluid model for predicting rogue waves in the real scenario. However, in order to more deeply investigate the stratification effect in the framework of this approach, we further increase the strength of stratification to unreal cases. As the density ratio decreases to 0.95 which is a very highly stratified flow that is very scarce in nature, most rogue waves are still well predicted within 10% error in the two-layer fluid system. For this density ratio, only five cases which have small $H_{rs} < 2.2$ ratios show prediction errors greater than 10%, while the error is still less than 20%. However, for a highly stratified and impossible case with $\mathcal{R}$=0.9, the number of cases with prediction error greater than 10% increases to 9. These results show the possibility of using the homogeneous fluid model for the rogue waves prediction for even highly stratified flow (i.e. $\mathcal{R}$ =0.95) in $100T_p$. The linear interpolation of the data is also plotted to show the statistical trend. They show that the error increases as H_{rs} ratio increases and as the $\mathcal{R}$ deceases (i.e. stronger stratification).

Now in order to assess the effect of prediction time on the prediction accuracy, we consider a case when the predictions are made for $500T_p$. The prediction accuracy for this case is shown in Figure 4.6b. While this figure in the first glance shows scattered data, but careful inspections show that for $\mathcal{R} = 0.99$ only 4 points are predicted with error greater than 10% while they still lie below 20% error. This extends the suitability of the homogeneous fluid model for making long time prediction of rogue waves with promising accuracy when the stratification is real. However, for the very highly stratified case of $\mathcal{R}$=0.95, large prediction errors are observed more (i.e. 16 points have error greater than 10%.) This becomes worse for $\mathcal{R}$=0.90 for which more points lie beyond the 10% error zone compared to the other two stratification ratios. This means that this model could be dangerous for the very strong stratification resulting in erroneous estimations of the wave height prediction.

If the rogue waves occurrence is successfully predicted, even with different H_{rs}, necessary precautions can be taken to avoid or reduce the potential damages. Markers in the gray regions in Figure 4.6 represent the dangerous cases that the predicted waves have $H_{rs} < 2$ (i.e. not predicted as rogue waves) while they are actual rogue waves (i.e. $H_{rs} > 2$). For typically stratified ocean (i.e. $\mathcal{R}$=0.99), the occurrence of the rogue waves are accurately predicted up to $500T_p$ (i.e. only squares with $H_{rs} < 2.1$ fall into the gray region in Figure 4.6b). While for highly stratified fluid with $\mathcal{R}$=0.95, the occurrence of rogue waves are only captured accurately up to $100T_p$ (i.e. almost all of the diamonds are outside the gray region in Figure 4.6a but not in Figure 4.6b). If the density ratio drops to $\mathcal{R} = 0.9$, the prediction of the rogue wave occurrence based on the homogeneous fluid model is not reliable even in $100T_p$ (i.e. many of the circles are in the gray region in Figure 4.6a).

Now, we extend our discussion by studying the effect of the thermocline depth on the rogue waves prediction in approach 2 as shown in Figure 4.7. Three thermocline depths h_u are considered, such that the depth ratios are h_u/h=0.05, 0.15 and 0.34, while the total depth is kept constant at $h = 300$ m. We only use density ratio $\mathcal{R}$=0.95 and consider two prediction times $100T_p$ and $500T_p$ for this case. Interestingly, the comparison of the results for h_u/h=0.05, 0.15 and 0.34 for $100T_p$ as presented in Figure 4.7a shows that the rogue waves are predicted well and there is no meaningful difference in the results for different
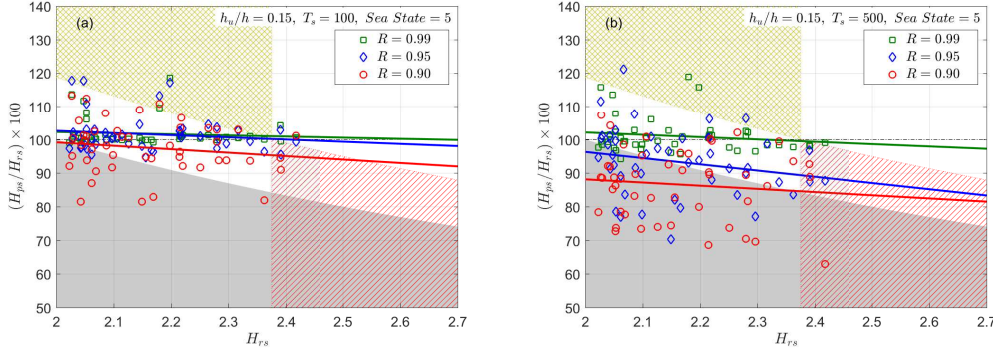
Figure 4.6: Prediction accuracy using approach 2 with respect to H_{rs} ratio in the homogeneous fluid model for density ratio $\mathcal{R}$=0.99, 0.95 and 0.9. (a) is for T_s=100T_p and (b) is for T_s=500T_p The horizontal axis is calculated as $H_{rs} = H_r/H_s$ in the homogeneous fluid model. All the markers in the figure represent the result for one initial condition. The green (blue, red) markers represent the prediction accuracy for $\mathcal{R}$=0.99 (0.95, 0.9) and the green (blue, red) solid line is the linear interpolation of the prediction accuracy for $\mathcal{R}$=0.99 (0.95, 0.9).
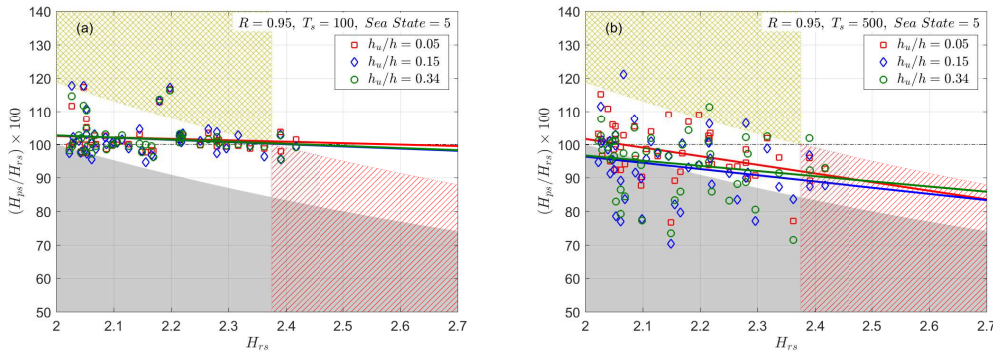
Figure 4.7: Prediction accuracy using approach 2 with respect to H_{rs} ratio in the homogeneous fluid model for h_u/h=0.05, 0.15 and 0.34. (a) is for T_s=100T_p and (b) is for T_s=500T_p. The horizontal axis is calculated as $H_{rs} = H_r/H_s$ in the homogeneous fluid model. All the markers in the figure represent the result for one initial condition. The red (blue, green) markers represent the prediction accuracy for h_u/h=0.05 (0.15, 0.34). and the red (blue, green) solid line is the linear interpolation of the prediction accuracy for h_u/h=0.05 (0.15, 0.34).

depth ratios implying the insensitivity of the model to thermocline depth. This is also shown by plotting the linear interpolations of the prediction accuracy and as it can be seen they closely follow each other. Almost, the same result can be deduced for $500T_P$ shown in figure 4.7b. For this case the results are much more scattered compared to $100T_p$ and no clear correlation between the thermocline depth and the accuracy of prediction can be observed. This is confirmed by drawing the linear interpolation lines for each case which show that the prediction for the shallowest case $h_u/h = 0.05$ is only slightly better compared to deeper cases when $H_{rs} \lesssim 2.45$. Also, the deepest case $h_u/h = 0.34$ results in better prediction compared to $h_u/h = 0.15$ for all H_{rs} values. While this may seem counterintuitive since the effect of the interfacial waves on the surface wave dynamics is expected to be larger for shallower upper layer. However, this invariance is likely a result of the assumption of absence of the interfacial mode initially.

4.4 Summary

In this chapter, we performed extensive computational simulations to quantify the effect of stratification on the prediction of rogue waves in a two-dimensional unidirectional broadband sea. Both short time (i.e. $100T_p$) and long time (i.e. $500T_p$) predictions are considered in different sea states together with varying stratification parameters, including density ratio and thermocline depth. 48 initial conditions in the two-layer fluid model that can lead to rogue waves in the future time are filtered out, and then are applied to the homogeneous fluid model to predict the rogue waves. The highest predicted waves in homogeneous fluid model are compared with the actual rogue waves to quantify the prediction error.

Firstly, by examining the accuracy in predicted height of rogue waves as well as in the occurrence of rogue waves (i.e. check if predicted waves have $H_{rs} > 2$) we find that the homogeneous fluid model is suitable for both short and long times predictions (i.e. $100T_p$ and $500T_p$) for typical density stratification in the ocean (i.e. $\mathcal{R}=0.99$). It is shown that the prediction accuracy drops significantly as the fluid density stratification increases and thus the homogeneous fluid model is no longer applicable for long time predictions (i.e. $500T_p$). This model is still applicable for short time (i.e. $100T_p$) predictions for strongly stratified ocean (i.e. $\mathcal{R}=0.95$) but for unrealistic stratifications (i.e. $\mathcal{R}=0.9$), even the short time (i.e. $100T_p$) predictions are not acceptable. Moreover, remarks are made on the application of the homogeneous fluid model in predicting the dangerous waves exceeding the design load of offshore structures (i.e. to check if the predicted waves have $H_{rs} > 2.375$). We suggest that the homogeneous fluid model is suitable for predictions in typically or strongly stratified ocean (i.e. $\mathcal{R}$ as low as 0.95) up to $500T_p$ in sea state 4. In rougher sea states (i.e. sea states 5 and 6), the predictions for normal stratifications can still be made accurately up to $500T_p$, but the predictions are accurate only up to $100T_p$ for strongly stratified ocean. For unrealistic stratifications (i.e. $\mathcal{R}=0.9$), the predictions are not accurate even for $100T_p$.

In addition, we assessed the thermocline depth and observed that the predicted rogue waves are not sensitive to the thermocline depth change. This may be explained by the

assumption we made that baroclinic modes are absent in the initial conditions. Although this is not always true in a realistic scenario, it seems to be an ideal starting point for introducing the effect of stratification effect due to the lack of realistic information about internal waves in the ocean. Under this assumption, the non-resonant interactions may dominate and hence do not significantly affect the surface wave field evolution[96]. An interesting and immediate follow-up of the current research is to include the baroclinic modes in the initial conditions, which is expected to notably change the predicted rogue waves.

Chapter 5

Prediction of rogue wave occurrence

5.1 Background

Predicting rogue waves is an outstanding challenge in ocean engineering[43] not only because they lead to catastrophic disasters on ships and offshore structures every year, but also because the exact physical mechanism of rogue waves is yet not well understood[10]. Unlike tsunamis or storms, which can be predicted hours in advance[97], the inherent complexity of oceanic waves interactions makes prediction of rogue waves appear far-reaching and motivates statements such as these waves "appear from nowhere"[7]. Predictions of rogue waves, even a short time in advance, can significantly increase the safety of operations in the ocean.

One major question in rogue waves study is to predict whether rogue waves will occur or not, and if yes then when and where they will occur. Recent advancements in radar technology can now provide a high-resolution spatial and temporal distribution of wave. This, together with the calibrated in situ or remotely sensed data, enable us to predict wave evolutions in the near future[98, 99]. Rogue waves are possible to be predicted using direct wave simulations, but such predictions are relatively sensitive to the measurement errors[52] as well as the stratification in ocean[100]. Moreover, the direct simulations can be very expensive. Many rogue wave prediction models are based on numerical predictions in the framework of weakly nonlinear governing equations(i.e. Nonlinear Schrödinger Equation(NLS) or Modified Nonlinear Schrödinger Equation(MNLS)). The particular triangular shape of wave spectra is detected at early stage of the rogue wave development[101], and hence continuously detection of the wave spectra can possibly help detect the dangerous peak before it occurs. It is also shown that minimizing the variance of the total wave phase can be used as an indication of the location and time of rogue wave occurrence [74]. Still within the framework of MNLS, the modulation instability analysis on localized wave groups allows the detection of such instabilities at the early stage and hence serves as precursors for rogue waves[42]. Quantitative assessment on this precursor has been evaluated and this precursor achieves relatively high successful prediction rate with low false prediction rate. However, these methods proposed above are limited only to NLS or MNLS systems, which

does not consider wave dissipation in long term evolution($t/T_p \geq \mathcal{O}(\epsilon^{-2})$)[1] and hence does not represent the strongly non-Gaussian statistics of wave events in long term. The main goal of our work is to identify and develop a robust precursor for rogue wave occurrence in the high-order nonlinear system(i.e. Zakharov Equation).

A number of mechanisms have been proposed to explain the unexpectedness of rogue waves[102], at the mean time there is an increasing consensus that energy focusing as a result of energy exchange between different wave modes plays an important role in the rogue wave formation[103, 104]. The superposition of sinusoidal waves with different modes is the simplest mechanism that explains the occurrence of rogue waves in small amplitude background environment. In weakly nonlinear systems, such as NLS system, the Davey-Stewartson system, the Kortewegde Vries equation and the Kadomtsev-Petviashvili equation, modulational instability(i.e. Benjamin-Feir instability) is suggested as one mechanism of rogue wave formation[105] in deep water. In shallow waters, wave focusing is suggested as the main mechanism of rogue wave formation[106]. Other mechanisms, like the wave-current interaction and wind-driven waves, can also trigger the extreme events. In reality, the extreme events(e.g. rogue waves) are mostly likely a result of several combined mechanisms. Thus we propose to directly look at the energy focusing and scattering of surface waves without worrying about the exact mechanism behind them. Staring with 2-dimensional wave propagation problem in deep water with flat seabed, we derived a precursor based on energy flux over a vertical plane from seabed to free surface to predict rogue wave events in future time. In this way, the precursor we proposed can be easily extended to a broader application(e.g. 3-dimensional rogue waves, current induced rogue waves).

By simply tracking how energy focuses in both space and time, we can define a criterion on energy flux focusing that serves as a robust precursor for rogue wave occurrence. We focus on 2D non-breaking sea states because predictions on rogue wave probability based on 2D models represent an upper limit of what can happen in more realistic ocean wave conditions[50]. We further test this precursor using statistical approach in a larger numerically generated database. Moreover, the prediction based on energy flux is very cost effective since it does not require the simulation of the whole time window $[0, T]$ if we need to predict whether rogue waves will occur up to $t = T$. We reached a relatively high prediction accuracy(i.e. more than 80%) in terms of rogue wave occurrence with a relatively low false prediction rate(i.e. ~20%). Predictions can be usually $\mathcal{O}(10)T_p$ ahead of rogue wave occurrence, which is about several minutes ahead.

5.2   Governing equations

The surface water wave dynamics, under the assumption of inviscid, irrotational, incompressible and homogeneous fluid, can be described by the potential flow theory. Here we solve the two-dimensional weakly nonlinear wave evolution equations in the Zakharov form[31] (see equation (5.1)), which can be solved through a phase resolved high-order spectral (HOS) method. This method has been used widely in solving many problems, such as wave bottom

and wave-wave interactions[47, 40, 38, 107, 41]. It has also been extended to the scenario of rogue waves [34, 108, 109]. Note that the governing equations are constructed in the Cartesian coordinate system located at the mean free surface with x as the horizontal 0 and z as the vertical axis. The free surface elevation is denoted as η. The field velocity $\mathbf{u}(x, z, t)$ is expressed in terms of the velocity potential $\phi(x, z, t)$ with the relation $\nabla \phi = \mathbf{u}$. In terms of the velocity potential evaluated at the free surface $\phi^s(x, t) = \phi(x, z = \eta, t)$, the governing equations read

$$\eta_t = \phi_z^S(1 + \eta_x^2) - \phi_x^S \eta_x \qquad \text{at } z = \eta(x, t) \qquad (5.1a)$$

$$\phi_t^S = -g\eta - 1/2(\phi_x^S)^2 - 1/2\phi_z^2(1 + \eta_x^2) \qquad \text{at } z = \eta(x, t) \qquad (5.1b)$$

As a primary consideration, we do not consider any effects from seabed topography, and hence the bottom boundary condition is $\phi_z = 0$ at the uniform water depth $z = -h$. The effect of bottom topography can be easily taken into account by simply modifying the bottom boundary condition.

In reality, the surface elevation η is initialized with the reconstructed wave field from the SAR images or ship-borne photographs[110]. To test the accuracy of our precursor, we numerically generate a database of waves from initial wave field characterized by the JONSWAP spectrum. The JONSWAP spectrum is defined by the sea state parameters, which is a general description of the sea roughness. For a given sea state, the JONSWAP spectrum can be calculated as in Equation (2.15) in chapter 2:

$$S(\omega) = \frac{\alpha_p g^2}{\omega^5} \exp(\beta) \gamma^\delta \qquad (5.2)$$

The power spectrum can be expressed in terms of wavenumber by using the relation $S(k) = S(\omega)C_g$, where C_g is the group velocity. The wave amplitude can be calculated as $a(k) = \sqrt{2S(k)dk}$. The initial random sea states characterized by the spectral density $S(\omega)$ can thus be generated by assigning a uniformly distributed random phase $\theta \in (0, 2\pi)$ to each wave in the domain. Here we adopt the conventional definition of rogue wave in terms of wave height $H_r > 2H_s$, where H_r is the maximum height of rogue waves and $H_s = 4\sigma$ (σ is the standard deviation of the surface wave elevation) is the significant wave height. In this chapter, sea states 4 is considered, which represents the mild sea state. It has significant wave height $H_s = 1.875$ meter, and the peak period $T_p = 8.8$ second.

5.2.1 Energy flux

In a particular sea state, we are interested in how energy focus and scatters in space and time, that can serve as a precursor of rogue wave event in the future time. Starting from a general problem in the whole fluid domain bound by control volume V, the total energy in this control volume reads

$$E(t) = \rho \iiint_\Omega (1/2|\mathbf{v}|^2 + gz)dV \qquad (5.3)$$

Thus the energy flux across a control surface S bounding the control volume V reads

$$
\begin{aligned}
p(t) &= \frac{dE}{dt} \\
&= \frac{d}{dt}\rho \iiint_\Omega (1/2|\mathbf{v}|^2 + gz)dV \\
&= \iiint_\Omega \frac{\partial \mathcal{E}}{\partial t}dV + \iint_S \mathcal{E}U_n dS
\end{aligned}
\tag{5.4}
$$

Where $\mathcal{E} = \rho(1/2|\mathbf{v}|^2 + gz)$. In particularly, the control surface S for 2D wave evolution problem is chosen as a vertical plane from flat seabed to free surface. Hence after some mathematical manipulations, energy flux can be written as

$$
p(t) = -\rho \int_{-h}^{\eta} \frac{\partial \phi}{\partial t}\phi_x dz
\tag{5.5}
$$

The complete derivation to Equation (5.5) is covered in Appendix B.

Energy flux varies with time and space, and is calculated numerically together with the wave elevation using the HOS method. ϕ_t is obtained using the backward one-step finite different method. And the integration part is also calculated numerically. The result of energy flux has been tested to converge with nonlinear modes M, current spatial and time resolution. A good match has been reached between the energy flux using numerical method with $M = 1$ and the theoretical energy flux from linear theory.

To eliminate unstructured pattern, we average the energy flux over the spatial window $[-a\lambda_p, +a\lambda_p]$ to get processed energy flux $\bar{P}$. a is chosen to be 1 such that both unwanted oscillations are avoided and basic patterns of energy flux are preserved. Furthermore, we subtract the mean energy flux P_{ave} from the energy flux $\bar{P}$ and reach processed energy flux $\hat{P}$. Energy flux P stays positive for unidirectional (i.e. left to right propagating) 2D wave. Meanwhile, the mean value of energy flux in the whole fluid domain remains almost constant in time. Hence the processed energy flux $\hat{P}$ has positive and negative values, as in Figure 5.1. Positive $\hat{P}$ indicates energy travels faster than the average level, while negative $\hat{P}$ indicates slower than average level. If we observe a large positive energy flux crest on the left of a negative energy flux trough, energy is likely to accumulate between the crest and trough which obviously is inclined to trigger rogue wave events.

The central problem is whether this pattern of energy flux can be used as a precursor of extreme event and how much in advance can we predict an extreme event. We define a simple parameter H_e, which is the maximum height of highest crest to the tough on its right of the processed energy flux $\hat{P}$(see Figure 5.1). The detailed precursor based on this parameter will be presented in next section.
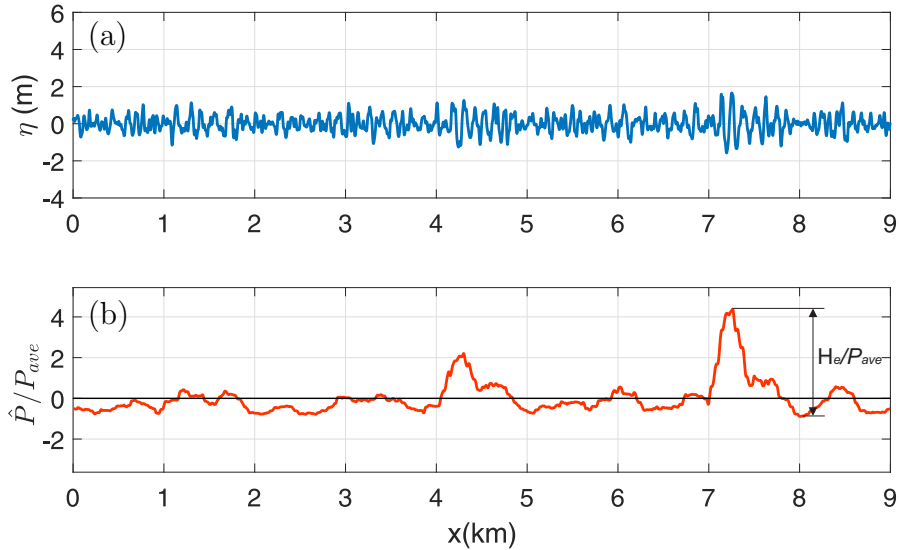
Figure 5.1: Surface wave elevation (a) and the corresponding processed energy flux over the mean energy flux (b). The energy flux is averaged over the spatial window $[-\lambda_p, +\lambda_p]$ and the mean energy flux is subtracted from the averaged energy flux. The maximum height of normalized energy flux is shown as H_e in (b), which is used to define the metric in rogue wave prediction later. The location with large H_e indicates wave groups here are most likely to develop into rogue waves. Other locations with energy focusing(i.e. smaller crests and troughs of energy flux) may also result in rogue waves.

5.3   Predictions of extreme events

For a given sea state, we may determine how much net energy flux is needed to "trigger" an extreme event in the future. We present our main results in this section where a straightforward scheme to predict extreme events in advance is developed and tested. The prediction based on energy flux has very low computational cost since we only need to run the simulation for one time step given the current sea surface. There is no need to run the simulation for the whole time domain $t = T_f$ if we want to know whether rogue waves will be expected in the time window $t = [0, T_f]$.

For each given sea state, we first run many simulations and screened out those result in rogue waves in future time. Then we conduct analysis on these cases and summarize a criterion on rogue wave prediction. Furthermore, the robustness of the criterion is tested on many other random cases and other sea states. In sea state 4, we concluded that $H_e/P_{ave} > 3.5$ gives good accuracy of rogue wave prediction as well as relatively low false prediction rate(i.e. rogue waves are predicted but not occurred in reality). One case of rogue wave formation and the corresponding energy flux as prediction mechanism is shown in Fig. 5.2. The rogue wave occurs at $t = 66.6T_p$ and reaches maximum wave height at $t = 68T_p$. We

observe energy focuses at the location of rogue wave occurrence. In fact, energy focuses before the rogue wave occurs(i.e. usually $\mathcal{O}(10)$ peak periods). As observed in Fig. 5.2(b), energy focuses and H_e/P_{ave} reaches 3.5 several peak periods ahead of the rogue wave occurrence. This indicates that rogue wave will occur in the future time for this particular case.

To test the accuracy using energy flux as the precursor of rogue wave event, we form a database of $\mathcal{O}(100)$ wave evolution with random initial conditions, where the cases used to develop this criterion are not included For each case, we search for rogue waves in time window $[50T_p,130T_p]$. In total N cases, rogue wave occurs in r cases, and we successfully predict s of them. This result in successful rate of s/r. On the other hand, we falsely predict f waves as rogue waves which are indeed not. This result in false rate of f/(N-r).

We further analyze how the successful and false rate vary with the constant β in the criterion $H_e/P_{ave} \geq \beta$, see Fig.5.3. Within the same database of 160 random realizations in sea state 4, we change the constant β and find out how many rogue waves are successfully predicted and how many normal waves are falsely predicted as rogue waves. Both the successful and false rate decease as β increase. But the false rate decreases at a larger rate. For sea state 4, $\beta = 3.5$ gives a relatively good prediction of rogue waves (i.e. we successfully predict 52 out of 64 rogue waves) and low false prediction rate(i.e. among 94 cases with no rogue wave occurrence, we falsely predict 21 of them). Hence we have successful prediction rate s/r=81.25% and false prediction rate f/(N-r)=21.88%. On average, we can predict the occurrence of rogue wave event $32T_p$ ahead of time. This is about 4 minutes and 40 seconds ahead.

5.4   Energy concentration through wavelet analysis

Wavelet transform has localized information not only in space, but also in scale, which renders them suitable for the study of measured data of non-stationary, transient phenomenon in dispersive medium, such as rogue waves. In the past decades, wavelet analysis has been successfully applied to ocean engineering fields[111, 112, 113]. Wavelet transform represents the space series in terms of a combination of many localized functions of different scale, named wavelet function. Wavelet transform is similar to the Fourier transform in the sense of decomposing signal into a summation of series. Thee inherent difference is that Fourier transform uses basis function of sines and cosines, while wavelet transform uses basis function that is localized in both space and scale. Here, we used continuous wavelet transform on rogue wave series, which can be expressed by the following equation:

$$W_i(s) = \sum_{j=0}^{N-1} f_j \phi(\frac{x_j - x_i}{s}) \tag{5.6}$$

$\phi_i(\eta)$ is wavelet functions, where we use Morlet wavelet, consisting of a plane wave modulated by a Gaussian:
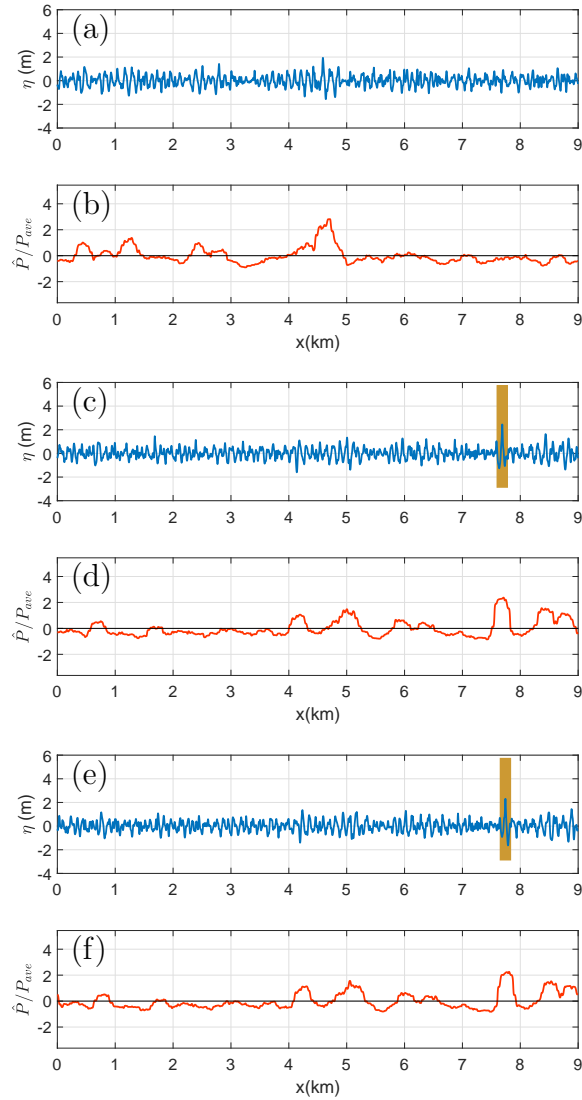
Figure 5.2: Surface wave elevation and the corresponding normalized processed energy flux $\hat{P}/P_{ave}$ at $t = 7T_p$(see (a) and (b)), $t = 66.6T_p$(see (c) and (d)) and $t = 68T_p$(see (e) and (f)). The maximum normalized wave height is defined as $H_{ms} = H_m/H_s$, where H_m is the maximum wave height. Rogue wave occurs at $t = 66.6T_p$ with $H_{ms} = 2.001$(see the orange rectranguler in(c)). After evolving for $1.4T_p$ the rogue waves reaches maximum height $H_{ms} = 2.124$ at $t = 68T_p$(see the orange rectranguler in (e)). Rogue wave occurs as a result of energy focusing(i.e. a large hump of energy flux at the location of rogue wave occurrence) as in (d) and (e). This energy focusing has been observed about $60T_p$ before the rogue wave occurs, as in (b). At $t = 7T_p$, the normalized maximum processed energy flux is $H_e/P_{ave} = 3.503$, which satisfy the criterion predicting rogue waves. This is consistent with what has been observed in (c) and (e).
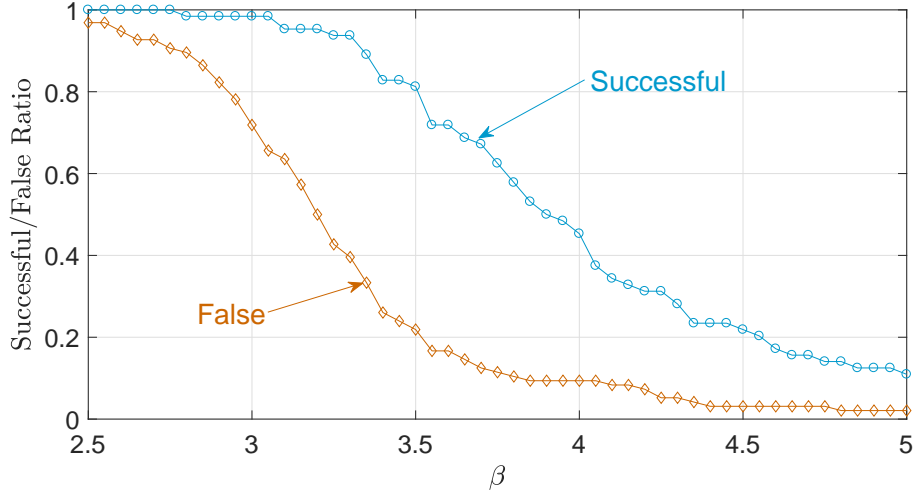
Figure 5.3: Successful(blue line) and false(orange line) prediction ratio for sea state 4. As the criterion becomes more "strict", or as β increases in the criterion $H_e/P_{ave} \geq \beta$, both the successful and false rate decrease. The total number of random cases is N=160.

$$\phi(\eta) = \pi^{-1/4} \exp(i\omega_0\eta) \exp(-\eta^2/2) \tag{5.7}$$

We use Morlet wavelet, which allows high scale resolution as such a wavelet is very well localized in length scales. ω_0 is the non-dimensional frequency. By translating along localized space index i and the wavelet scale s, we construct a picture showing both the amplitude of any features versus the scale and how this amplitude varies in space. The detailed introduction on wavelet transform on spatial series of ocean wave series is covered in Appendix C.

Because the wavelet function $\phi(\eta)$ is generally complex, the wavelet transform $W_i(s)$ is complex as well. So we have real and imaginary parts of $W_i(s)$. A larger positive amplitude in wavelet coefficients implies a higher positive correlation, while a large negative amplitude implies a high negative correlation. So the wavelet power spectrum(WPS) is defined to determine the distribution of energy within the data array, which is $|W(s)|^2$. By identifying large energy concentration in WPS, one can determine which features of the signal are important.

Here we showed one rogue wave event and how does the wavelet power spectrum distribute in both space and length scale, as in Figure 5.4. The results show that rogue waves can be potentially be well predicted from wavelet power spectrum. We observed a high energy density associated with a wave group $\mathcal{O}(10T_p)$ before the rogue wave occurs. This energy is more dense associated with a certain scale factor, in this case $0.9\lambda_p$. We observed this high
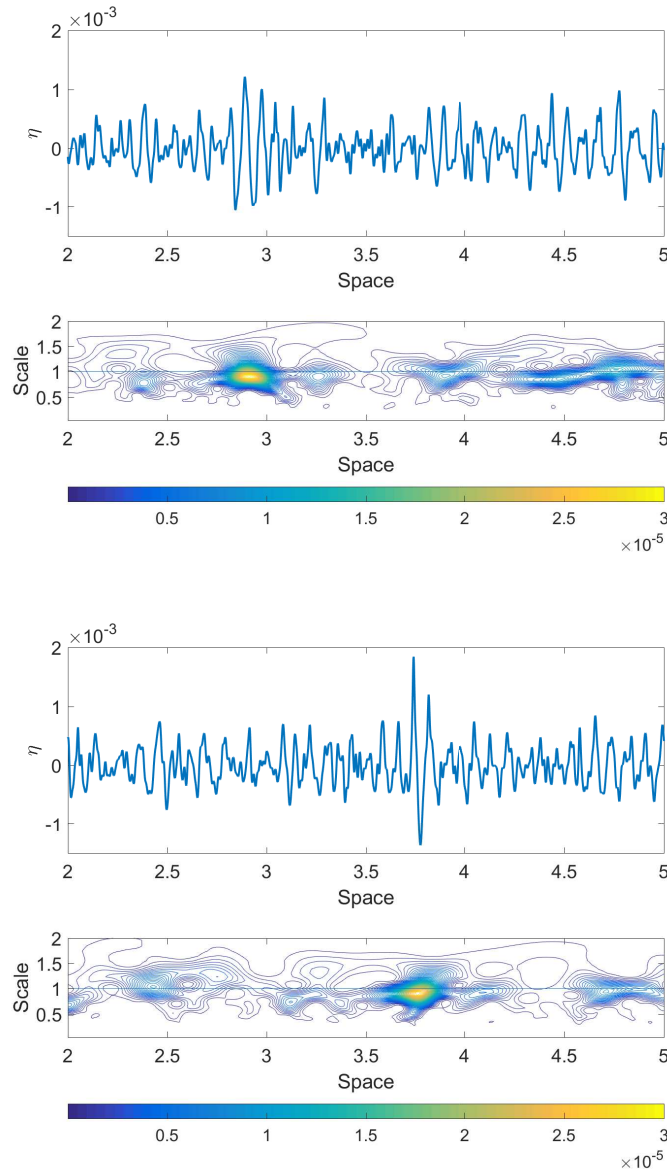
Figure 5.4: An example of a rogue wave occurrence(in (c)) and the wavefield $20T_p$ before that(in (a)). In addition, the corresponding wavelet power spectrum is showed in (b) and (d). This rogue wave has normalized wave height $H_r/H_s = 2.48$. We observe that energy concentrates at the location of the rogue wave, with highest scale close to $0.9\lambda_p$. Looking at the wave field $20T_p$ before the rogue wave occurs, we observed that the highest wave has normalized height $H/H_s = 1.75$. From the surface elevation, it is hard to tell whether a rogue wave will occur or not. However, energy is also concentrated with a certain wave group and this group later evolves into a rogue wave.

energy density pattern for most of the rogue waves in our data set. More detailed analysis is needed for quantitative results to be presented. But wavelet analysis can potentially be the ideal tool for such study.

5.5   Summary

We study and derive a robust precursor in predicting extreme events(i.e. rogue waves) in highly nonlinear waves. We track the time and locations that energy focuses and find that energy focuses several peak periods before the rogue wave occurrence and can exceed a certain level. Based on this observation, we developed the criterion on the maximum net energy flux that can potentially "trigger" rogue wave events. We concluded that $H_e/P_{ave} = 3.5$ is a robust precursor in sea state 4. We managed to achieve a high successful rate in rogue wave prediction($>80\%$) with a relatively low false prediction rate($\sim 20\%$). The constant β in the criterion $H_e/P_{ave} = \beta$ that gives optimal prediction may vary slightly for different sea states, but within same order. The performance of this precursor converges with a larger number of random cases considered.

Although the current set up is limited to unidirectional waves with uniform depth, there is no limitation to apply the criterion $H_e/P_{ave} = \beta$ to other set-ups that involves disturbances such as wind and current, or even 3D wave evolution. This proposed approach introduces a new understanding in predicting rogue waves in nonlinear system. Unlike previous approaches that focus on specific forms of equations and use analytic tools, we derived the precursor by directly tracking the net energy transfer based on statistical approach on a large database. This approach is inexpensive in terms of the time and storage cost.

Since the exact mechanism of rogue wave formation is understandably diverse, this precursor on energy concentration needs to be tested carefully on many other scenarios. It will night be surprising of different freak waves can be predicted the best using different technique.

In the future, we would like to expand this precursor on the rogue wave prediction to problems with bottom corrugations, current, wind and more sea states. We plan to conclude with a robust, consistent scheme for rogue wave prediction in fully nonlinear waves, which can benefit on guiding the offshore installation or operation activities.

Chapter 6

Conclusions and recommendations

6.1   Conclusions

In this dissertation, we first formulated the mathematical model in the application of rogue waves in homogeneous fluid with small seabed corrugations. We derived the governing equations in expansion of ϵ and solved the mathematical model using HOS method.

Statistical properties(i.e. averaged shape, asymmetry, standard deviations) were obtained in various sea states, considering both linear and nonlinear mechanisms. A new approach was proposed to retrieve the averaged profile of rogue waves, through which the asymmetry in the preceding and succeeding troughs is well preserved. The averaged spatial profile is observed having high asymmetry compared with temporal profile, where the deeper trough can be more than twice in height compared to the shallower trough. Thus using the traditional approach I in chapter 3 can strongly underestimate the rogue wave height(i.e. by more than 10% for sea state 4, 5 and 6). Nonlinear effect was quantitatively evaluated and a great impact from second-order nonlinearity on rogue wave formation has been observed. Higher-order nonlieanrities beyond second order play an important, though not dominant, role in forming rogue waves. Other effects(i.e. sea state roughness, water depth) are found less important. Rogue waves show an identical shape in crossing seas in 2-dimensional framework, but the probability of occurrence is much higher compared with that in unidirectional seas.

In chapter 4, we showed that oceanic stratification alters rogue wave dynamics in relatively long term, but not short term. A two-layer stratified fluid model is adopted and the mathematical model is formulated in representing surface wave dynamics in stratified fluid. For the typical density stratification scenario(i.e. two-layer model with density ratio 0.99), rogue wave height is not significantly altered in time up to $500T_p$. The prediction accuracy on rogue wave height significantly drops as the fluid becomes more stratified. For extremely strongly stratified ocean(i.e. density ratio 0.95), rogue wave height can only be relatively well captured up to $100T_p$ if the homogeneous fluid assumption is made. Furthermore, the effect of thermocline depth is found playing a less important role in predicting rogue wave height. However, rogue wave dynamics can be modified significantly in the presence of inter-

nal modes on the thermocline. The prediction of rogue wave height even is not acceptable even in short-term(i.e. $100T_p$) for typical stratified ocean.

In chapter 5, we addressed the problem of predicting rogue wave occurrence in homogeneous ocean by tracking energy accumulation in space. A precursor based on the net height of energy flux(i.e. quantifying energy concentration in space) was proposed to predict whether rogue wave will occur or not in short term(i.e. $\sim 100T_p$). This precursor was tested in a numerical wave dataset. We successfully predicted more than 80% of the rogue waves with a relatively low false predicting rate(i.e. $\sim 20\%$). This precursor was motivated by the observation of high correlation between high energy concentration with large rogue wave height. Further investigation on energy concentration using wavelet analysis was discussed in Appendix C.

6.2   Recommendations on future work

Several extensions of the results presented in this dissertation may be worth further investigations because they could be of significant interest for oceanographers as well as engineering practice. Here, we briefly discuss some of them below.

1. Rogue wave morphology for wave field with high characteristic wave steepness. The averaged morphology of rogue wave in sea state 4, 5 and 6 are considered in this dissertation, where all wave fields considered here all have steepness < 0.1. Although identical averaged profile has been observed as in in figure 3.5, the averaged rogue wave profile can be deviated from that if very steep wave field is considered(i.e. $\epsilon > 0.15$). In order to consider such extremely rough wave field, energy in high frequency need to be dissipated at each time step to avoid numerical explosion.

2. Effect of topography on shallow water rogue waves. Bragg resonance exist for surface waves over a wavy bottom, which can cause energy shifting to other frequencies. This resonant effect on the rogue wave formation is worth looking at. In addition, it has been observed that strong depth variation can potentially trigger rogue wave[19]. So the statistical analysis and quantitative prediction on rogue waves over such bottom corrugations can be interesting.

3. Extend current work from 2D to 3D framework. A full 2D+1 numerical computation of the primitive equation of motion, including a realistic forcing and (some parametrization of) dissipation, is surely needed in order to establish more realistic modeling on the probability of formation of extreme waves in different sea state conditions.[50]. In 3D framework, the temporal rogue wave profile should still be similar to figure 3.4. The spatial profile needs to be carefully defined and may be different from figure 3.2.

Bibliography

[1] W. Xiao, Y. Liu, G. Wu, and D. K. P. Yue, "Rogue wave occurrence and dynamics by direct simulations of nonlinear wave-field evolution," *Journal of Fluid Mechanics*, vol. 720, pp. 357–392, feb 2013.

[2] P. Petrova, Z. Cherneva, and C. Guedes Soares, "Distribution of crest heights in sea states with abnormal waves," *Applied Ocean Research*, vol. 28, no. 4, pp. 235–245, 2006.

[3] P. H. Taylor and T. Adcock, "Draupner Giant Wave of 1St January 1995 and the Associated Sea-State, and How To Estimate Directional Spreading From an Eulerian Surface Elevation Time History," University of Oxford, United Kingom, Tech. Rep., 2006.

[4] I. I. Didenkulova, A. V. Slunyaev, E. N. Pelinovsky, and C. Kharif, "Freak waves in 2005," *Natural Hazards and Earth System Science*, vol. 6, no. 6, pp. 1007–1015, 2005.

[5] L. Cavaleri, L. Bertotti, L. Torrisi, E. Bitner-Gregersen, M. Serio, and M. Onorato, "Rogue waves in crossing seas: The Louis Majesty accident," *Journal of Geophysical Research: Oceans*, vol. 117, no. 5, pp. 1–8, 2012.

[6] I. Viste-ollestad, T. L. Andersen, and I. Viste-ollestad, "Granskingsrapport etter hendelse med fatalt utfall på COSLInnovator 30. desember 2015," Narve Oma og Sigvart Zachariassen, Tech. Rep., 2015.

[7] C. Kharif, P. Efim, S. Alexey, K. C., E. Pelinovsky, and A. Slunyaev, *Rogue Waves in the Ocean.* Elservier Scientific Publishing Company, 2014, no. 1.

[8] H. Socquet-Juglard, K. B. Dysthe, K. Trulsen, H. E. Krogstad, and J. Liu, "Probability distributions of surface gravity waves during spectral changes," *Journal of Fluid Mechanics*, vol. 542, pp. 195–216, 2005.

[9] M. Christou and K. Ewans, "Field Measurements of Rogue Water Waves," *Journal of Physical Oceanography*, vol. 44, no. 9, pp. 2317–2335, 2014.

[10] C. Kharif and E. Pelinovsky, "Physical mechanisms of the rogue wave phenomenon," *European Journal of Mechanics - B/Fluids*, vol. 22, no. 6, pp. 603–634, nov 2003.

[11] C. Guedes Soares, Z. Cherneva, and E. M. Antao, "Steepness and asymmetry of the largest waves in storm sea states," *Ocean Engineering*, vol. 31, no. 8-9, pp. 1147–1167, 2004.

[12] A. K. Magnusson and M. A. Donelan, "The Andrea Wave - Characteristics of a Measured North Sea Rogue Wave," *Proceedings of 27th International Conference on Offshore Mechanics and Arctic Engineering*, vol. 135, no. 1999, pp. 1–10, 2012.

[13] K. B. Dysthe, H. E. Krogstad, and P. Müller, "Oceanic Rogue Waves," *Annual Review of Fluid Mechanics*, vol. 40, no. 1, pp. 287–310, 2008.

[14] G. Wu, "Direct simulation and deterministic prediction of large-scale nonlinear ocean wave-field," Ph.D. dissertation, Massachusetts Institute of Technology, Cambridge, MA, 2004.

[15] A. Toffoli, T. Waseda, H. Houtani, L. Cavaleri, D. Greaves, and M. Onorato, "Rogue waves in opposing currents: an experimental study on deterministic and stochastic wave trains," *J. Fluid Mech*, vol. 769, no. 2015, pp. 277–297, 2016.

[16] M. Christou, K. Ewans, B. Buchner, and C. Swan, "Spectral characteristics of an extreme crest measured in a laboratory basin," in *Proc. Rogue Waves*, Brest, France, 2008, pp. 165–178.

[17] T. E. Baldock and C. Swan, "Extreme waves in shallow and intermediate water depths," *Coastal Engineering*, vol. 27, no. 95, pp. 21–46, 1996.

[18] K. Trulsen, H. Zeng, and O. Gramstad, "Laboratory evidence of freak waves provoked by non-uniform bathymetry," *Physics of Fluids*, vol. 24, no. 1070, pp. 1–11, 2012.

[19] C. Viotti and F. Dias, "Extreme waves induced by strong depth transitions : Fully nonlinear results Extreme waves induced by strong depth transitions : Fully nonlinear results," *Physics of Fluids*, vol. 26, 2014.

[20] J. Touboul and C. Kharif, "On the interaction of wind and extreme gravity waves due to modulational instability," *Physics of Fluids*, vol. 18, no. 10, 2006.

[21] A. Toffoli, D. Proment, H. Salman, J. Monbaliu, F. Frascoli, M. Dafilis, E. Stramignoni, R. Forza, M. Manfrin, and M. Onorato, "Wind Generated Rogue Waves in an Annular Wave Flume," *Physical Review Letters*, vol. 118, no. 14, pp. 1–5, 2017.

[22] N. N. Akhmediev, V. M. Eleonskii, and N. E. Kulagin, "Exact first-order solutions of the nonlinear Schrodinger equation," *Theoretical and Mathematical Physics*, vol. 72, no. 2, pp. 809–818, 1987.

[23] M. J. Ablowitz and B. M. Herbst, "On Homoclinic Structure and Numerically Induced Chaos for the Nonlinear Schrödinger Equation," *SIAM Journal on Applied Mathematics*, vol. 50, no. 2, pp. 339–351, 1990.

[24] N. Akhmediev, A. Ankiewicz, and M. Taki, "Waves that appear from nowhere and disappear without a trace," *Physics Letters A*, vol. 373, no. 6, pp. 675–678, feb 2009.

[25] P. Dubard and V. B. Matveev, "Multi-rogue waves solutions: from the NLS to the KP-I equation," *Nonlinearity*, vol. 26, no. 12, p. R93, 2013.

[26] K. B. K. Dysthe, "Note on a modification to the nonlinear Schrodinger equation for application to deep water waves," *Proceedings of the Royal Society of London. A. Mathematical and Physical Sciences*, vol. 369, no. 1736, pp. 105–114, 1979.

[27] Y. Ohta and J. Yang, "Dynamics of rogue waves in the DaveyStewartson II equation," *Journal of Physics A: Mathematical and Theoretical*, vol. 46, no. 10, p. 105202, 2013.

[28] R. Grimshaw, E. Pelinovsky, T. Talipova, M. Ruderman, and R. Erdélyi, "Short-lived large-amplitude pulses in the nonlinear long-wave model described by the modified Korteweg-de vries equation," *Studies in Applied Mathematics*, vol. 114, no. 2, pp. 189–210, 2005.

[29] P. Dubard, P. Gaillard, C. Klein, and V. Matveev, "On multi-rogue wave solutions of the NLS equation and positon solutions of the KdV equation," *The European Physical Journal Special Topics*, vol. 185, no. 1, pp. 247–258, aug 2010.

[30] B. B. Kadomtsev and V. I. Petviashvili, "On the Stability of Solitary Waves in Weakly Dispering Media," pp. 539–541, 1970.

[31] V. E. Zakharov, "Stability of Periodic Waves of Finite Amplitude on the Surface of a Deep Fluid," *Journal of Applied Mechanics and Technical Physics*, vol. 9, no. 2, pp. 190–194, 1968.

[32] D. Clamond and J. Grue, "A fast method for fully nonlinear water-wave computations," *Journal of Fluid Mechanics*, vol. 447, pp. 337–355, oct 2001.

[33] D. Fructus, D. Clamond, J. Grue, and O. Kristiansen, "An efficient model for three-dimensional surface wave simulations. Part I: Free space problems," *Journal of Computational Physics*, vol. 205, pp. 665–685, 2005.

[34] A. Toffoli, E. M. Bitner-Gregersen, a. R. Osborne, M. Serio, J. Monbaliu, and M. Onorato, "Extreme Waves in Random Crossing Seas: Laboratory Experiments and Numerical Simulations," *Geophysical Research Letters*, vol. 38, pp. 1–5, 2011.

[35] F. Fedele, J. Brennan, S. Ponce De León, J. Dudley, and F. Dias, "Real world ocean rogue waves explained without the modulational instability," *Scientific Reports*, vol. 6, no. May, pp. 1–11, 2016.

[36] P. Lubin, S. Vincent, J. P. Caltagirone, and S. Abadie, "Fully three-dimensional direct numerical simulation of a plunging breaker," *Comptes Rendus - Mecanique*, vol. 331, no. 7, pp. 495–501, 2003.

[37] M. A. Tayfun and F. Fedele, "Wave-height distributions and nonlinear effects," in *Proceedings of 25th International Conference on Offshore Mechanics and Arctic Engineering*, Hamburg, Germany, 2006.

[38] M.-R. Alam, Y. Liu, and D. K. P. Yue, "Bragg resonance of waves in a two-layer fluid propagating over bottom ripples. Part II. Numerical simulation," *Journal of Fluid Mechanics*, vol. 624, pp. 191–224, mar 2009.

[39] A. V. Porubov, "On formation of the rogue waves and holes in Ocean," in *Rendiconti del Seminario Matematico*, vol. 65, no. 2, 2007, pp. 279–286.

[40] M.-R. Alam, Y. Liu, and D. K. P. Yue, "Bragg Resonance of Waves in a Two-layer Fluid Propagating Over Bottom Ripples. Part I. Perturbation Analysis," *Journal of Fluid Mechanics*, vol. 624, p. 191, mar 2009.

[41] M.-R. Alam, "A new triad resonance between co-propagating surface and interfacial waves," *Journal of Fluid Mechanics*, vol. 691, pp. 267–278, dec 2011.

[42] W. Cousins and T. P. Sapsis, "Reduced order prediction of rare events in unidirectional nonlinear water waves," *Journal of Fluid Mechanics*, vol. 790, pp. 368–388, 2016.

[43] M. Erkintalo, "Rogue waves: Predicting the unpredictable?" *Nature Photonics*, vol. 9, no. 9, pp. 560–562, 2015.

[44] N. Akhmediev, A. Ankiewicz, J. M. Soto-Crespo, and J. M. Dudley, "Rogue wave early warning through spectral measurements?" *Physics Letters, Section A: General, Atomic and Solid State Physics*, vol. 375, no. 3, pp. 541–544, 2011.

[45] F. Ball, "Energy transfer between external and internal gravity waves," pp. 465–478, 1964.

[46] D. G. Dommermuth and D. K. P. Yue, "A high-order spectral method for the study of nonlinear gravity waves," *Journal of Fluid Mechanics*, vol. 184, p. 267, apr 1987.

[47] Y. Liu and D. K. Yue, "On generalized Bragg scattering of surface waves by bottom ripples," *Journal of Fluid Mechanics*, vol. 356, pp. 297–326, 1998.

[48] W. J. Pierson and L. Moskowitz, "A Proposed Spectral Form for Fully Developed Wind Seas Based on the Similarity Theory of S. A. Kitaigorodski," New York University, Tech. Rep., 1963.

[49] K. Hasselmann, T. Barnett, E. Bouws, and H. Carlson, "Measurements of wind-wave growth and swell decay during the Joint North Sea Wave Project," *Deutsches Hydrographisches Institut - Hamburg*, 1973.

[50] V. Ruban, Y. Kodama, M. Ruderman, J. Dudley, R. Grimshaw, P. McClintock, M. Onorato, C. Kharif, E. Pelinovsky, T. Soomere, G. Lindgren, N. Akhmediev, A. Slunyaev, D. Solli, C. Ropers, B. Jalali, F. Dias, and A. Osborne, "Rogue waves towards a unifying concept?: Discussions and debates," *The European Physical Journal Special Topics*, vol. 185, no. 1, pp. 5–15, aug 2010.

[51] P. a. E. M. Janssen, "Nonlinear Four-Wave Interactions and Freak Waves," *Journal of Physical Oceanography*, vol. 33, pp. 863–884, 2003.

[52] M.-R. Alam, "Predictability horizon of oceanic rogue waves," *Geophysical Research Letters*, vol. 41, pp. 1–9, 2014.

[53] C. Guedes Soares and R. Pascoal, "On the Profile of Large Ocean Waves," *Journal of Offshore Mechanics and Arctic Engineering*, vol. 127, no. 4, p. 306, 2005.

[54] C. Soares, N. Fonseca, and R. Pascoal, "Abnormal wave-induced load effects in ship structures," *Journal of Ship Research*, vol. 52, no. 1, pp. 30–44, 2008.

[55] D. Peregrine, "Water waves, nonlinear Schrödinger equations and their solutions," *The Journal of the Australian Mathematical Society. Series B. Applied Mathematics*, vol. 25, no. 1, pp. 16–43, 1983.

[56] A. Chabchoub and N. Akhmediev, "Observation of rogue wave triplets in water waves," *Physics Letters A*, vol. 377, no. 38, pp. 2590–2593, 2013.

[57] J. S. He, H. R. Zhang, L. H. Wang, K. Porsezian, and a. S. Fokas, "A generating mechanism for higher order rogue waves," *Physical Review E*, vol. 87, no. 5, p. 12, 2013.

[58] D. J. Kedziora, A. Ankiewicz, and N. Akhmediev, "Circular rogue wave clusters," *Physical Review E - Statistical, Nonlinear, and Soft Matter Physics*, vol. 84, no. 5, pp. 1–7, 2011.

[59] O. Phillips, D. Gu, and M. Donelan, "Expected Sturcture of Extreme Waves in a Gaussian Sea. Part I: Theory and SWADE Buoy Measurements," *Journal of Physical Oceanography*, vol. 23, pp. 992–1000, 1992.

[60] S. Haver, "A Possible Freak Wave Event Measured at the Draupner Jacket January 1 1995," *Rogue Waves 2004*, 2004.

[61] S. Sand, H. Ottesen, P. Klinting, O. Gudmestadt, and M. Sterndorff, "Freak Wave Kinematics," *NATO ASI Series ed. Kluwer Academic Publisher*, pp. 535–549, 1990.

[62] C. Guedes Soares, Z. Cherneva, and E. M. Antao, "Characteristics of abnormal waves in North Sea storm sea states," *Applied Ocean Research*, vol. 25, no. 2003, pp. 337–344, 2003.

[63] N. Mori, P. C. Liu, and T. Yasuda, "Analysis of freak wave measurements in the Sea of Japan," *Ocean Engineering*, vol. 29, no. 11, pp. 1399–1414, 2002.

[64] C. Garett and J. Gemmrich, "Rogue waves," *Physics Today*, vol. 62, no. 6, pp. 62–63, 2009.

[65] M. Klein and G. Clauss, "The New Year Wave in a seakeeping basin: Generation, propagation, kinematics and dynamics," *Ocean Engineering*, vol. 38, no. 14-15, pp. 1624–1639, 2011.

[66] J. Gemmrich and J. Thomson, "Observations of the shape and group dynamics of rogue waves," *Geophysical Research Letters*, pp. 1–8, 2017.

[67] G. F. Clauss and M. Klein, "The New Year Wave: Spatial Evolution of an Extreme Sea State," *Journal of Offshore Mechanics and Arctic Engineering*, vol. 131, no. 4, p. 041001, 2009.

[68] P. Müller, C. Garrett, and A. Osborne, "MEETING REPORT — Rogue WavesThe Fourteenth 'Aha Huliko'a Hawaiian Winter Workshop," *Oceanography*, vol. 18, no. 3, pp. 66–75, 2005.

[69] H. Tomita and T. Kawamura, "Statistaical Analysis and Inference from the In-Situ Data of the Sea of Japan with Reference to Abnormal and/or Freak Waves," *Proceedings of the Tenth International Offshore and Polar Engineering Conference*, vol. 111, pp. 116–122, 2000.

[70] A. Sergeeva and A. Slunyaev, "Rogue waves, rogue events and extreme wave kinematics in spatio-temporal fields of simulated sea states," *Natural Hazards and Earth System Sciences*, vol. 13, no. 7, pp. 1759–1771, 2013.

[71] B. T. B. Benjamin and J. Feir, "The Distribution of Wave Trains on Deep Water," *Journal of Fluid Mechanics*, vol. 27, pp. 417–430, 1967.

[72] N. Mori and T. Yasuda, "A weakly non-gaussian model of wave height distribution for random wave train," *Ocean Engineering*, vol. 29, no. 10, pp. 1219–1231, 2002.

[73] F. Dias and C. Kharif, "Nonlinear Gravity and Capillary-Gravity Waves," *Annual Review of Fluid Mechanics*, vol. 31, no. 1, pp. 301–346, 1999.

[74] A. L. Latifah and E. van Groesen, "Coherence and predictability of extreme events in irregular waves," *Nonlinear Processes in Geophysics*, vol. 19, no. 2, pp. 199–213, 2012.

[75] D. Chalikov, "Freak waves: Their occurrence and probability," *Physics of Fluids*, vol. 21, no. 7, p. 076602, 2009.

[76] K. Hasselmann, W. Sell, D. B. Ross, and P. Müller, "A Parametric Wave Prediction Model," pp. 200–228, 1976.

[77] N. Nekouee, S. A. Hamidi, and R. Etemadi, "Sensitivity analysis of numerical wave predictions models, considering wind and geometry effects in rectangular lakes," *Ocean Engineering*, vol. 104, pp. 549–557, 2015.

[78] D. G. Dommermuth, T. C. Fu, K. a. Brucker, T. T. O'Shea, and D. C. Wyatt, "Numerical Prediction of a Seaway," in *28th Symposium on Naval Hydrodynamics Pasadena*, no. September, Pasadena, CA, USA, 2010.

[79] D. M. Sigman, S. L. Jaccard, and G. H. Haug, "Polar ocean stratification in a cold climate," *Nature*, vol. 428, pp. 59–63, 2004.

[80] C. Staquet and J. Sommeria, "I NTERNAL G RAVITY W AVES : From Instabilities to Turbulence," *Annual Review of Fluid Mechanics*, vol. 34, no. 1, pp. 559–593, 2002.

[81] V. N. Kudryavtsev, "Interaction between the surface and internal waves: The modulation and maser mechanisms," *Physical Oceanography*, vol. 4, no. 5, pp. 357–375, 1993.

[82] J. P. Rebert, J. R. Donguy, G. Eldin, and K. Wyrtki, "Relations between sea level, thermocline depth, heat content, and dynamic height in the tropical Pacific Ocean," *Journal of Geophysical Research*, vol. 90, no. C6, p. 11719, 1985.

[83] N. Suginohara, "Onset of coastal upwelling in a two-layer ocean by wind stress with longshore variation," *Journal of the Oceanographical Society of Japan*, vol. 30, no. 1, pp. 23–33, 1974.

[84] P. Lynett and P. L.-F. Liu, "A two-layer approach to wave modelling," *Proceedings of the Royal Society A: Mathematical, Physical and Engineering Sciences*, vol. 460, no. 2049, pp. 2637–2669, 2004.

[85] C.-Y. Chen, J. R.-C. Hsu, M.-H. Cheng, H.-H. Chen, and C.-F. Kuo, "An investigation on internal solitary waves in a two-layer fluid: Propagation and reflection from steep slopes," *Ocean Engineering*, vol. 34, no. 1, pp. 171–184, 2007.

[86] I. R. Young, "Parametric hurricane wave prediction model," *Proc ASCE J Waterway Port Coast Ocean Eng*, vol. 114, no. 5, pp. 637–652, 1989.

[87] Z. Zhao, V. Klemas, Q. Zheng, X. Li, and X.-H. Yan, "Estimating parameters of a two-layer stratified ocean from polarity conversion of internal solitary waves observed in satellite SAR images," *Remote Sensing of Environment*, vol. 92, no. 2, pp. 276–287, 2004.

[88] X. Li, P. Clemente-Colón, and K. S. Friedman, "Estimating oceanic mixed-layer depth from internal wave evolution observed from Radarsat-1 SAR," *Johns Hopkins APL Technical Digest (Applied Physics Laboratory)*, vol. 21, no. 1, pp. 130–135, 2000.

[89] J. Sun and H. Kawamura, "Retrieval of surface wave parameters from sar images and their validation in the coastal seas around Japan," *Journal of Oceanography*, vol. 65, no. 4, pp. 567–577, 2009.

[90] E. M. Bitner-Gregersen and A. K. Magnusson, "Extreme events in field data and in a second order wave model," *Rogue Waves*, no. September 2015, pp. 1–16, 2004.

[91] A. Islas and C. Schober, "Predicting rogue waves in random oceanic sea states," *Physics of Fluids*, no. October 2004, pp. 18–21, 2005.

[92] A. B. Kara, P. A. Rochford, and H. E. Hurlburt, "An optimal definition for ocean mixed layer depth," *Journal of Geophysical Research*, vol. 105, no. C7, p. 16803, 2000.

[93] M. Leijon, C. Boström, O. Danielsson, S. Gustafsson, K. Haikonen, O. Langhamer, E. Strömstedt, M. Stålberg, J. Sundberg, O. Svensson, S. Tyrberg, and R. Waters, "Wave Energy from the North Sea: Experiences from the Lysekil Research Site," *Surveys in Geophysics*, vol. 29, no. 3, pp. 221–240, 2008.

[94] A. Leonard-Williams and A. Saulter, "Comparing EVA results from analysis of 12 years of WAVEWATCHIII and 50 years of NORA10 data," Met Office, Tech. Rep. February, 2013.

[95] Standards Norway, "NORSOK: N-003 Actions and action effects," *The Norwegian Oil Industry Association (OLF) and Federation of Norwegian Manufacturing Industries (TBL)*, no. September, 2007.

[96] J. L. Hammack and D. M. Henderson, "Resonant interactions among gravity waves," *Annu. Rev. Fluid Mech.*, vol. 25, no. 1963, pp. 55–97, 1993.

[97] E. Bernard, F. González, and C. Meinig, *Developing Tsunami-Resilient Communities*, E. Bernard, Ed. Springer, 2005.

[98] M. G. Bulatov, Y. a. Kravtsov, O. Y. Lavrova, K. T. Litovchenko, M. I. Mityagina, M. D. Raev, K. D. Sabinin, Y. G. Trokhimovskii, A. N. Churyumov, and I. V. Shugan, "Physical mechanisms of aerospace radar imaging of the ocean," *Physics-Uspekhi*, vol. 46, no. 1, pp. 63–79, 2003.

[99] F. Collard, F. Ardhuin, and B. Chapron, "Extraction of coastal ocean wave fields from SAR images," *IEEE Journal of Oceanic Engineering*, vol. 30, no. 3, pp. 526–533, 2005.

[100] Q. Guo and M.-R. Alam, "Sensitivity of Rogue Wave Prediction on Oceanic Stratification," in *Proceedings of the ASME 2015 34th International Conference on Ocean, Offshore and Arctic Engineering*, St. John's, 2015.

[101] N. Akhmediev, J. M. Soto-Crespo, A. Ankiewicz, and N. Devine, "Early detection of rogue waves in a chaotic wave field," *Physics Letters, Section A: General, Atomic and Solid State Physics*, vol. 375, no. 33, pp. 2999–3001, 2011.

[102] M. Onorato, S. Residori, U. Bortolozzo, A. Montina, and F. Arecchi, "Rogue waves and their generating mechanisms in different physical contexts," *Physics Reports*, vol. 528, no. 2, pp. 47–89, jul 2013.

[103] I. V. Lavrenov, "The wave energy concentration at the Agulhas Current off South Africa," *Natural Hazards*, vol. 17, pp. 117–127, 1998.

[104] C. Fochesato, S. Grilli, and F. Dias, "Numerical modeling of extreme rogue waves generated by directional energy focusing," *Wave Motion*, vol. 44, no. 5, pp. 395–416, apr 2007.

[105] M. Onorato, A. R. Osborne, and M. Serio, "Modulational instability in crossing sea states: A possible mechanism for the formation of freak waves," *Physical Review Letters*, vol. 96, no. 1, pp. 1–4, 2006.

[106] I. Didenkulova and E. Pelinovsky, "Rogue waves in nonlinear hyperbolic systems (shallow-water framework)," *Nonlinearity*, vol. 24, no. 3, pp. R1–R18, 2011.

[107] M.-R. Alam, Y. Liu, and D. K. P. Yue, "Oblique Sub- and Super-harmonic Bragg Resonance of Surface Waves by Bottom Ripples," *Journal of Fluid Mechanics*, vol. 643, pp. 437–447, 2010.

[108] Q. Guo and M.-R. Alam, "Statistical investigation of the surface profile of rogue waves in 2d non-breaking seas," in *Proceedings of the ASME 2016 35th International Conference on Ocean, Offshore and Arctic Engineering*, Busan, 2016.

[109] W. Fujimoto and T. Waseda, "OMAE2016-54768," in *Proceedings of the ASME 2016 35th International Conference on Ocean, Offshore and Arctic Engineering OMAE2016*, 2016, pp. 1–7.

[110] N. P. Holliday, M. J. Yelland, R. Pascal, V. R. Swail, P. K. Taylor, C. R. Griffiths, and E. Kent, "Were extreme waves in the Rockall Trough the largest ever recorded?" *Geophysical Research Letters*, vol. 33, no. 5, p. L05613, 2006.

[111] J. B. Jakobsen, S. Haver, and J. E. Odegard, "Study of freak waves by use of wavelet transform," *Proceedings of the Eleventh (2001) International Offshore and Polar Engineering Conference, Vol Iii*, vol. III, pp. 58–64, 2001.

[112] C. Bayndr, "Early detection of rogue waves by the wavelet transforms," *Physics Letters A*, vol. 380, no. 1-2, pp. 156–161, 2016.

[113] A. Moitra, C. Chabalko, and B. Balachandran, "Extreme wave solutions: Parametric studies and wavelet analysis," *International Journal of Non-Linear Mechanics*, vol. 83, pp. 39–47, 2016.

[114] S. Kitaigorodski, "Applications of the theory of similarity to the analysis of wind-generated wave motion as a stochastic process," *Izv. Akad. Nauk, SSSR. Ser. Geofiz.*, vol. 1, pp. 105–117, 1962.

Appendix A

Derivation of similarity in rogue wave profiles

A.1 Similarity of rogue wave profiles in several sea states

Here we showed that the linear wave governing equations has self-similar solutions given the normalized wind-wave spectra(i.e. JONSWAP spectrum) are identical. An important basis of this similarity solution is the self-similarity features of the JONSWAP parameterization. Actually, this self-similarity of the wind-wave spectra has been found in experiments[114] before the theoretical explain[49]. We proved that the linear wave solutions are self-similar given the initial self similar JONSWAP spectra through dimensional analysis. The detailed derivation is shown here.

Recall the fully nonlinear governing equations of free surface wave, as Equation (2.1). Assuming that both surface elevation η and velocity potential ϕ are in the order of a small parameter ϵ. Then we express ϕ and η in series of ϵ, as

$$\eta = \epsilon\eta^{(1)} + \epsilon^2\eta^{(2)} + \mathcal{O}(\epsilon^3) \tag{A.1a}$$

$$\phi = \epsilon\phi^1 + \epsilon^2\phi^{(2)} + \mathcal{O}(\epsilon^3) \tag{A.1b}$$

By substituting Equation (A.1) into (2.1) and collecting only the leading order(i.e.$\mathcal{O}(\epsilon)$) terms, the governing equations of linear surface wave are obtained as follows:

$$\begin{aligned} \nabla^2\phi^{(1)} &= 0, & \text{for } -h < z < 0 \\ \eta_t^{(1)} &= \phi_z^{(1)}, & \text{at } z = 0 \\ \phi_t^{(1)} &= -g\eta^{(1)}, & \text{at } z = 0 \end{aligned} \tag{A.2}$$

For convenience, we drop the leading order notation (1) for all variables. We further non-dimensionalize the variables by the following relations:

$$
\begin{aligned}
\tilde{\eta} &= \eta/H_s \\
\tilde{t} &= t/T_p \\
\tilde{z} &= z/(gT_p^2) \\
\tilde{\phi} &= \phi/(gT_pH_s) \\
\tilde{x} &= x/\lambda_p \\
\tilde{k} &= k\lambda_p \\
\tilde{\omega} &= \omega/\omega_p \\
\tilde{h} &= h/\lambda_p
\end{aligned} \tag{A.3}
$$

where the parameters with ˜ are non-dimensional, and H_s, T_p, ω_p, λ_p are parameters representing different sea states. H_s is the significant wave height, T_p is the peak period, $\omega_p = 2\pi/T_p$ is the peak period. λ_p is the wavelength for the wave with peak frequency. g is the gravitational acceleration. Then we substitute (A.3) into (A.2) and non-dimensional governing equations for linear wave write:

$$
\nabla^2\tilde{\phi} = 0, \qquad\qquad\qquad \text{for } -h < \tilde{z} < 0 \tag{A.4a}
$$

$$
\tilde{\eta}_{\tilde{t}} = \tilde{\phi}_{\tilde{z}}, \qquad\qquad\qquad \text{at } \tilde{z} = 0 \tag{A.4b}
$$

$$
\tilde{\phi}_{\tilde{t}} = -\tilde{\eta}, \qquad\qquad\qquad \text{at } \tilde{z} = 0 \tag{A.4c}
$$

Equation (A.4a) is automatically satisfied if ϕ is assumed to be a sinusoid function in space and time. Then the solutions of non-dimensional wave elevation $\tilde{\eta}$ and velocity potential $\tilde{\phi}$ on the free surface are calculated by direct integrating (A.4b) and (A.4c) respect to time t. The solutions write

$$
\begin{aligned}
\tilde{\eta} &= \tilde{\eta}_0 + \int \tilde{\phi}_{\tilde{z}} d\tilde{t}, \quad \text{at } \tilde{z} = 0 \\
\tilde{\phi} &= \tilde{\phi}_0 - \int \tilde{\eta} d\tilde{t}, \quad \text{at } \tilde{z} = 0
\end{aligned} \tag{A.5}
$$

where $\tilde{\eta}_0$ and $\tilde{\phi}_0$ are initial conditions of right propagating waves to (A.5). These initial conditions write

$$
\begin{aligned}
\tilde{\eta}_0 &= \sum_n \frac{A_n}{H_s} \cos(\tilde{k}\tilde{x} + \theta_n) \qquad \text{at } \tilde{z} = 0 \\
\tilde{\phi}_0 &= \frac{1}{2\pi} \sum_n \frac{A_n}{H_s} \frac{1}{\tilde{\omega}} \sin(\tilde{k}\tilde{x} + \theta_n) \quad \text{at } \tilde{z} = 0
\end{aligned} \tag{A.6}
$$

From the continuity equation the z-dependence of the initial velocity potential $\tilde{\phi}_0$ is obtained as

$$
\tilde{\phi}_0 = \frac{1}{2\pi} \sum_n \frac{A_n}{H_s} \frac{1}{\tilde{\omega}} \frac{\cosh(\tilde{k}(C_1\tilde{z} + \tilde{h}))}{\cosh(\tilde{k}\tilde{h})} \sin(\tilde{k}\tilde{x} + \theta_n) \tag{A.7}
$$

where $C_1 = gT_p^2/\lambda_p$ is constant. Then $\tilde{\phi}_{\tilde{z}}$ writes

$$
\tilde{\phi}_{0\tilde{z}} = \frac{1}{2\pi} \sum_n \frac{A_n}{H_s} \frac{C_1\tilde{k}}{\tilde{\omega}} \frac{\sinh(\tilde{k}(C_1\tilde{z} + \tilde{h}))}{\cosh(\tilde{k}\tilde{h})} \sin(\tilde{k}\tilde{x} + \theta_n) \tag{A.8}
$$

where A_n the θ_n are the amplitude and random phase shift of the n-th wave mode. By substituting equation (A.6) into (A.5), then (A.8) can be written as

$$
\begin{aligned}
\tilde{\eta} = \tilde{\eta}_0 \quad\quad &+ \int \tilde{\phi}_{\tilde{z}} d\tilde{t} \\
= \sum_n \frac{A_n}{H_s} \cos(\tilde{k}\tilde{x} + \theta_n) \quad &+ \int \frac{1}{2\pi} \sum_n \frac{A_n}{H_s} \frac{C_1 \tilde{k}}{\tilde{\omega}} \frac{\sinh(\tilde{k}\tilde{h})}{\cosh(\tilde{k}\tilde{h})} sin(\tilde{k}\tilde{x} - 2\pi\tilde{\omega}\tilde{t} + \theta_n) d\tilde{t} \\
= \sum_n \frac{A_n}{H_s} \cos(\tilde{k}\tilde{x} + \theta_n) \quad &+ \frac{1}{2\pi} \sum_n \frac{A_n}{H_s} \frac{C_1 \tilde{k}}{\tilde{\omega}} \frac{\sinh(\tilde{k}\tilde{h})}{\cosh(\tilde{k}\tilde{h})} (-\frac{1}{2\pi\tilde{\omega}}) cos(\tilde{k}\tilde{x} - 2\pi\tilde{\omega}\tilde{t} + \theta_n) \\
= \sum_n \frac{A_n}{H_s} \cos(\tilde{k}\tilde{x} + \theta_n) \quad &- \frac{1}{4\pi^2} \sum_n \frac{A_n}{H_s} \frac{C_1 \tilde{k}}{\tilde{\omega}^2} \tanh(\tilde{k}\tilde{h}) \cos(\tilde{k}\tilde{x} - 2\pi\tilde{\omega}\tilde{t} + \theta_n)
\end{aligned} \quad\quad \text{(A.9)}
$$

$$
\begin{aligned}
\tilde{\phi} = \tilde{\phi}_0 \quad\quad\quad &- \int \tilde{\eta} d\tilde{t} \\
= \frac{1}{2\pi} \sum_n \frac{A_n}{H_s} \frac{1}{\tilde{\omega}} \sin(\tilde{k}\tilde{x} + \theta_n) \quad &- \int \sum_n \frac{A_n}{H_s} \cos(\tilde{k}\tilde{x} - 2\pi\tilde{\omega}\tilde{t} + \theta_n) d\tilde{t} \\
= \frac{1}{2\pi} \sum_n \frac{A_n}{H_s} \frac{1}{\tilde{\omega}} \sin(\tilde{k}\tilde{x} + \theta_n) \quad &- \sum_n \frac{A_n}{H_s} (-\frac{1}{2\tilde{\pi}\omega}) \sin(\tilde{k}\tilde{x} - 2\pi\tilde{\omega}\tilde{t} + \theta_n) \\
= \frac{1}{2\pi} \sum_n \frac{A_n}{H_s} \frac{1}{\tilde{\omega}} \sin(\tilde{k}\tilde{x} + \theta_n) \quad &+ \frac{1}{2\pi} \sum_n \frac{A_n}{H_s} \frac{1}{\tilde{\omega}} \sin(\tilde{k}\tilde{x} - 2\pi\tilde{\omega}\tilde{t} + \theta_n)
\end{aligned} \quad\quad \text{(A.10)}
$$

From (A.9) and (A.10) we find that $\tilde{\eta}$ and $\tilde{\phi}$ can have the same normalized wave amplitudes across different sea states provided that $\frac{A_n}{H_s}$ and $\frac{A_n}{H_s} \frac{C_1 \tilde{k}}{\tilde{\omega}^2} \tanh(\tilde{k}\tilde{h})$ are identical for the sea states considered. From a given spectrum $S(\omega)$, the wave amplitude A_n is calculated as

$$
A_n = \sqrt{2S(\omega)\delta\omega} \quad\quad \text{(A.11)}
$$

We substitute (A.3) into (A.11), then we get the expression for normalized wave amplitude for the n-th wave mode:

$$
\begin{aligned}
A_n/H_s &= \sqrt{2S(\omega)/H_s^2 \delta\tilde{\omega}\omega_p} \\
&= \sqrt{2S(\omega)/(H_s^2/\omega_p)\delta\tilde{\omega}} \\
&= \sqrt{2\tilde{S}\delta\tilde{\omega}}
\end{aligned} \quad\quad \text{(A.12)}
$$

From (A.1), we found that the non-dimensional wave amplitude depends on the integral of wave spectrum . Here, we considered JONSWAP spectrum in most of the simulations. In this dissertation, we considered three sea states(i.e. 4, 5 and 6) as stated in Table 2.2. Further more, we plot the normalized spectral density function $\tilde{S} = S/(H_s^2/\omega_p)$ respect to

the normalized angular frequency $\tilde{\omega} = \omega/\omega_p$ for sea states 4, 5 and 6. An identical normalized spectrum shape has been observed across the sea states considered.
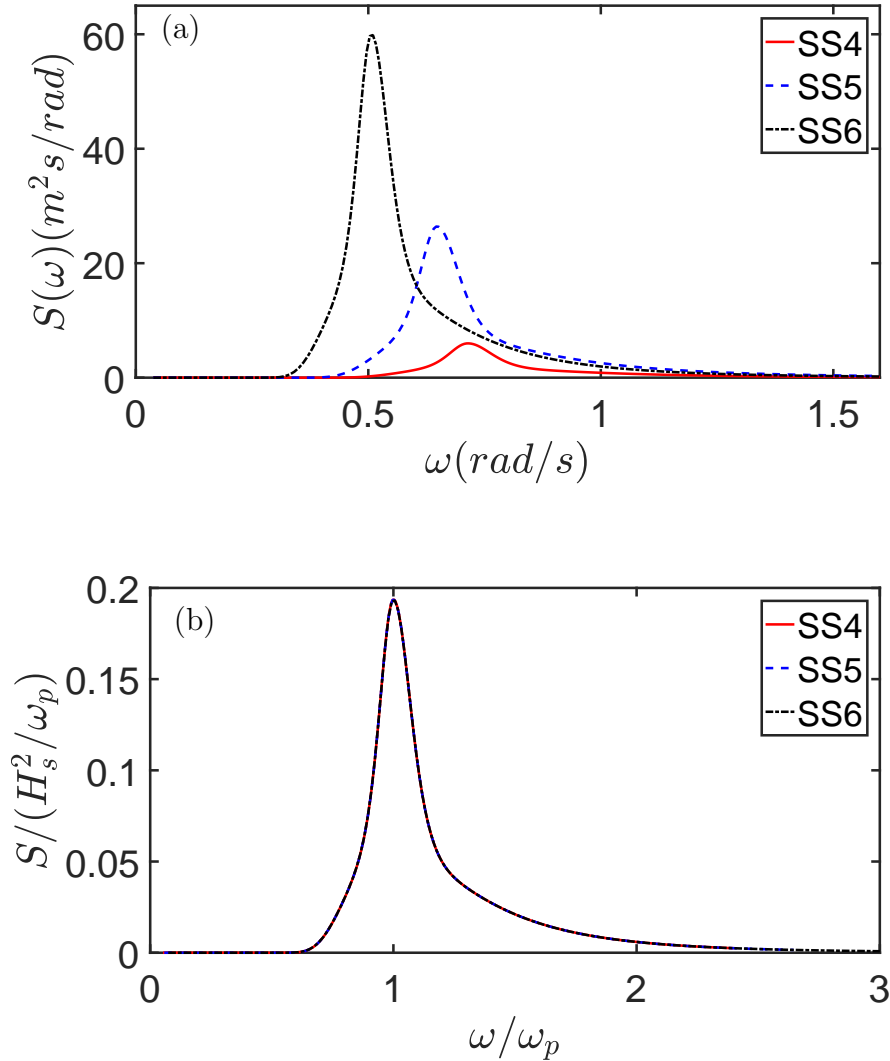

Figure A.1: Dimensional and non-dimensional JONSWAP spectrum in sea state 4, 5 and 6, as in (a) and (b) respectively. The non-dimensional JONSWAP spectra across these three sea states have identical shape across the sea states considered. This is equivalent of showing that the right hand side of equation (A.1) are identical for these three sea states. Hence the normalized wave amplitude should be the same.

Given linear wave governing equations (A.4), the non-dimensional dispersion relation can

be derived as

$$\tilde{\omega} = \sqrt{\frac{\tilde{k}g}{\lambda_p \omega_p^2} \tanh(\tilde{k}\tilde{h})} \qquad (A.13)$$

We substitute C_1 and (A.1) into the other term $\frac{C_1 \tilde{k}}{\tilde{\omega}^2} \tanh(\tilde{k}\tilde{h})$. We obtained the normalized term to be:

$$
\begin{aligned}
\frac{C_1 \tilde{k}}{\tilde{\omega}^2} \tanh(\tilde{k}\tilde{h}) &= \frac{gT_p^2 \tilde{k}}{\lambda_p \tilde{\omega}^2} tanh(\tilde{k}\tilde{h}) \\
&= \frac{gT_p^2 \tilde{k}}{\lambda_p \frac{\tilde{k}g}{\lambda_p \omega_p^2} \tanh(\tilde{k}\tilde{h})} \tanh(\tilde{k}\tilde{h}) \\
&= T_p^2 \omega_p^2 \\
&= 4\pi^2
\end{aligned}
\qquad (A.14)
$$

Up to now, we have shown that the linear wave solutions η and ϕ are identical across all three sea states considered in this dissertation. The nonlinear mechanism becomes much more complicated due to the wave-wave resonant interactions.

Appendix B

Derivation of energy flux across a vertical plane

The total energy in the fluid domain can be expressed as:

$$E(t) = \rho \iiint_\Omega (1/2|\mathbf{v}|^2 + gz)dV \tag{B.1}$$

Then the energy flux is as:

$$p(t) = \frac{dE}{dt} = \frac{d}{dt}\rho \iiint_\Omega (1/2|\mathbf{v}|^2 + gz)dV$$
$$= \iiint_\Omega \frac{\partial \mathcal{E}}{\partial t}dV + \iint_S \mathcal{E}U_n dS \tag{B.2a}$$

Where $\mathcal{E} = \rho(1/2|\mathbf{v}|^2 + gz)$. Then we calculate the equation term by term.

$$\frac{\partial \mathcal{E}}{\partial t} = \frac{\partial}{\partial t}(1/2\rho|\mathbf{v}|^2 + \rho gz)$$
$$= \frac{\partial}{\partial t}(1/2\rho|\nabla\phi|^2 + \rho gz)$$
$$= \frac{\partial}{\partial t}(1/2\rho(\nabla\phi \cdot \nabla\phi))$$
$$= \frac{1}{2}\rho\nabla \cdot (\frac{\partial\phi}{\partial t}\nabla\phi) - \frac{1}{2}\rho\frac{\partial\phi}{\partial t}\nabla^2\phi$$
$$= \frac{1}{2}\rho\nabla \cdot (\frac{\partial\phi}{\partial t}\nabla\phi)$$

Thus if we consider the case for gravity surface waves, the energy flux across a fixed vertical plane can be calculated as:

$$p(t) = \rho \iiint_\Omega \nabla \cdot (\frac{\partial\phi}{\partial t}\nabla\phi)dV + \rho \iint_S (1/2|\mathbf{v}|^2 + gz)U_n dS$$

$$= \rho \iiint_{\Omega} \nabla \cdot (\frac{\partial \phi}{\partial t} \nabla \phi) dV$$

$$= \rho \iint_{S} \frac{\partial \phi}{\partial t} \nabla \phi \cdot \mathbf{n} dS$$

$$= \rho \iint_{S} \frac{\partial \phi}{\partial t} \phi_n dS$$

For 2-dimensional problem with water depth h, the energy flux is as:

$$p(t) = -\rho \int_{-h}^{\eta} \frac{\partial \phi}{\partial t} \phi_x dz \tag{B.5}$$

Appendix C

Wavelet analysis in space

The wave elevation is a function of time and space $\eta(x,t)$. We would like to select the scale and energy intensity of wave elevations, hence we do wavelet analysis on wave elevations at each time step.

C.1   Continuous wavelet transformation

The wavelet transformation $W_i(s)$ at location $t_i = i\delta x$ on a scale s of a discrete spatial series $f_j = f(x_j)$ of length N with a sampling interval Δx can be interpreted as an extension of discrete Fourier transformation $F(k) = \sum_j f_j exp(ikx_j)$. Wavelet transformation replaces the periodic exponential $exp(ikx_j)$ with a localized wavelet $\Psi(x_j - x_i, s)$, which is located around the location x_i and stretched according to the investigated scale s. Thus the spatial series can be decomposed scale- and space-dependent:

$$W_i(s) = \sum_{j=0}^{N-1} f_j \Psi((j-i)\delta x, s) \tag{C.1}$$

If one considers arbitrary scales between the sampling interval and the length of the time series, one speaks of continuous wavelet transformation(CWT). The wavelet $\Psi(x_j - x_i, s)$ is a stretched and translated version of a chosen mother wavelet, normalized with a factor $c(s)$.

$$\Psi(x_j - x_i, s) = c(s)\Psi_0(\frac{t_j - t_i}{s}) \tag{C.2}$$

In the following, we always consider the Morlet mother wavelet

$$\Psi_0(\theta) = \pi^{-1/4} \exp^{i\omega_0\theta} \exp^{-\theta^2/2} \tag{C.3}$$

Where $\theta = \frac{x_j - x_i}{s}$ and ω_0 are unit-less. The Gaussian envelope $\exp(-\theta^2/2)$ localizes the wavelet in space. The space/scale resolution is adjusted by ω_0. For higher values of ω_0, the scale resolution increases, whereas space resolution decreases and vice versa. Wave number k and wavelet scale s are not directly related.
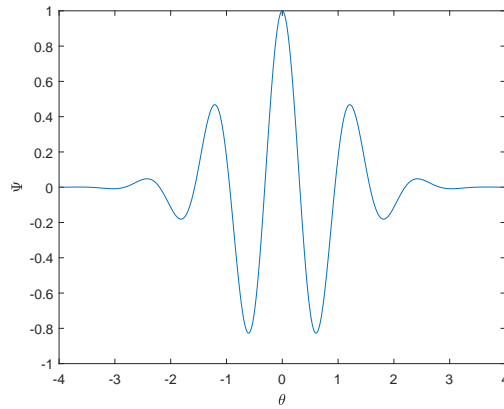
Figure C.1: Morlet wavelet

C.2 Wave power spectrum

A wavelet power spectrum(WPS) can be defined as the wavelet transformation of the auto-correlation function, which is defined as

$$WPS_i(s) = |W_i(s)|^2 \tag{C.4}$$

$WPS_i(s)$ describes the power of the signal $f(x)$ at a certain location x_i on a scale s, where s is actual wavelet scale$/\lambda_p$. So scale value 1 means the scale of the wavelet is 1 times λ_p.